Growth and characterization of bulk $GaAs_{1-x}Bi_x$/GaAs diodes

CHRISTOPHER JACK OWEN HUNTER

A thesis submitted for the degree of Doctor of Philosophy

Department of Electronic and Electrical Engineering

The University of Sheffield

March 2014

Table of Contents

Acknowledgements

First I would like to thank Prof. John David for his support and guidance throughout the project (and indeed for proposing the project to begin with) and Dr. Faebian Bastiman for building and maintaining the MBE-STM system so that it was able to successfully produce my samples. Thanks are also due to Dr. Rahman Mohmad, Danuta and Rob for all their help and for giving feedback on my work. I would like to acknowledge Dr. Dave Sykes at Loughborough Surface Analysis and Dr. Richard Beanland at the University of Warwick for carrying out the SIMS and TEM measurements respectively. Thanks also go to Ian Burns for proofreading some of this thesis.

I would like to thank members of the Impact Ionization Group past and present who have helped me with measurements, particularly Siew Li for her help with the photocurrent measurements and Pin Jern for showing me how to use the Janis probe setup. The staff of the National Centre for III-V Technologies have also been very helpful. Richard Frith has devoted much of his time to maintaining the MBE-STM setup, and Dr. Rob Airey and Dr. Kris Groom also deserve thanks for their help with the device processing.

I would also like to acknowledge all the support I have received from E-Futures - Neil Lowrie deserves a special mention for organising what has been a very enjoyable and productive course. Thanks go to all the inhabitants of the E-House who have provided welcome distractions from PhD work over the past few years.

Last, but definitely not least, I thank my family for providing love, support and food, where appropriate.

Abstract

To explore the feasibility of utilising gallium arsenide bismide (GaAsBi) as a material for use in solar cells, undoped GaAsBi layers ranging from 50 nm to 350 nm in thickness have been grown by molecular beam epitaxy (MBE) in a p-i-n diode configuration. A growth interrupt technique was employed in order to avoid accumulation of excess surface bismuth. X-ray diffraction measurements showed that $GaAs_{1-x}Bi_x$ with x~0.06 can be grown up to at least 100 nm thick with negligible strain relaxation. The GaAsBi layers are highly uniform and free from the common phenomenon of phase separation; however transmission electron diffraction measurements show the presence of CuPt-type ordering.

The structures were processed into devices using a combination of photolithography and wet etching. The electrical characteristics of the devices were investigated using current-voltage and capacitance-voltage measurements. The absorption properties of the devices were systematically investigated by measuring the photocurrent both at a fixed wavelength of 1064 nm and over a range of wavelengths. The samples containing GaAsBi layers showed a photoresponse in the near-infrared up to almost 1.3 μm. The absorption coefficients of the layers were obtained from the responsivity data. Below the band gap, the absorption coefficients showed an exponential dependence on the photon energy (Urbach tailing).

The electroluminescence properties of the samples were also investigated. All samples showed room-temperature emission from the GaAsBi layers at wavelengths around 1.25 μm. The presence of localized states in the band gap was evident from taking electroluminescence measurements as a function of injection current and temperature.

List of publications

Journal papers

1. A. R. Mohmad, F. Bastiman, **C. J. Hunter**, J. S. Ng, S. J. Sweeney and J. P. R. David, "The effect of Bi composition to the optical quality of GaAsBi", *Appl. Phys. Lett*., vol. 99, p. 042107, 2011.
2. A. R. Mohmad, F. Bastiman, **C. J. Hunter**, R. D. Richards, S. J. Sweeney, J. S. Ng and J. P. R. David, "Effects of rapid thermal annealing on GaAsBi alloys", *Appl. Phys. Lett*., vol. 101, p. 012106, 2012.
3. S. L. Tan, **C. J. Hunter**, S. Zhang, L. J. J. Tan, Y. L. Goh, J. S. Ng, I. P. Marko, S. J. Sweeney, A. R. Adams, J. Allam, J. P. R. David, "Improved Optoelectronic Properties of Rapid Thermally Annealed Dilute Nitride GaInNAs Photodetectors", *Journal of Electron. Mater.*, vol. 41, pp. 3393-3401, 2012.
4. **C. J. Hunter**, F. Bastiman, A. R. Mohmad, R. Richards, J. S. Ng, S. J. Sweeney and J. P. R. David, "Absorption Characteristics of $GaAs_{1-x}Bi_x$/GaAs Diodes in the Near Infra-Red", *IEEE Photon. Technol. Lett.*, vol. 24, pp. 2191-2194, 2012.
5. D. F. Reyes, D. González, F. Bastiman, L. Dominguez, **C. J Hunter**, E. Guerrero, M. A. Roldan, A. Mayoral, J. P. R. David, D. L. Sales, "Photoluminescence Enhancement of InAs(Bi) Quantum Dots by Bi Clustering", *App. Phys. Express*, vol. 6, p. 042103, 2013.
6. R. D. Richards, F. Bastiman, **C. J. Hunter**, D. F. Mendes, A. R. Mohmad, J. S. Roberts, J. P. R. David, "Molecular beam epitaxy growth of GaAsBi using As_2 and As_4", *J. Cryst. Growth*, vol. 390, pp. 120-124, 2014.
7. D. F. Reyes, F. Bastiman, **C. J. Hunter**, A. M. Sanchez, R. Beanland, J. P. R. David, D. L. Sales, and D. Gonzalez, "Bismuth incorporation and the role of ordering in GaAsBi/GaAs structures," *Nanoscale Research Letters*, vol. 9, p. 23, 2014.
8. A. R. Mohmad, F. Bastiman, **C. J. Hunter**, R. D. Richards, S. J. Sweeney, J. S. Ng, J. P. R. David and B. Y. Majlis, "Localization effects and band gap of GaAsBi alloys", *submitted to Physica Status Solidi B*.
9. **C. J. Hunter**, F. Bastiman, A. R. Mohmad, R. Richards, R. Beanland and J. P. R. David, "Growth and characterisation of bulk GaAsBi/GaAs p-i-n diodes", *submitted to Journal of Crystal Growth*.

Oral and poster presentations

1. A. R. Mohmad, F. Bastiman, **C. J. Hunter**, J. S. Ng, S. J. Sweeney and J. P. R. David, "The effect of Bi composition to the optical quality of $GaAs_{1-x}Bi_x$ alloys", 2nd International Workshop on Bismuth Containing Semiconductors, Guildford, UK, 18 - 20 July 2011.
2. A. R. Mohmad, F. Bastiman, **C. J. Hunter**, R. D. Richards, S. J. Sweeney, J. S. Ng and J. P. R. David, "Effects of rapid thermal annealing on the optical and structural properties of $GaAs_{1-x}Bi_x$", Semiconductor and Integrated Optoelectronics Conference (SIOE) 2012, Cardiff, UK, 2 - 4 April 2012.
3. **C. J. Hunter**, F. Bastiman, A. R. Mohmad, R. D. Richards, J. S. Ng, S. J. Sweeney and J. P. R. David, "Absorption characteristics of $GaAs_{1-x}Bi_x$/GaAs diodes in the near infra-red", Semiconductor and Integrated Optoelectronics Conference (SIOE) 2012, Cardiff, UK, 2 - 4 April 2012.
4. F. Bastiman, **C. J. Hunter**, A. R. Mohmad, R. D. Richards, J. S. Ng, S. J. Sweeney and J. P. R. David, "Growth and characterisation of $GaAs_{1-x}Bi_x$ p-i-n diodes", EMRS Spring Meeting, Strasbourg, France, 14 - 18 May 2012.
5. R. D. Richards, F. Bastiman, **C. J. Hunter**, A. R. Mohmad, J. S. Ng and J. P. R. David, "Effect of arsenic species on growth of $GaAs_{1-x}Bi_x$", UK Semiconductors 2012, Sheffield, UK, 4 - 5 July 2012.
6. **C. J. Hunter**, F. Bastiman, A. R. Mohmad, R. D. Richards, J. S. Ng, S. J. Sweeney and J. P. R. David, "Optical and electrical properties of $GaAs_{1-x}Bi_x$/GaAs diodes", 3rd International Workshop on Bismuth Containing Semiconductors, Victoria, Canada, 15 - 18 July 2012.
7. A. R. Mohmad, F. Bastiman, **C. J. Hunter**, R. D. Richards, S. J. Sweeney, J. S. Ng and J. P. R. David, "The effect of growth parameters on the optical and structural quality of $GaAs_{1-x}Bi_x$ alloys", 17th International Conference on Molecular Beam Epitaxy, Nara, Japan, 23 - 28 September 2012.
8. F. Bastiman, A. R. Mohmad, R. D. Richards, **C. J. Hunter**, D. F. Mendes, D. F. Reyes, D. L. Sales, J. S. Ng and J. P. R. David, "Reconstruction orientated Bi incorporation mechanisms in GaAsBi/GaAs (100)", 17th European Molecular Beam Epitaxy Workshop, Levi, Finland, 10 - 13 March 2013.

9. R. Richards, F. Bastiman, **C. J. Hunter**, A. R. Mohmad, J. P. R. David and N. Ekins-Daukes, "GaAsBi MQWs for Multi-Junction Photovoltaics", 39th IEEE Photovoltaic Specialists Conference, Tampa, USA, 16 - 21 June 2013.
10. **C. J. Hunter**, F. Bastiman, A. R. Mohmad, R. Richards, R. Beanland and J. P. R. David, "TEM characterization of bulk GaAsBi layers", UK Semiconductors 2013, Sheffield, UK, 3 - 4 July 2013.
11. **C. J. Hunter**, R. Richards, F. Bastiman, A. R. Mohmad, and J. P. R. David, "Growth and characterization of p-i-n diodes containing multiple quantum well GaAsBi layers", 4th International Workshop on Bismuth Containing Semiconductors, Fayetteville, USA, 14 - 17 July 2013.

Chapter 1: Introduction

This section covers two main topics. First, a brief history of solar cells is given, with a particular focus on limits to efficiency and what can be done to overcome them. Second, existing semiconductor materials used for high-efficiency solar cells are covered and the potential of bismuth-containing semiconductors for this application is reviewed. A brief summary of the thesis is then given.

1.1 Solar cells

1.1.1 Overview

'Solar power' is a general term used to describe power generation from sunlight. Specifically this work is concerned with photovoltaic energy conversion, where sunlight is converted directly into electricity. The photovoltaic effect was first observed in 1839 by Becquerel [1]. There was not much focus on the energy applications of the effect until researchers at Bell Laboratories in the USA reported a solar cell consisting of a silicon p-n junction in 1954 [2]. Not long afterwards, researchers at RCA Laboratories reported on similar work using GaAs [3].

Solar power is now becoming an important method of generating electricity due to several factors. Increasing concern over the availability and environmental impacts of fossil fuels has led to interest in renewable energy sources, and in addition, solar cell efficiency has been increasing and the cost of solar power decreasing since the 1970s. While photovoltaics currently produce less than 1% of global energy demand, the installed capacity has increased more than ten-fold over the past 5 years (Figure 1.1).

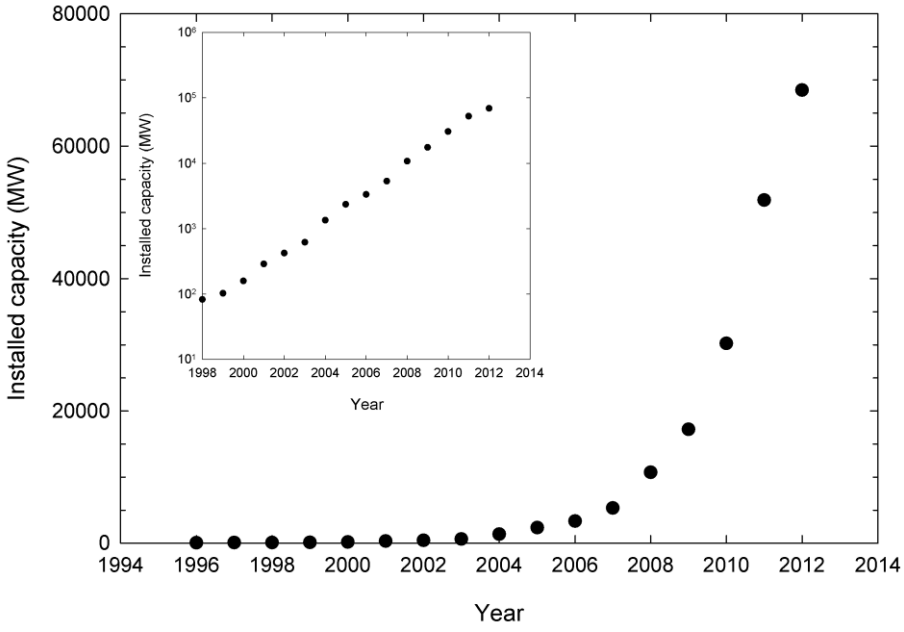

Figure 1.1: Global installed PV capacity from 1996-2012. The inset shows the data on a log scale. Data taken from BP Statistical Review of World Energy 2013 [4].

1.1.2 Types of solar cells

Silicon is the most commonly used material for solar cells. Although silicon does not absorb light well due to its indirect band gap, it is abundant in the Earth's crust and therefore relatively cheap. High quality silicon was also being produced in large quantities for the microelectronics market before the advent of solar cells, leading to mature production and processing techniques.

Other types of inorganic semiconductor solar cells are based on materials such as cadmium telluride (CdTe), copper indium gallium selenide (CIGS) and III-V semiconductors e.g. gallium arsenide. This last category is the focus of this work.

1.1.3 Solar cell processes

There are two main processes which must occur in semiconductor solar cells in order to generate electricity. First, a photon with energy greater than the band gap energy excites an electron from the valence band into the conduction band, leaving a hole in the valence band. The electron and hole must then be separated and extracted from the cell before they can recombine. In a semiconductor solar cell, this is achieved by using a structure with a built-in electric field, such as a p-n or p-i-n junction. These processes are illustrated in Figure 1.2.

The magnitude of the energy barrier between the p-type and n-type regions at equilibrium is given by qV_{bi}, where q is the charge on an electron and V_{bi} is the built-in voltage of the junction. Under illumination, the net barrier also depends on the voltage, V, which is derived from the photocurrent. The total barrier is $q(V_{bi}-V)$.

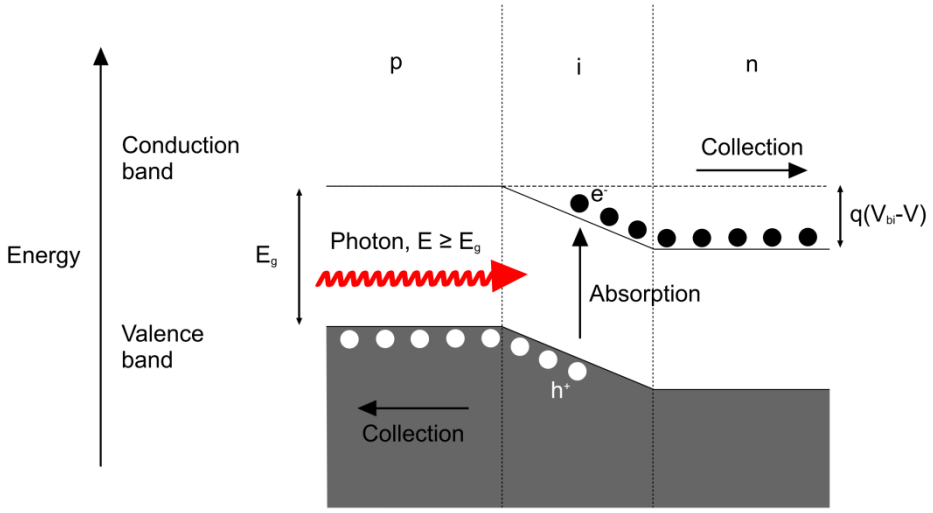

Figure 1.2: The photovoltaic process in a semiconductor solar cell.

1.1.4 Solar cell efficiency

A crucial metric of a solar cell's performance is its efficiency, which is defined as the electrical power generated by the cell divided by the optical power incident on the cell. In order to make consistent measurements of the efficiency, it is necessary to define a standard solar spectrum. The Sun's light is strongly absorbed by the atmosphere at certain wavelength bands, and this is taken into account by using a quantity known the air mass ratio, A. This is defined as the path length taken by sunlight through the Earth's atmosphere relative to the path length when the Sun is directly overhead. For an observer at sea level, this has a value of 1 when the Sun is directly overhead. Radiation outside the atmosphere, i.e. in outer space, has $A = 0$. The value of A increases with increasing angle away from the zenith. An air mass value of 1.5 is considered standard for solar cell calibration. Figure 1.3 shows AM 0 and AM 1.5 spectra taken from the American Society for Testing and Materials (ASTM) website [5].

The Sun can be approximated as a black body with a temperature of 5800 K. The spectral irradiance of the Sun was calculated using Planck's law, taking into account the size of the Sun and the distance between the Sun and the Earth. This is shown in Figure 1.3 as a comparison.

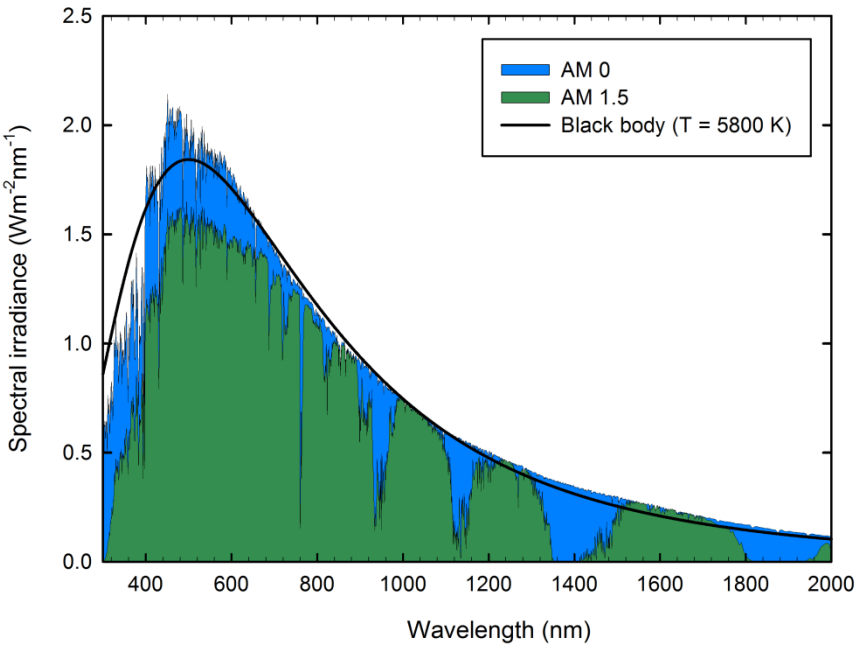

Figure 1.3: Comparison of a black body spectrum with solar radiation outside the atmosphere (AM0) and at sea level (AM1.5).

Once a standard solar spectrum has been defined, it is necessary to consider the loss mechanisms within the cell. Five intrinsic loss mechanisms for an ideal single junction solar cell are detailed in [6] and are summarized here. First, there is a loss due to the finite difference in temperature between the Sun and the cell. Assuming the Sun to be at T = 5800 K and the solar cell to be at T = 300 K, the Carnot efficiency is given by

$$\eta_{Carnot} = \left(1 - \frac{T_{cell}}{T_{sun}}\right) \times 100\% = 95\% \tag{1.1}$$

This is an important result as it shows that the efficiency can never reach 100%, no matter what type of cell is used.

Second, since the cell is operating in forward bias it will emit light, therefore some carriers will be lost to emission. Also, while the cell absorbs light from a small solid angle it emits light in all directions, and thus there is a difference in the absorption and emission angles. This leads to an additional entropic loss process.

All of these loss mechanisms make relatively small reductions to the maximum efficiency. The two most important loss mechanisms both depend directly on the magnitude of the cell band gap, E_g. Photons with energy less than the band gap energy cannot be absorbed by the cell,

while photons with energy greater than the band gap energy generate 'hot' electrons and holes which thermalize to the band edges, so that the excess energy of the photons is wasted. Changing the magnitude of the band gap will reduce the effect of one of these loss mechanisms while increasing the effect of the other. Thus, there is an optimum band gap value which will give maximum power conversion efficiency. Shockley and Queisser [7] determined this value to be 1.1 eV, assuming the Sun and Earth to be black bodies with temperatures of 6000 K and 300 K respectively. This band gap gives an efficiency of 30%. Since this original paper many different efficiency values have been determined, using different conditions and assumptions. A review of these is given in [8].

1.1.5 Concentration

One way to exceed the efficiency limit is to concentrate the sunlight incident on the cell, which reduces the mismatch between the angles of absorption and emission. This is achieved by using mirrors and/or lenses to focus the light, along with tracking systems which adjust the positioning of the cells throughout the day to follow the Sun. This also reduces the amount of material needed to produce a given amount of electricity, which is important for material systems such as III-V semiconductors where material costs are high. At maximum concentration Shockley and Quiesser found the limiting efficiency to be 44% (for a single-junction cell) [7]. In addition, for non-ideal cells there is a reduction in efficiency from non-radiative recombination due to defects. Concentrating the light gives a large photocurrent, which saturates these defects and reduces their effect [9].

1.1.6 Multi-junction solar cells

Another way to exceed the single-junction limit is to use a cell with two or more junctions connected in series, an approach first considered theoretically by Henry [10]. This allows each cell to capture a portion of the solar spectrum, and reduces the energy that is wasted.

For AM 1.5 direct normal irradiance, the limiting efficiency for a cell with an infinite number of junctions was found to be 65.4% [11]. Multi-junction cells are commonly grown in a single structure, termed a monolithic cell. The junctions are arranged in order of decreasing band gap, with the largest band gap material at the top of the cell. The optimum band gap values are chosen so that each cell produces the same current, and they vary with the number of junctions used. This method is often used in combination with solar concentration, in which case the band gap values will also depend on the concentration factor. In the case of maximum

concentration, the limiting efficiency for a cell with an infinite number of junctions increases to 85% [11].

In practice however, the choice of materials used is dictated not just by the band gaps required, but also by the lattice constants of the materials. To grow a monolithic multi-junction solar cell, it is necessary to use a combination of materials which have similar lattice constants - materials with the same lattice constant are referred to as 'lattice matched'. Using materials with different lattice constants typically causes dislocations to be introduced into the cell. This leads to states within the band gap which trap carriers and reduce efficiency. However this can sometimes be offset by the gain in efficiency due to the band gap combinations being closer to the optimum values.

An efficiency of over 30% has been reported for a lattice-matched tandem cell [12], while efficiencies above 40% were first reported in 2007 for both lattice-matched and lattice-mismatched triple junction cells [13]. In general however, the constraint of lattice matching further limits the efficiency of multi-junction solar cells, as a combination of materials that is lattice-matched or near lattice-matched will not necessarily possess the optimum band gap values.

In order to increase efficiency still further, a multi-junction cell containing four junctions could be used. A band gap of 1 eV has been predicted to be the optimum value for an additional fourth junction [14, 15]. No binary III-V compound with this band gap exists; therefore it is necessary to look at ternary or quaternary compounds where the band gap can be adjusted to this value. Some possible material combinations are explored in the next section.

1.2 III-V compounds

Groups III, IV and V of the periodic table are shown in Table 1.1. (Officially these have been renamed 13, 14 and 15; however the Roman numeral notation is still used [16]). Elements that are commonly used to produce III-V compounds are highlighted in blue. Over the past two decades, there has been interest in incorporating elements such as nitrogen and bismuth into existing III-V compounds, particularly GaAs. Due to the large differences in atomic radius and electronegativity between these elements and arsenic, unusual electronic properties of the alloys are observed. The most obvious of these is the change in band gap with composition, which is covered in the next section.

III	IV	V
B	C	N
Al	Si	P
Ga	Ge	As
In	Sn	Sb
Tl	Pb	Bi

Table 1.1: Groups III, IV and V of the periodic table.

1.2.1 Band gaps of ternary III-V compounds and the band anticrossing model

Ternary compounds are commonly referred to using subscripts to denote the relative concentrations of the constituent compounds, ie. $A_xB_{1-x}C$, where x takes values between 0 and 1. For convenience the subscripts are often omitted; in this thesis the term GaAsBi is used throughout rather than $GaAs_{1-x}Bi_x$.

The band gap of a conventional ternary III-V compound $A_xB_{1-x}C$ can be described by a linear interpolation between the end compounds *AC* and *BC*, with the addition of a bowing parameter, *b* [17]:

$$E_g(A_xB_{1-x}C) = xE_g(AC) + (1-x)E_g(BC) - bx(1-x) \tag{1.2}$$

The bowing parameter is typically less than 1 eV. However when equation (1.2) is applied to gallium arsenide nitride (GaAsN), values of *b* as large as 25 eV are found [17], and the bowing parameter is also observed to vary with composition. The band gap reduction is therefore not adequately described by equation (1.2). Instead, a model known as the band anticrossing (BAC) model was proposed [18]. This model assumes an interaction between localized nitrogen states with energy E_N and the conduction band states of the host matrix, with the energy of the conduction band edge given by E_M. (Both energies are given relative to the valence band maximum whose energy is taken to be zero). This interaction leads to the splitting of the conduction band into two sub-bands $E_{\pm}$, whose energies are given by the equation

$$E_{\pm} = \frac{\left(E_N + E_M \pm [(E_N - E_M)^2 + 4V_{MN}^2]^{1/2}\right)}{2} \tag{1.3}$$

where V_{MN} is the strength of the interaction between E_N and E_M. This is dependent on the square root of the nitrogen concentration, *x* [19]:

$$\mathrm{V_{MN}} = \mathrm{C_{MN}x^{1/2}} \tag{1.4}$$

C_{MN} is a constant which depends on the host semiconductor.

The energy of the new conduction band edge is given by E_-. Thus the band gap for a given nitrogen composition can be calculated, assuming nitrogen incorporation has no effect on the valence band. The validity of this model was confirmed by observations of optical transitions involving the E_+ band using reflectance methods [18, 20].

Figure 1.4 shows how the band gaps of various ternary compounds based on GaAs vary with composition. The original calculations were carried out by fitting to experimental band gap data for pseudomorphic epitaxial layers and have been reproduced here.

The band gap of InGaAs was calculated using equation (1.2) with a bowing coefficient taken from [17]. For GaAsSb, the band gap was determined from a weighted average of the band gaps $E_g^{As\text{-}rich}$ and $E_g^{Sb\text{-}rich}$ (which are calculated by the valence and conduction band anticrossing models respectively) following the procedure used in [21]. For GaAsN the conduction band anticrossing model was used [19]. The exact method used for GaAsBi is described in detail in section 1.2.3.

It can be seen that the reduction in band gap achieved using nitrogen and bismuth is much greater than for indium or antimony. As mentioned previously, this is due to the large difference in size and electronegativity between N/Bi and As atoms.

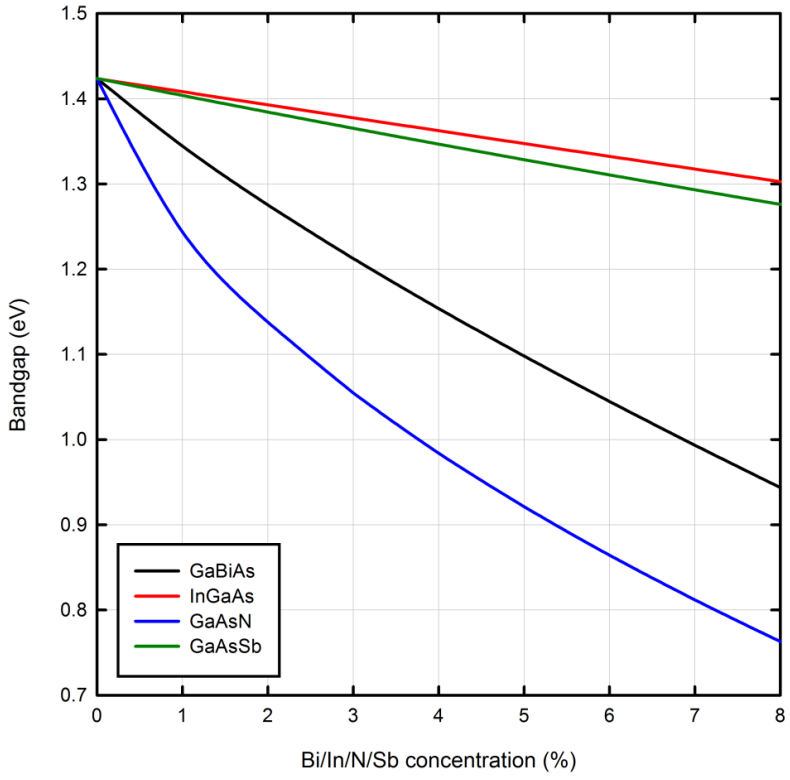

Figure 1.4: Band gaps of various pseudomorphic ternary III-V compounds.

1.2.2 Gallium arsenide nitride

GaN has a large band gap of around 3.4 eV and thus it might be expected that the band gap of GaAsN would increase with increasing nitrogen concentration. The giant bowing of the band gap that is in fact observed [22, 23] offers the possibility of accessing the near-infrared region of the electromagnetic spectrum using relatively small amounts of nitrogen.

Adding indium as well as nitrogen to GaAs gives the quaternary alloy indium gallium nitride arsenide ($In_xGa_{1-x}As_{1-y}N_y$) which is lattice matched to GaAs when $y \approx 0.35x$ [15]. Since adding indium also reduces the band gap, less nitrogen must be added to obtain a given band gap value. InGaAsN with a 1 eV band gap can be grown lattice matched to GaAs or Ge, and as such would appear to be an ideal candidate for use in multi-junction solar cells. Its use in such devices has been demonstrated [15, 24]; however achieving high material quality has proved difficult. This is in part due to the necessity of using low growth temperatures, but also due to the manner of nitrogen incorporation. Nitrogen has been found to incorporate at interstitial sites [25], which leads to the formation of defect states in the band gap. Such states will reduce the photoluminescence efficiency [26], the minority carrier diffusion length [27] and the electron mobility [28]. These properties can be improved by postgrowth thermal annealing [29, 30], which is believed to remove some of the structural defects. Despite these problems, this material has been used in a multijunction solar cell with an efficiency of 44% under concentration, which at the time was a world record [31].

1.2.3 Gallium arsenide bismide

Over the last decade there has been much interest in incorporating bismuth into GaAs, which like nitrogen also reduces the band gap [32, 33]. A reduction in band gap is expected due to the predicted semi-metallic character of GaBi [34], however the reduction displays a large bowing in a similar manner to that observed for GaAsN. This bowing can also be explained by the BAC model.

In GaAsBi, localized bismuth states are introduced into the valence band instead of the conduction band. In this case, equation (1.3) can be rewritten as

$$E_{\pm} = \frac{\left(E_{Bi} \pm \left[{E_{Bi}}^2 + 4V_{MN}^2\right]^{1/2}\right)}{2} \tag{1.5}$$

since E_M is the energy of the valence band maximum which is taken to be zero.

This induces a splitting of the light-hole (LH) and heavy-hole (HH) bands into sub bands LH $E_{\pm}$ and HH $E_{\pm}$ [21, 35]. This is illustrated in Figure 1.5 for the GaAs light-hole band, using the parameters given in [35]. The higher energy band edge E_{+} becomes the new valence band maximum.

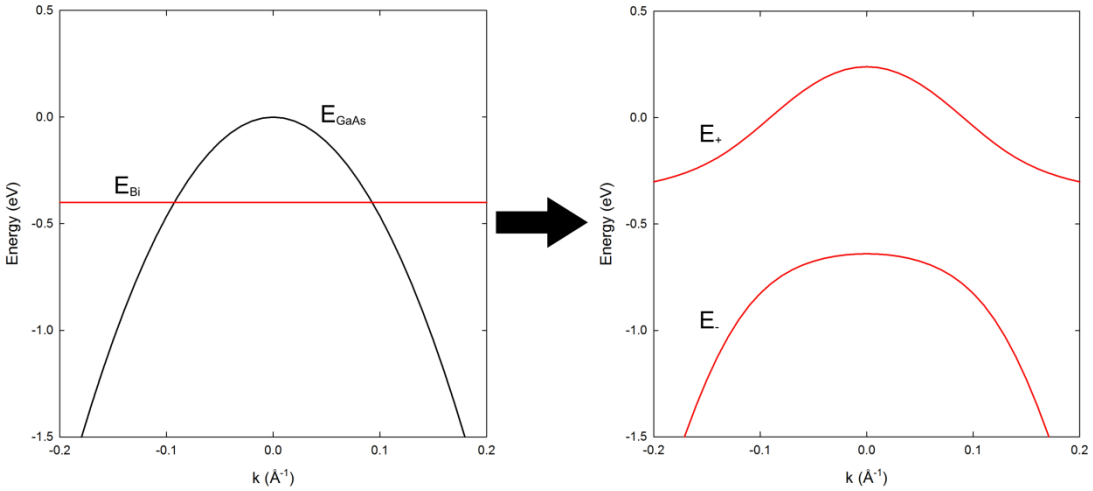

Figure 1.5: Band diagrams showing the valence band of GaAs and the localized Bi level (left) and the resulting E_{+} and E_{-} levels for [Bi] = 6% (right).

However, there have been no experimental observations of the E_{-} band. This is due to the resonant Bi levels being broadened due to the interaction with the large density of valence band states, along with the presence of defect levels due to Bi pairs and clusters [36].

The BAC model for GaAsBi assumes that the anticrossing interaction occurs with the valence band only and thus that the band gap reduction is caused purely by the upward movement of the valence band. There has therefore been uncertainty about the conduction band alignment of GaAsBi with GaAs. It has been suggested [36, 37] that while the shift in valence band is described by the BAC interaction, the conduction band also undergoes a linear reduction in energy, giving a type I alignment. This has been supported by experimental studies [38].

Taking this into account, the band gap as a function of Bi content is described by the equation

$$E_{\mathrm{GaAsBi}} = E_{\mathrm{GaAs}} - \frac{\left(E_{Bi} + \left[{E_{Bi}}^2 + 4V_{MN}^2\right]^{1/2}\right)}{2} - 100x\Delta_{CB} \qquad (1.6)$$

where x is the Bi fraction and Δ_{CB} is the reduction in conduction band energy per % Bi. The parameters used in [35] are E_{Bi} = -0.4 eV, C_{Bi} = 1.6 eV and Δ_{CB} = 23meV/%Bi.

Besides the band gap reduction, GaAsBi has other properties that are desirable for device applications. The spin-orbit splitting, Δ_{SO}, of a III-V compound increases as Z^4, where Z is the atomic number of the group V element [39]. Since bismuth is the heaviest group V element, GaBi is predicted to have a large spin-orbit splitting of 2.2 eV [40], leading to an increase in Δ_{SO} with bismuth content. This effect has the potential to reduce CHSH Auger recombination in lasers (where a hole gives its energy to another hole when recombining with an electron) when $\Delta_{SO} > E_g$ [41]. This crossover has been shown to occur for Bi concentrations above 10% [42], although no devices with such high Bi content have been reported at present. The band gap of GaAsBi also exhibits lower sensitivity to temperature than GaAs which could lead to lower cooling requirements for GaAsBi based devices [43].

Most work on GaAsBi in the literature has focused on material growth and characterization; however there have been a few reports of devices in recent years. GaAsBi has been used to form the active region in LEDs [38, 44] and optically-pumped lasers [45]. An electrically-pumped laser has recently been demonstrated [46].

Other bismuth containing alloys such as InAsBi [47], InGaAsBi [48, 49], BGaAsBi [50], GaSbBi [51, 52] and GaAsBiN [53] have been reported. GaAsBiN is covered in more detail in section 1.2.4.

1.2.4 Gallium arsenide bismide nitride (GaAsBiN)

The co-alloying of nitrogen and bismuth in GaAs to form GaAsBiN was first proposed by Janotti et al. [34]. This material is of interest for solar cells as it is possible to produce an alloy with a 1 eV band gap that is lattice matched to GaAs/Ge, as with InGaAsN. As the addition of Bi causes a larger band gap reduction than In, using Bi instead of In reduces the amount of N required for a lattice matched 1 eV junction, which may improve material quality. GaAsNBi was first grown in 2004 [54], and a photoluminescence wavelength of 1.3 μm was obtained [53]. Incorporation of N was found to reduce the photoluminescence intensity compared to samples containing Bi only; however post-growth annealing was shown to increase it slightly. Growth of several samples with different compositions led to a formula for N and Bi concentrations needed for lattice matching, which is $Ga(N_{0.33}Bi_{0.67})_zAs_{1-z}$ [55]. Growth was also reported in [56]. Besides adjusting the band gap, using Bi and N together allows control of strain, spin-orbit splitting and the conduction-band and valence-band offsets [39].

1.3 Overview of thesis

In this work, the growth and characterization of p-i-n diodes containing undoped GaAsBi layers with a 1 eV band gap is explored, with specific reference to detection applications such as solar cells. Ideally the layers would be lattice matched to GaAs/Ge using nitrogen; however the MBE system used in this work does not possess a nitrogen source. Therefore this thesis explores the properties of GaAsBi with a 1 eV band gap as preparation for future work based on GaAsBiN.

Chapter 2 gives an overview of MBE and the specifics of the system used to grow the samples in this work, as well as the fabrication methods used to process the as-grown structures into working devices. Chapter 3 details the various techniques which were used to characterize the devices. Since growth of GaAsBi is non-trivial, chapter 4 explains the issues involved and describes a method used to grow thick GaAsBi layers with the Bi content required for a 1 eV band gap (~6%). The GaAsBi layers are grown within diode structures, which allows device characteristics to be evaluated. Chapter 5 reports the electrical characteristics and absorption properties of the samples, while chapter 6 reports electroluminescence characteristics of the samples. Chapter 7 summarizes the results and outlines suggestions for future work.

1.4 References

[1] E. Becquerel, "Mémoire sur les effets électriques produits sous l'influence des rayons solaires," *Comptes Rendus*, vol. 9, pp. 561-567, 1839.

[2] D. M. Chapin, C. S. Fuller, and G. L. Pearson, "A New Silicon p-n Junction Photocell for Converting Solar Radiation into Electrical Power," *J. Appl. Phys.*, vol. 25, pp. 676-677, 1954.

[3] D. A. Jenny, J. J. Loferski, and P. Rappaport, "Photovoltaic Effect in GaAs p-n Junctions and Solar Energy Conversion," *Phys. Rev.*, vol. 101, pp. 1208-1209, 1956.

[4] BP. (2013). *BP statistical review of world energy June 2013*. Available: http://www.bp.com/en/global/corporate/about-bp/statistical-review-of-world-energy-2013.html

[5] American Society for Testing and Materials. (2002). *Reference solar spectral irradiance: air mass 1.5*. Available: http://rredc.nrel.gov/solar/spectra/am1.5/

[6] L. C. Hirst and N. J. Ekins-Daukes, "Fundamental losses in solar cells," *Prog. Photovoltaics*, vol. 19, pp. 286-293, 2011.

[7] W. Shockley and H. J. Queisser, "Detailed Balance Limit of Efficiency of p-n Junction Solar Cells," *J. Appl. Phys.*, vol. 32, pp. 510-519, 1961.

[8] P. T. Landsberg and V. Badescu, "Solar energy conversion: list of efficiencies and some theoretical considerations Part II—Results," *Progress in Quantum Electronics*, vol. 22, pp. 231-255, 1998.

[9] S. M. Vernon, S. P. Tobin, V. E. Haven, L. M. Geoffroy, and M. M. Sanfacon, "High-efficiency concentrator cells from GaAs on Si," in *Photovoltaic Specialists Conference, 1991, Conference Record of the Twenty Second IEEE*, 1991, pp. 353-357.

[10] C. H. Henry, "Limiting efficiencies of ideal single and multiple energy gap terrestrial solar cells," *J. Appl. Phys.*, vol. 51, pp. 4494-4500, 1980.

[11] A. Martí and G. L. Araújo, "Limiting efficiencies for photovoltaic energy conversion in multigap systems," *Solar Energy Materials and Solar Cells*, vol. 43, pp. 203-222, 1996.

[12] T. Takamoto, E. Ikeda, H. Kurita, and M. Ohmori, "Over 30% efficient InGaP/GaAs tandem solar cells," *Appl. Phys. Lett.*, vol. 70, pp. 381-383, 1997.

[13] R. R. King, D. C. Law, K. M. Edmondson, C. M. Fetzer, G. S. Kinsey, H. Yoon, R. A. Sherif, and N. H. Karam, "40% efficient metamorphic GaInP/GaInAs/Ge multijunction solar cells," *Appl. Phys. Lett.*, vol. 90, pp. 183516-3, 2007.

[14] D. J. Friedman and S. R. Kurtz, "Breakeven criteria for the GaInNAs junction in GaInP/GaAs/GaInNAs/Ge four-junction solar cells," *Prog. Photovoltaics*, vol. 10, pp. 331-344, 2002.

[15] D. J. Friedman, J. F. Geisz, S. R. Kurtz, and J. M. Olson, "1-eV solar cells with GaInNAs active layer," *J. Cryst. Growth*, vol. 195, pp. 409-415, 1998.

[16] E. Fluck, "New notations in the periodic table," *Pure Appl. Chem.*, vol. 60, pp. 431-436, 1988.

[17] I. Vurgaftman, J. R. Meyer, and L. R. Ram-Mohan, "Band parameters for III--V compound semiconductors and their alloys," *J. Appl. Phys.*, vol. 89, pp. 5815-5875, 2001.

[18] W. Shan, W. Walukiewicz, J. W. Ager, E. E. Haller, J. F. Geisz, D. J. Friedman, J. M. Olson, and S. R. Kurtz, "Band Anticrossing in GaInNAs Alloys," *Phys. Rev. Lett.*, vol. 82, p. 1221, 1999.

[19] W. Shan, W. Walukiewicz, K. M. Yu, J. W. Ager Iii, E. E. Haller, J. F. Geisz, D. J. Friedman, J. M. Olson, S. R. Kurtz, H. P. Xin, and C. W. Tu, "Band Anticrossing in III–N–V Alloys," *phys. stat. sol. (b)*, vol. 223, pp. 75-85, 2001.

[20] C. Skierbiszewski, "Experimental studies of the conduction-band structure of GaInNAs alloys," *Semicond. Sci. Technol.*, vol. 17, p. 803, 2002.

[21] K. Alberi, J. Wu, W. Walukiewicz, K. M. Yu, O. D. Dubon, S. P. Watkins, C. X. Wang, X. Liu, Y. J. Cho, and J. Furdyna, "Valence-band anticrossing in mismatched III-V semiconductor alloys," *Phys. Rev. B*, vol. 75, p. 045203, 2007.

[22] M. Weyers, M. Sato, and H. Ando, "Red Shift of Photoluminescence and Absorption in Dilute GaAsN Alloy Layers," *Jpn. J. Appl. Phys.*, vol. 31, p. L853, 1992.

[23] S. Wei and A. Zunger, "Giant and Composition-Dependent Optical Bowing Coefficient in GaAsN Alloys," *Phys. Rev. Lett.,* vol. 76, p. 664, 1996.

[24] S. R. Kurtz, A. A. Allerman, E. D. Jones, J. M. Gee, J. J. Banas, and B. E. Hammons, "InGaAsN solar cells with 1.0 eV band gap, lattice matched to GaAs," *Appl. Phys. Lett.,* vol. 74, pp. 729-731, 1999.

[25] S. G. Spruytte, C. W. Coldren, J. S. Harris, W. Wampler, P. Krispin, K. Ploog, and M. C. Larson, "Incorporation of nitrogen in nitride-arsenides: Origin of improved luminescence efficiency after anneal," *J. Appl. Phys.,* vol. 89, pp. 4401-4406, 2001.

[26] T. K. Ng, S. F. Yoon, S. Z. Wang, W. K. Loke, and W. J. Fan, "Photoluminescence characteristics of GaInNAs quantum wells annealed at high temperature," *J. Vac. Sci. Technol., B,* vol. 20, pp. 964-968, 2002.

[27] S. R. Kurtz, A. A. Allerman, C. H. Seager, R. M. Sieg, and E. D. Jones, "Minority carrier diffusion, defects, and localization in InGaAsN, with 2% nitrogen," *Appl. Phys. Lett.,* vol. 77, pp. 400-402, 2000.

[28] M. Reason, Y. Jin, H. A. McKay, N. Mangan, D. Mao, R. S. Goldman, X. Bai, and C. Kurdak, "Influence of N on the electronic properties of GaAsN alloy films and heterostructures," *J. Appl. Phys.,* vol. 102, 2007.

[29] S. L. Tan, C. J. Hunter, S. Zhang, L. J. J. Tan, Y. L. Goh, J. S. Ng, I. P. Marko, S. J. Sweeney, A. R. Adams, J. Allam, and J. P. R. David, "Improved Optoelectronic Properties of Rapid Thermally Annealed Dilute Nitride GaInNAs Photodetectors," *J. Electron. Mater.,* vol. 41, pp. 3393-3401, 2012.

[30] A. Khan, "Correlation of nitrogen related traps in InGaAsN with solar cell properties," *Appl. Phys. Lett.,* vol. 90, p. 243509, 2007.

[31] M. A. Green, K. Emery, Y. Hishikawa, W. Warta, and E. D. Dunlop, "Solar cell efficiency tables (version 41)," *Prog. Photovoltaics,* vol. 21, pp. 1-11, 2013.

[32] S. Francoeur, M. J. Seong, A. Mascarenhas, S. Tixier, M. Adamcyk, and T. Tiedje, "Band gap of $GaAs_{1-x}Bi_x$, $0 < x < 3.6\%$," *Appl. Phys. Lett.,* vol. 82, pp. 3874-3876, 2003.

[33] X. Lu, D. A. Beaton, R. B. Lewis, T. Tiedje, and Y. Zhang, "Composition dependence of photoluminescence of $GaAs_{1-x}Bi_x$ alloys," *Appl. Phys. Lett.,* vol. 95, pp. 041903-3, 2009.

[34] A. Janotti, S. Wei, and S. B. Zhang, "Theoretical study of the effects of isovalent coalloying of Bi and N in GaAs," *Phys. Rev. B,* vol. 65, p. 115203, 2002.

[35] K. Alberi, O. D. Dubon, W. Walukiewicz, K. M. Yu, K. Bertulis, and A. Krotkus, "Valence band anticrossing in $GaBi_xAs_{1-x}$," *Appl. Phys. Lett.,* vol. 91, pp. 051909-3, 2007.

[36] M. Usman, C. A. Broderick, Z. Batool, K. Hild, T. J. C. Hosea, S. J. Sweeney, and E. P. O'Reilly, "Impact of alloy disorder on the band structure of compressively strained $GaBi_xAs_{1-x}$," *Phys. Rev. B,* vol. 87, p. 115104, 2013.

[37] M. Usman, C. A. Broderick, A. Lindsay, and E. P. O'Reilly, "Tight-binding analysis of the electronic structure of dilute bismide alloys of GaP and GaAs," *Phys. Rev. B,* vol. 84, p. 245202, 2011.

[38] N. Hossain, I. P. Marko, S. R. Jin, K. Hild, S. J. Sweeney, R. B. Lewis, D. A. Beaton, and T. Tiedje, "Recombination mechanisms and band alignment of $GaAs_{1-x}Bi_x$/GaAs light emitting diodes," *Appl. Phys. Lett.,* vol. 100, pp. 051105-3, 2012.

[39] S. J. Sweeney and S. R. Jin, "Bismide-nitride alloys: Promising for efficient light emitting devices in the near- and mid-infrared," *J. Appl. Phys.,* vol. 113, pp. 043110-6, 2013.

[40] Y. Zhang, A. Mascarenhas, and L. W. Wang, "Similar and dissimilar aspects of III-V semiconductors containing Bi versus N," *Phys. Rev. B,* vol. 71, p. 155201, 2005.

[41] C. A. Broderick, M. Usman, S. J. Sweeney, and E. P. O'Reilly, "Band engineering in dilute nitride and bismide semiconductor lasers," *Semicond. Sci. Technol.,* vol. 27, p. 094011, 2012.

[42] Z. Batool, K. Hild, T. J. C. Hosea, X. Lu, T. Tiedje, and S. J. Sweeney, "The electronic band structure of GaBiAs/GaAs layers: Influence of strain and band anti-crossing," *J. Appl. Phys.,* vol. 111, pp. 113108-7, 2012.

[43] A. R. Mohmad, F. Bastiman, J. S. Ng, S. J. Sweeney, and J. P. R. David, "Photoluminescence investigation of high quality $GaAs_{1-x}Bi_x$ on GaAs," *Appl. Phys. Lett.,* vol. 98, p. 122107, 2011.

[44] R. B. Lewis, D. A. Beaton, X. Lu, and T. Tiedje, "$GaAs_{1-x}Bi_x$ light emitting diodes," *J. Cryst. Growth,* vol. 311, pp. 1872-1875, 2009.

[45] Y. Tominaga, K. Oe, and M. Yoshimoto, "Low Temperature Dependence of Oscillation Wavelength in $GaAs_{1-x}Bi_x$ Laser by Photo-Pumping," *Appl. Phys. Express,* vol. 3, p. 062201, 2010.

[46] P. Ludewig, N. Knaub, N. Hossain, S. Reinhard, L. Nattermann, I. P. Marko, S. R. Jin, K. Hild, S. Chatterjee, W. Stolz, S. J. Sweeney, and K. Volz, "Electrical injection Ga(AsBi)/(AlGa)As single quantum well laser," *Appl. Phys. Lett.,* vol. 102, pp. 242115-3, 2013.

[47] S. P. Svensson, H. Hier, W. L. Sarney, D. Donetsky, D. Wang, and G. Belenky, "Molecular beam epitaxy control and photoluminescence properties of InAsBi," *J. Vac. Sci. Technol., B,* vol. 30, pp. 02B109-5, 2012.

[48] G. Feng, K. Oe, and M. Yoshimoto, "Bismuth containing III–V quaternary alloy InGaAsBi grown by MBE," *phys. stat. sol. (a),* vol. 203, pp. 2670-2673, 2006.

[49] Y. Zhong, P. B. Dongmo, J. P. Petropoulos, and J. M. O. Zide, "Effects of molecular beam epitaxy growth conditions on composition and optical properties of $In_xGa_{1-x}Bi_yAs_{1-y}$," *Appl. Phys. Lett.,* vol. 100, pp. 112110-4, 2012.

[50] D. A. Beaton, A. J. Ptak, K. Alberi, and A. Mascarenhas, "Quaternary bismide alloy lattice matched to GaAs," *J. Cryst. Growth,* vol. 351, pp. 37-40, 2012.

[51] Y. Song, S. Wang, I. S. Roy, P. Shi, and A. Hallen, "Growth of $GaSb_{1-x}Bi_x$ by molecular beam epitaxy," *J. Vac. Sci. Technol., B,* vol. 30, pp. 02B114-7, 2012.

[52] M. K. Rajpalke, W. M. Linhart, M. Birkett, K. M. Yu, D. O. Scanlon, J. Buckeridge, T. S. Jones, M. J. Ashwin, and T. D. Veal, "Growth and properties of GaSbBi alloys," *Appl. Phys. Lett.,* vol. 103, p. 142106, 2013.

[53] W. Huang, M. Yoshimoto, Y. Takehara, J. Saraie, and K. Oe, "GaNAsBi Alloy Lattice Matched to GaAs with 1.3 um Photoluminescence Emission," *Jpn. J. Appl. Phys.,* vol. 43, p. L1350, 2004.

[54] M. Yoshimoto, W. Huang, Y. Takehara, J. Saraie, A. Chayahara, Y. Horino, and K. Oe, "New Semiconductor GaNAsBi Alloy Grown by Molecular Beam Epitaxy," *Jpn. J. Appl. Phys.,* vol. 43, p. L845, 2004.

[55] W. Huang, K. Oe, G. Feng, and M. Yoshimoto, "Molecular-beam epitaxy and characteristics of $GaN_yAs_{1-x-y}Bi_x$," *J. Appl. Phys.,* vol. 98, pp. 053505-6, 2005.

[56] S. Tixier, S. E. Webster, E. C. Young, T. Tiedje, S. Francoeur, A. Mascarenhas, P. Wei, and F. Schiettekatte, "Band gaps of the dilute quaternary alloys $GaN_xAs_{1-x-y}Bi_y$ and $Ga_{1-y}In_yN_xAs_{1-x}$," *Appl. Phys. Lett.,* vol. 86, pp. 112113-3, 2005.

Chapter 2: Molecular Beam Epitaxy and Device Fabrication

2.1 Introduction

In this chapter, the basics of molecular beam epitaxy are described, and the specific characteristics of the growth setup used in this work are explained. The processing steps used to fabricate device structures into working devices are also detailed.

2.2 Molecular beam epitaxy

Epitaxy is the process of depositing a crystalline film onto a crystalline substrate in an ordered manner, so that the film adopts the lattice structure of the substrate. If the deposited material is the same as that of the substrate, the process is termed homoepitaxy; if it is different, it is termed heteroepitaxy.

Molecular beam epitaxy (MBE) is one of several epitaxial growth techniques which are commonly used for the production of semiconductors. These include liquid phase epitaxy (LPE) and metal-organic vapour phase epitaxy (MOVPE). In MBE, the substrate is placed in a vacuum chamber which is held under ultra-high vacuum ($<10^{-9}$ mbar). Samples of elements to be deposited are placed in separate cells connected to the chamber and heated so that they sublime on to the substrate. Due to the vacuum, they should not encounter any other gaseous species before they reach the substrate and should thus be emitted in a 'beam', hence the term molecular beam epitaxy. When the molecules are present on the substrate surface, they can react and form a new layer of the crystal.

2.2.1 History of MBE

MBE was invented in the late 1960s and was developed rapidly in the next few years. The technique first came about through the study of the interaction of molecular beams of Ga and As_2 with GaAs substrates in ultra-high vacuum [1]. By maintaining an overpressure of As_2, all the Ga atoms present on the substrate surface were found to react to form a new monolayer of GaAs. The new technique was used to confirm theoretical predictions concerning electron confinement: in 1973 a superlattice structure composed of alternating layers of AlGaAs

'sandwiched' between GaAs layers was grown [2]. Since the band gap of AlGaAs increases with aluminium composition, the electrons in the GaAs layers are confined by potential barriers. Optical absorption measurements on similar structures showed that the energy states in the GaAs layer were quantized and thus that the electrons were confined [3].

2.2.2 Experimental set-up

In a typical MBE setup, the sample is placed in the centre of a growth chamber, with various material sources and analysis devices placed in ports around the chamber wall. The chamber contains a panel which is cooled using liquid nitrogen, which helps remove gaseous impurities. The source cells are usually made from pyrolytic boron nitride, as this material has high thermal conductivity and has minimal outgassing at high temperatures. Group III sources produce monatomic species (e.g. Ga, In), whereas most group V elements produce tetramers (e.g. P_4, As_4). A cracker can be used in order to break the tetramers down into dimers.

The flux from a cell can be regulated simply by opening and closing a shutter covering it. The shutters should not be too close to the cell however, as this can lead to thermal radiation being reflected back inside the cell, which increases its temperature [4]. The cells are thermally isolated from one another so that their temperatures can be controlled individually.

The sample is heated either directly by passing a current through the sample, or by radiative heating from a heating element. The sample temperature dictates the average energy of atoms at the sample surface, and therefore the average mobility. Samples are usually rotated during growth in order to ensure uniform coverage (and therefore composition for alloys).

2.2.3 Crystal surfaces and surface reconstructions

A semiconductor crystal is typically treated as an ideal crystal, i.e. one that is infinite in three dimensions. However when using an epitaxial technique such as MBE, the surface of the crystal must be considered. A crystal surface represents a termination of the lattice in a particular dimension, and so the atoms present on the surface will no longer have their bonding requirements satisfied. To minimise the energy of the surface, the surface atoms can move uniformly in a certain direction (usually closer to the bulk). This process is termed relaxation. Often, however, the atoms will adopt an entirely different structure from that of the bulk, in a process termed reconstruction. The study of surface reconstructions of semiconductor surfaces has been of great interest to physicists, chemists and materials scientists over the past 50 years. MBE has provided a means to grow surfaces under controlled conditions so that many different reconstructions can be observed.

The standard notation used to describe surface reconstructions of III-V semiconductors is Wood's notation [5]. This takes the form

$$X(hkl)\ n \times m\ R\varphi$$

where X is the chemical formula of the material and h,k,l are the Miller indices of the surface. The surface unit cell is n times greater that the bulk unit cell in the x direction and m times the unit cell in the y direction. The unit cell may also be rotated by an angle φ compared to the bulk unit cell (denoted by $R\varphi$).

Surface reconstructions observed during growth are referred to as dynamic reconstructions, while those observed when no growth is taking place are termed static reconstructions. The reconstruction adopted by a surface depends on the surface temperature and also the composition of the surface, which in MBE is determined by the material fluxes. Varying both the sample temperature and the fluxes allows a phase diagram of surface structures to be built up. An example of such a phase diagram for the growth of GaAs is shown in [6].

2.2.4 Growth modes

There are two growth modes in homoepitaxy. Assuming the surface possesses a series of terraces, an adatom on the surface can either be incorporated at a step edge or on the terrace surface. The growth mode adopted depends on the relationship between the diffusion length of an adatom, λ, and the average terrace width, l. At low temperatures, the diffusion length is low and adatoms are unlikely to reach step edges. Instead they nucleate on the terrace itself, forming two-dimensional 'islands'. At higher temperatures, adatoms are able to diffuse to step edges and growth occurs by the advancement of the edges, so-called 'step flow'.

For heteroepitaxy, there are three growth modes. In the Frank-van der Merwe (F-M) mode, growth occurs a layer at a time - it is 'two-dimensional'. In the Volmer-Weber (V-W) mode, three-dimensional islands form on the substrate. Stranski-Krastanov (S-K) growth is an intermediate mode, where growth initially occurs in a layer-by-layer fashion then undergoes a transition to 3D island growth above a critical thickness, h.

The growth mode adopted by a system where a material *A* is being deposited on a material *B* is determined by the inequality

$$\gamma_A + \gamma_{AB} = \gamma_A + \gamma_{AB}^{\epsilon} + \gamma_{AB}^{0} < \gamma_B \tag{2.1}$$

where γ_A and γ_B are the surface free energies of *A* and *B* and γ_{AB} is the interface free energy. This is composed of two parts: the strain energy γ_{AB}^{ϵ} which increases with the thickness of the epitaxial layer and the zero strain energy γ_{AB}^{0} which depends on the chemical interaction between A and B [7].

2.2.5 Surfactants

The heteroepitaxial growth of a semiconductor material on a substrate can be viewed simply from a thermodynamic perspective by considering the different surface energies of the two materials. Copel et al. [8] showed simply that this leads to problems for obtaining layer-by-layer growth - if material *A* grows on *B* in a layer-by-layer mode, then *B* will grow on *A* in a V-W or S-K mode, and vice-versa. They suggested using a third species, *C*, which will surface segregate and lower the surface energies of *A* and *B*, inhibiting island formation. Such a species is referred to as a surfactant. They demonstrated this effect for the growth of Ge on Si using As as a surfactant. Though this increases layer quality, some of the As will incorporate into the film and act as an n-type dopant, leading to undesirably high background doping levels.

Grandjean et al. [9-11] were the first to investigate this effect for III-V material systems, looking at the growth of InAs on GaAs, which typically occurs via the S-K growth mode. In this case the group VI element tellurium (Te) was used as a surfactant. They showed that use of Te prolongs layer-by-layer growth and increases the critical thickness for which strain relaxation occurs. As with using As for group IV semiconductor growth, Te will act as an n-type dopant if it is incorporated. It has been pointed out by Massies [12] that when a surfactant is used to prevent a S-K transition, it is assumed to reduce the surface diffusion length, however when a surfactant is used to improve the quality of an epi-layer grown in the 2D layer-by-layer mode, it is increasing the surface diffusion length.

Bi was then used as a surfactant for the growth of InGaAs on GaAs by Pillai et al. [13], who reported reduced interface roughness and improved PL intensity in MQW structures. Following this, other groups have used Bi for improving the growth of (In)GaAsN [14, 15] and more recently BGaAs [16] and InAs quantum dots [17]. This use of Bi as a surfactant was a precursor to its role as an alloying element in III-V-Bi compounds.

2.2.6 Reflective high energy electron diffraction

There are several techniques used to monitor the growth process *in situ*, the most common of which is reflection high energy electron diffraction (RHEED). In this technique, electrons are supplied by an electron gun operating at voltages between 5 and 15 kV. The electrons are incident on the sample at very low angles (< 5°), so that they glance off the surface. As the chamber is under high vacuum, the electrons will have an uninterrupted path to the sample. After interacting with the surface, the electrons hit a phosphorescent screen, producing a pattern called a diffraction pattern.

RHEED can provide lots of important information about a sample surface. The diffraction pattern gives information about how the surface atoms are organised, as the periodicity of the surface reconstruction will determine the periodicity of the diffraction pattern. For instance, under conventional growth conditions a GaAs surface exhibits a (2×4) reconstruction. The RHEED pattern from this surface has twofold periodicity along the [110] azimuth, and fourfold periodicity along the [-110] azimuth [18]. Since the transitions between reconstructions occur at specific temperatures and flux ratios, they can be used as calibration points.

In addition, during growth, the intensity of the spots in the diffraction pattern fluctuates periodically. The period of the oscillations has been shown to correspond exactly to the growth of a single Ga-As layer [19, 20], and can therefore be used to calculate the growth rate. Typical intensity oscillations observed during growth of a GaAs buffer layer are shown in Figure 2.1. The time between many peaks is measured and divided by the number of peaks in order to give an average value for a single oscillation.

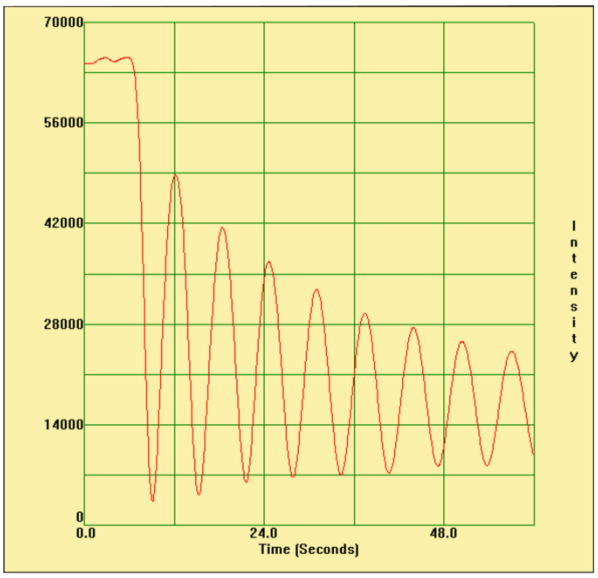

Figure 2.1: RHEED oscillations during growth of a GaAs buffer layer.

2.3 Growth using the MBE-STM system

All samples in this work were grown using an Omicron molecular beam epitaxy-scanning tunnelling microscopy (MBE-STM) system, unless otherwise noted. The system consists of an MBE chamber which is connected to a second, smaller MBE chamber containing a scanning tunnelling microscope. This allows STM measurements to be performed *in situ* while growth is taking place. However, only the conventional MBE chamber was used for growth of these samples. The system has a few differences from conventional MBE systems, which are outlined here.

2.3.1 Main growth chamber

The main MBE chamber is fitted with effusion cells for Al, Ga, In and Bi, as well as a Be/Si dual dopant cell. This contains two crucibles, one for each dopant. Initially (for the growth of these samples) As_4 was produced by evaporation of polycrystalline As in a standard effusion cell. An As cracker was added to the machine in August 2011, which allows either As_2 or As_4 to be used. A pyrolytic graphite (PG) track encapsulated in pyrolytic boron nitride (PBN) was used as a heating element. A movable ion gauge was used to measure the source fluxes.

The vacuum in the main MBE chamber is maintained by a turbo pump, an ion pump and a cooling shroud. This is cooled by liquid nitrogen which is supplied from a pressurized dewar. The background pressure in the chamber is typically around 10^{-9} mbar when the cells are at their standby temperatures.

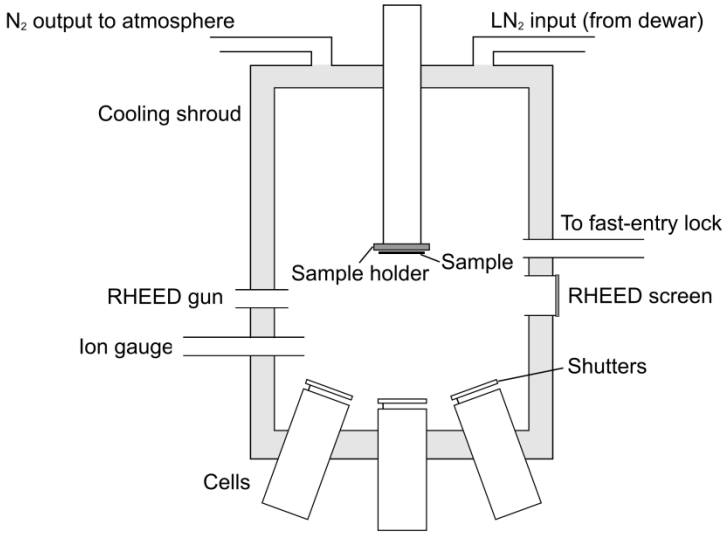

Figure 2.2: Diagram showing the main growth chamber of the MBE-STM system.

2.3.2 RHEED setup

Growth rates and surface reconstructions were determined using a RHEED gun operating at 15-18 kV. The intensity of the RHEED pattern was monitored using a camera. The signal from the camera was passed to a computer running software allowing the measurement of intensity over time. The growth rate was determined by averaging over several (typically at least 10) oscillations.

2.3.3 Sample details

The MBE-STM uses small samples measuring 11 mm × 3.5 mm. (A new sample plate was designed by F. Bastiman in June 2011 in order to accommodate larger samples measuring 11.4 mm × 11.8 mm). Whilst the sample rotation can be adjusted manually over a limited range, there is no facility for continuous rotation during growth. This has implications for material uniformity, although this is partially offset by the small sample size used.

Initially the sample is loaded into a fast-entry lock (FEL) chamber, which is separated from the main growth chamber by a gate valve. The FEL is pumped down by a turbo pump to a pressure of around 10^{-9} mbar before being transferred into the main growth chamber. Conventional MBE setups often have the facility to load multiple samples into the machine at once, which makes switching to a new sample easier. However in our system only one sample can be present in the machine at any one time, which limits throughput.

Samples were cleaned using isopropanol (IPA) before being loaded into the reactor. Upon loading into the main growth chamber, the sample is outgassed at 400 °C for 30 minutes to remove impurities such as water vapour from the sample surface. GaAs has a native surface oxide layer which must be removed before growth begins. This is achieved by heating at 580 °C for a further 30 minutes. The details of the growth of the samples will be covered in the next chapter.

2.4 Device fabrication

After growth, device structures must be processed in order to carry out device characterisation. A process flow is used consisting of several steps. The process outlined below is standard for GaAs p-i-n diode structures (where the substrate is n-type).

First, the sample is cleaned using n-butyl acetate, acetone, and isopropanol in turn. The sample is immersed in a beaker containing the solvent and heated on a hot plate for approximately 30 seconds (this heating step is omitted when using acetone). The solvent is wiped from the surface using a cotton bud and the sample is blown dry using a nitrogen gun. After the final cleaning step, the sample surface is inspected using a microscope and if necessary the cleaning process is repeated. The surface needs to be clean as possible in order to ensure a good contact between the metal contacts and the semiconductor.

The front and back contacts are deposited onto the sample using an evaporator. A schematic diagram of an evaporator is shown in Figure 2.3. The evaporation is carried out under high vacuum conditions, so that the metal atoms have an uninterrupted path to the sample and also so that no oxidation can take place. For the back (n-type) contacts, an InGeAu alloy is used. 20 nm of In/Ge are deposited followed by 200 nm of Au. The metals are placed in coils/boats which are suspended above the sample. The chamber is then evacuated, first using a rotary pump, then a diffusion pump, in order to reach a vacuum of around 5×10^{-6} mbar. Once this vacuum is achieved, a current is passed through the coil/boat containing the metal to be evaporated. When a high enough current is reached, the atoms will begin to evaporate from the metal on to the sample. The evaporation rate is monitored using a crystal monitor. Once all the metals have been evaporated, the coils/boats are allowed to cool and the evaporator is returned to atmospheric pressure.

Usually, deposition of metal on to a semiconductor will form a Schottky (rectifying) contact. In order to ensure that ohmic contacts are obtained, annealing may be necessary. To check whether the back contact is ohmic, a small piece of metal wire can be used as a mask during evaporation, which will leave a section of the sample uncovered by the evaporated metal. Probes can be connected to the two coated areas of the semiconductor, to see whether an ohmic I-V trace is obtained. The sample can then be annealed and the contacts re-tested. Annealing allows the contact metal to diffuse into the semiconductor, forming a highly n-doped surface layer which aids formation of an Ohmic contact [21, 22].

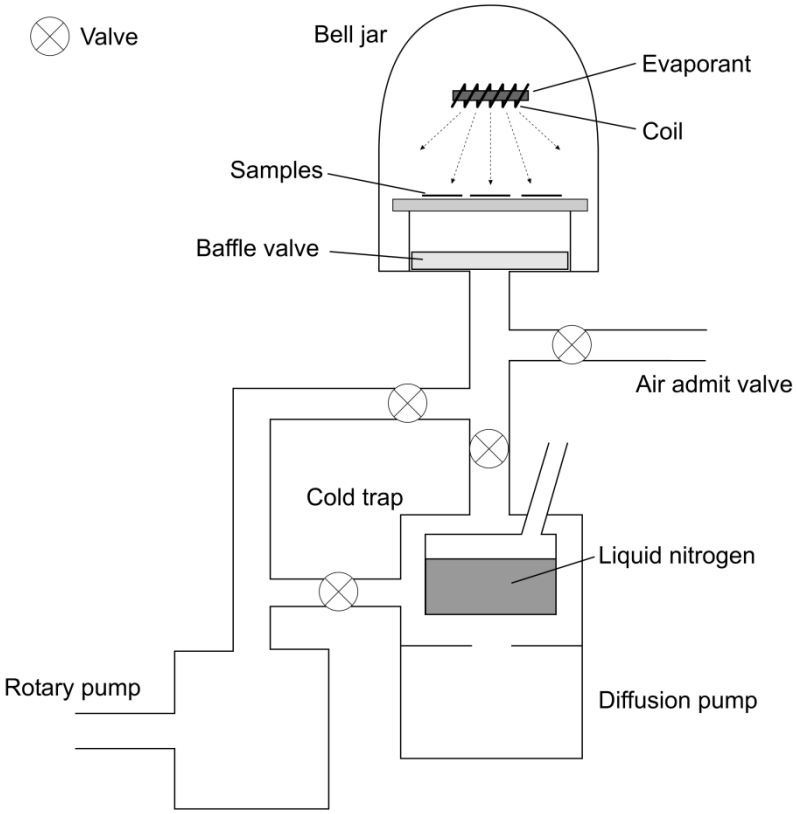

Figure 2.3: Diagram showing an evaporator and associated vacuum pumps.

The InGeAu contacts are annealed using a furnace, which is pre-heated to a temperature of around 450 °C. The sample is loaded into a quartz boat and is left for 5 minutes under a nitrogen flow to flush out air in order to prevent oxidation of the contacts. The boat is then moved into the centre of the furnace and the temperature of the sample is monitored via a thermocouple. Once the temperature reading is within 10 °C of the desired temperature, the boat is removed from the furnace. When the sample cools to below 100 °C, it can be removed from the chamber and cleaned.

The next step is to form a pattern for the top contacts. This is achieved using ultraviolet (UV) photolithography. First, the sample is stuck to a glass slide using wax, and a photoresist (BPRS 100) is spin-coated on to the top surface of the sample. A spin speed of 4000 rpm for 30 seconds is used, which gives a resist thickness between 600 and 900 nm. The sample is then baked at 100 °C for 1 minute to harden the resist. The sample is then selectively exposed to UV light using a Karl-Suss mask aligner. This contains a microscope which is used to align the sample with the mask pattern. The sample must be brought into close contact with the mask to

ensure accurate reproduction of the mask pattern, and the exposure time must be adjusted to give the optimum exposure.

After exposure, the sample is held in the developer solution for 1 minute, and then rinsed with de-ionized water. Areas of the photoresist which were exposed to the UV light are photo-oxidised and are removed. The sample surface is now covered by photoresist apart from the areas which are to be used for contacts. The pattern is checked under a microscope. If the sample has been under/overexposed, the photoresist can be removed using acetone and the process can be repeated. Diagrams of the sample at various stages of the photolithography process are shown in Figure 2.4.

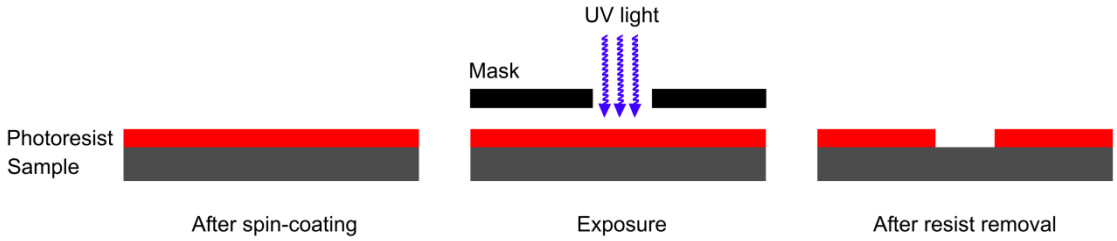

Figure 2.4: Diagrams illustrating the photolithography process.

Once the process is complete, the sample is ready for the second evaporation step. This step is the same as the first evaporation step, except that a different combination of metals is required. In order to form a contact to p-type GaAs, a AuZnAu alloy is used. 5 nm of Au is deposited followed by 10 nm of Zn and 200 nm of Au. The Zn forms a p-doped surface layer in the same way as Ge for n-type GaAs [23]. Once this step is complete, the photoresist can be removed using acetone. This also removes the metal on top of the resist, leaving only the contact areas covered with metal. Again, the contacts are checked to see if they are ohmic by probing two neighbouring top contacts, and annealed if necessary at a temperature of around 360 °C.

The devices must now be isolated from each other. This is achieved by a combination of photolithography and etching. The samples are cleaned in a similar manner to before, only this time a cotton bud is not used as this would damage the contacts. The samples are again coated with photoresist, but this time a different mask is used which covers the areas that will form devices, and the photoresist around the devices is removed. The mask pattern contains alignment markings which help align the mask pattern with the contact pattern. After exposure and developing, the samples can now be etched, with the areas between the devices being removed by the etchant.

Before etching, a height profile of the surface is measured using a Dektak surface profiler. This is to measure the depth of the photoresist, which is necessary to work out the etch depth. The samples are etched down to form mesas using hydrogen bromide (HBr), acetic acid (CH_3COOH) and potassium dichromate ($K_2Cr_2O_7$) mixed in a 1:1:1 ratio. This etchant has been shown to produce smooth etch surfaces for GaAs (001) [24]. It is also an anisotropic etchant which means undercutting of the metal contacts is negligible. Typical surface profiles before and after etching are shown in Figure 2.5. It is assumed that the presence of the Bi atoms does not have a significant effect on the etching process since the concentration is relatively low.

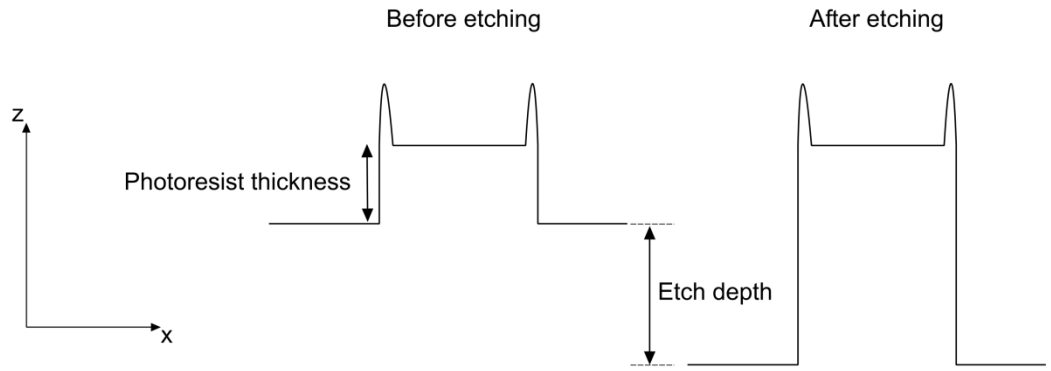

Figure 2.5: Height profiles for a sample before and after etching.

For p-i-n structures, it is necessary to etch through the p-type and undoped layers into the n-type layer. The sample is immersed in the solution for a set period of time, depending on the sample structure. After this time the height profile is re-measured in order to determine how much of the sample has been etched away. From this an estimate of the etch rate can be obtained, although this will decrease over time. Once the sample has been etched to the desired depth, the photoresist covering the devices can be removed using acetone and the devices are ready for characterisation. A schematic diagram showing a processed p-i-n mesa structure is shown in Figure 2.6.

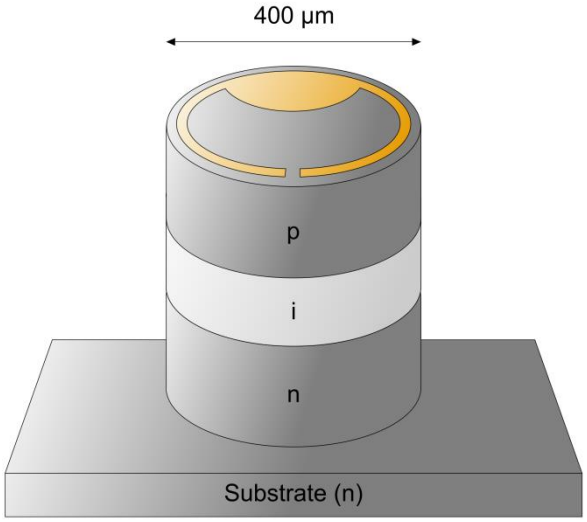

Figure 2.6: Diagram of a processed p-i-n mesa structure with a radius of 200 µm.

For certain characterisation techniques e.g. electroluminescence, it is desirable to use packaged samples. This involves cleaving a small piece of the sample and securing it to a TO5 header using conducting paste. The top contacts are then connected to the pins on the header using a ball wire bonder.

2.5 References

[1] J. R. Arthur, "Interaction of Ga and As_2 Molecular Beams with GaAs Surfaces," *J. Appl. Phys.*, vol. 39, pp. 4032-4034, 1968.

[2] L. L. Chang, L. Esaki, W. E. Howard, and R. Ludeke, "The Growth of a GaAs-GaAlAs Superlattice," *Journal of Vacuum Science and Technology*, vol. 10, pp. 11-16, 1973.

[3] R. Dingle, W. Wiegmann, and C. H. Henry, "Quantum States of Confined Carriers in Very Thin $Al_xGa_{1-x}As$-GaAs-$Al_xGa_{1-x}As$ Heterostructures," *Phys. Rev. Lett.*, vol. 33, pp. 827-830, 1974.

[4] J. R. Arthur, "Molecular beam epitaxy," *Surface Science*, vol. 500, pp. 189-217, 2002.

[5] E. A. Wood, "Vocabulary of Surface Crystallography," *J. Appl. Phys.*, vol. 35, pp. 1306-1312, 1964.

[6] L. Däweritz and R. Hey, "Reconstruction and defect structure of vicinal GaAs(001) and $Al_xGa_{1-x}As$(001) surfaces during MBE growth," *Surface Science*, vol. 236, pp. 15-22, 1990.

[7] E. Bauer and J. H. van der Merwe, "Structure and growth of crystalline superlattices: From monolayer to superlattice," *Phys. Rev. B,* vol. 33, p. 3657, 1986.

[8] M. Copel, M. C. Reuter, E. Kaxiras, and R. M. Tromp, "Surfactants in epitaxial growth," *Phys. Rev. Lett.,* vol. 63, p. 632, 1989.

[9] N. Grandjean, J. Massies, and V. H. Etgens, "Delayed relaxation by surfactant action in highly strained III-V semiconductor epitaxial layers," *Phys. Rev. Lett.,* vol. 69, pp. 796-799, 1992.

[10] J. Massies, N. Grandjean, and V. H. Etgens, "Surfactant mediated epitaxial growth of $In_xGa_{1-x}As$ on GaAs (001)," *Appl. Phys. Lett.,* vol. 61, pp. 99-101, 1992.

[11] N. Grandjean, J. Massies, C. Delamarre, L. P. Wang, A. Dubon, and J. Y. Laval, "Improvement of the growth of $In_xGa_{1-x}As$ on GaAs (001) using Te as surfactant," *Appl. Phys. Lett.,* vol. 63, pp. 66-68, 1993.

[12] J. Massies and N. Grandjean, "Surfactant effect on the surface diffusion length in epitaxial growth," *Phys. Rev. B,* vol. 48, pp. 8502-8505, 1993.

[13] M. R. Pillai, S. Kim, S. T. Ho, and S. A. Barnett, "Growth of $In_xGa_{1-x}As$/GaAs heterostructures using Bi as a surfactant," *J. Vac. Sci. Technol., B,* vol. 18, pp. 1232-1236, 2000.

[14] S. Tixier, M. Adamcyk, E. C. Young, J. H. Schmid, and T. Tiedje, "Surfactant enhanced growth of GaNAs and InGaNAs using bismuth," *J. Cryst. Growth,* vol. 251, pp. 449-454, 2003.

[15] E. C. Young, S. Tixier, and T. Tiedje, "Bismuth surfactant growth of the dilute nitride GaN_xAs_{1-x}," *J. Cryst. Growth,* vol. 279, pp. 316-320, 2005.

[16] A. J. Ptak, D. A. Beaton, and A. Mascarenhas, "Growth of BGaAs by molecular-beam epitaxy and the effects of a bismuth surfactant," *J. Cryst. Growth,* vol. 351, pp. 122-125, 2012.

[17] D. Fan, Z. Zeng, V. G. Dorogan, Y. Hirono, C. Li, Y. I. Mazur, S. Yu, S. R. Johnson, Z. M. Wang, and G. J. Salamo, "Bismuth surfactant mediated growth of InAs quantum dots by molecular beam epitaxy," *Journal of Materials Science: Materials in Electronics,* vol. 24, pp. 1635-1639, 2013/05/01 2013.

[18] M. Dabrowska-Szata, "Analysis of RHEED pattern from semiconductor surfaces," *Mater. Chem. Phys.,* vol. 81, pp. 257-259, 2003.

[19] J. H. Neave, B. A. Joyce, P. J. Dobson, and N. Norton, "Dynamics of film growth of GaAs by MBE from Rheed observations," *Applied Physics A: Materials Science & Processing,* vol. 31, pp. 1-8, 1983.

[20] J. J. Harris, B. A. Joyce, and P. J. Dobson, "Oscillations in the surface structure of Sn-doped GaAs during growth by MBE," *Surface Science,* vol. 103, pp. L90-L96, 1981.

[21] N. Braslau, "Alloyed ohmic contacts to GaAs," *Journal of Vacuum Science and Technology*, vol. 19, pp. 803-807, 1981.

[22] A. G. Baca, F. Ren, J. C. Zolper, R. D. Briggs, and S. J. Pearton, "A survey of ohmic contacts to III-V compound semiconductors," *Thin Solid Films*, vol. 308-309, pp. 599-606, 1997.

[23] T. C. Shen, G. B. Gao, and H. Morkoc, "Recent developments in ohmic contacts for III–V compound semiconductors," *J. Vac. Sci. Technol., B*, vol. 10, pp. 2113-2132, 1992.

[24] S. Adachi and K. Oe, "Chemical Etching Characteristics of (001) GaAs," *J. Electrochem. Soc.*, vol. 130, pp. 2427-2435, 1983.

Chapter 3: Characterisation Techniques

3.1 Introduction

In this section, an overview of the various characterisation techniques used in this work is given. The techniques are organized according to the type of information that is obtained, i.e. structural, optical or electrical.

3.2 Structural characterisation

3.2.1 X-ray diffraction

X-ray diffraction (XRD) is a non-destructive structural characterisation technique which can give information about sample properties such as layer thickness, lattice mismatch and alloy composition [1]. It is performed on samples before processing, as the whole structure needs to be measured and this is obviously affected by the etching process.

In a crystal there are planes of atoms which are a fixed distance apart. When an X-ray beam is incident on a crystal it can be diffracted by these planes. The diffracted beams will interfere with each other, and constructive interference occurs when the Bragg equation is satisfied:

$$n\lambda = 2dsin\theta \tag{3.1}$$

where n is an integer, λ is the X-ray wavelength, d is the distance between the adjacent crystal planes and θ is the angle between the incident ray and the crystal planes. Therefore for a fixed wavelength, an XRD spectrum of intensity versus diffraction angle contains peaks which correspond to the interplanar spacings of the materials within the sample.

A Bede D1 HR-XRD system was used to perform XRD measurements. A copper X-ray source operating at 50 kV was used, which produces characteristic emission wavelengths $K_{\alpha 1}$, $K_{\alpha 2}$ and K_{β}. In order to obtain a monochromatic X-ray beam, a silicon crystal channel cut was used, which removes the K_{β} wavelength. Of the K_{α} lines, the $K_{\alpha 1}$ line is typically used for measurements as this is the more intense of the two. The $K_{\alpha 2}$ line was cut out using a slit placed before the sample.

During a scan, the source remains fixed and both the sample and the detector are rotated. The angle of the source beam with the sample is referred to as omega, ω, and the angle of the detector with the sample is 2theta, 2θ. The interplanar spacing is determined from the peak position using equation (3.1). For a (004) reflection, the lattice parameter is four times this value.

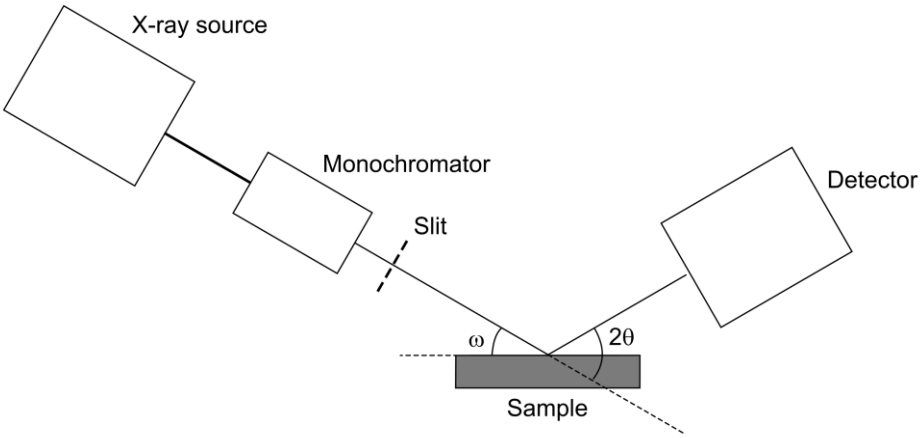

Figure 3.1: Diagram of a typical XRD setup.

One important application of XRD in the field of semiconductors is the determination of alloy composition. Once the lattice parameter of the material is known, the composition can be determined using Vegard's law, which assumes that the lattice constant has a linear dependence on the alloy composition. For $GaAs_{1-x}Bi_x$:

$$a_{GaAsBi} = x(a_{GaBi}) + (1 - x)(a_{GaAs}) \tag{3.2}$$

x is the GaBi fraction, which takes values between 0 and 1. Thus estimation of the lattice constant requires knowledge of the lattice constants of both components. The lattice constant for GaAs is 5.653 Å [2]. Since GaBi has not been synthesised, its lattice constant is obtained from theory. Janotti et al. found a value of 6.324 Å for a_{GaBi} [3], which is used in this work.

3.2.2 SIMS

Secondary ion mass spectrometry (SIMS) is a useful tool for determining concentrations of elements within a semiconductor structure. In the case of the samples in this work it is used for looking at dopants (Si and Be), as well as Bi in GaAsBi layers. It can be performed on samples before or after processing.

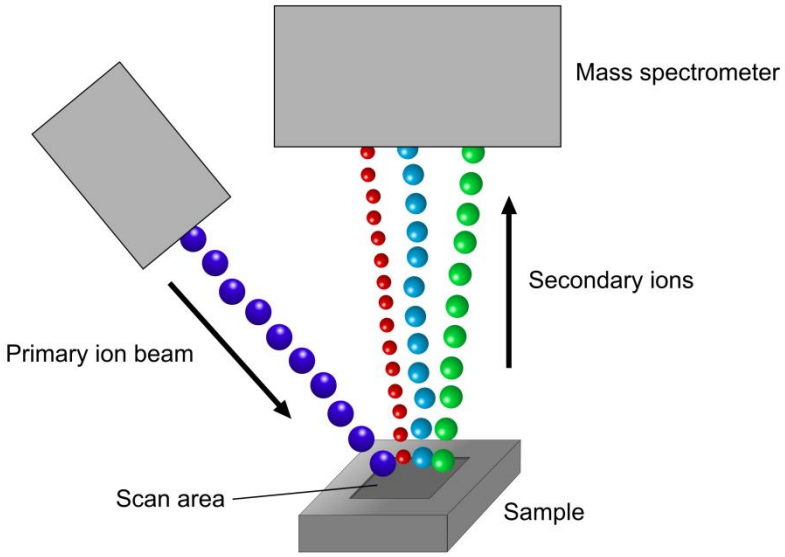

Figure 3.2: Diagram illustrating the SIMS process.

Figure 3.2 illustrates the SIMS process. A primary beam of ions is directed at the sample under vacuum. The secondary ions ejected from the surface are collected and analysed by a mass spectrometer. As the process continues, the sample is gradually eroded, forming a crater. At the end of the measurement the depth of the crater can be measured using a surface profiler. If it is assumed that the sputtering rate remains constant throughout the measurement, the erosion depth can be assumed to be proportional to time, and can be expressed by the equation [4]

$$d(t) = \frac{d_{tot}}{t_{tot}} t \tag{3.3}$$

where d_{tot} and t_{tot} are the depth and time at the end of the measurement.

The signal detected by the mass spectrometer is proportional to the concentration of the species under study. Using equation (3.3) the concentration at a given time can be related to the concentration at a given thickness, and thus a graph of concentration versus thickness can be obtained.

In order to quantify the signal from the mass spectrometer, a calibration sample with a known doping concentration is necessary. Samples doped with Be and Si were used to calibrate the doping concentrations, however we do not have a Bi calibration sample at present. Thus the Bi concentration could not be determined from the SIMS measurements, although it is still possible to measure the thicknesses of the GaAsBi layers.

3.3 Optical characterisation

3.3.1 Electroluminescence

Luminescence measurements are non-destructive optical analysis techniques that are used extensively for characterisation of III-V compounds. They are mainly used for direct band gap materials which give strong luminescence. In these methods, electron-hole pairs recombine radiatively within the material, emitting light, and the intensity of the luminescence is measured as a function of the emission wavelength. There are several ways of creating electron-hole pairs; the electroluminescence method used in this work utilises injection from an external circuit.

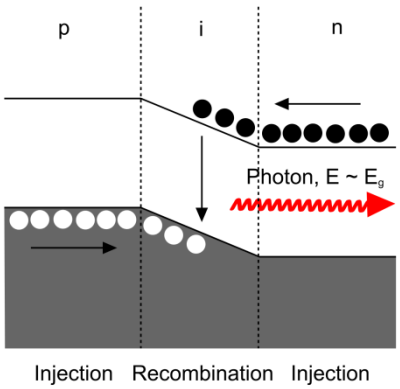

Figure 3.3: Diagram illustrating the electroluminescence process.

This process is illustrated in Figure 3.3. In electroluminescence, electrons and holes are injected into a p-n/p-i-n junction under forward bias and recombination will occur in the depleted region of the structure. For a conventional semiconductor at room temperature, the emitted photons have energies close to the band gap energy and a luminescence spectrum will show a peak at the wavelength corresponding to this energy.

For electroluminescence measurements, the packaged sample was mounted in a cryostat and connected to a Keithley 236 source-measure unit, which was set to current-source mode. The luminescence from the sample was collected and focused using a Cassegrain lens. After passing through the lens, the luminescence was chopped by a mechanical chopper operating at 180 Hz, which was connected to a lock-in amplifier. This frequency was chosen in order to avoid interference with the mains frequency of 50 Hz. A high-pass filter was placed in front of the entrance slits of the monochromator in order to cut out any short-wavelength light emitted from the sample. The monochromator contains three different diffraction gratings to allow coverage of different wavelength ranges. The grooves/mm values of the gratings are 1200, 900 and 600, which correspond to blaze wavelengths of 330 nm, 850 nm and 1500 nm respectively. The 850 nm blaze wavelength grating was used for all measurements as it has a good response over the range 850 - 1400 nm, which is most suitable for the GaAsBi samples in this work.

After passing through the monochromator the light was detected by a liquid-nitrogen cooled germanium detector. The signal from the detector was passed to the PC via the lock-in amplifier and a SpectraMax control unit. Using the signal from the chopper as a reference allows the lock-in amplifier to isolate the PL signal from any background noise. Neutral density filters were used to attenuate the sample luminescence, if required.

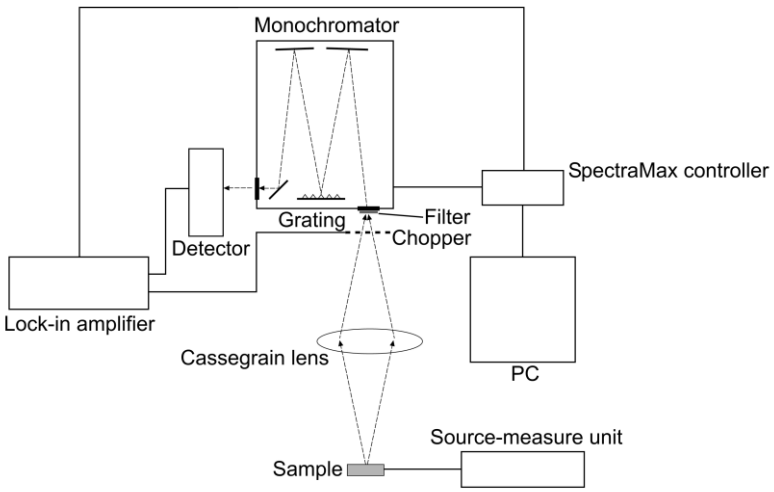

Figure 3.4: Diagram of setup for EL measurements.

In order to perform measurements at low temperatures, the cryostat is sealed and held under vacuum by a rotary pump. The cryostat was cooled by a helium compressor and can reach temperatures as low as 10 K. To achieve temperatures between 10 K and room temperature, the cryostat also contains a heater which is connected to a temperature controller.

3.3.2 Photocurrent

In electroluminescence a diode structure emits light when current is injected. For detection, the inverse process occurs: light is incident on the device and a photocurrent is generated. This process is illustrated in Figure 3.5.

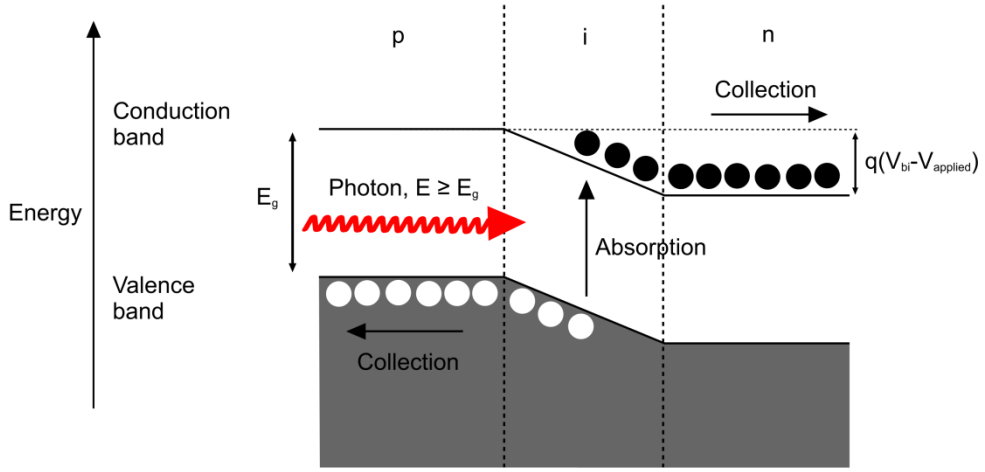

Figure 3.5: Diagram illustrating absorption and detection of light in a p-i-n diode structure.

Once absorption has occurred, the electron-hole pairs must be separated. This is accomplished by the built-in electric field that is present across the i-region. While solar cells are operated in forward bias, photodiodes/detectors are commonly operated in reverse bias. In this case the potential barrier between the n and p regions increases and the electric field across the i-region is increased, aiding carrier collection. If absorption occurs in the i-region, this can happen directly, otherwise carriers must diffuse from the p or n regions into the i-region before charge separation can occur. If the photon flux incident on the sample is constant, the system reaches a steady state and a constant current value can be measured, which is proportional to the photon flux.

Two sets of photocurrent measurements were undertaken. Photocurrent measurements at a fixed wavelength of 1064 nm were taken using a continuous wave laser, and the photoresponse over a range of wavelengths was measured using a white light source and a monochromator with a phase-sensitive detection system. The two setups are illustrated in Figure 3.6.

For the laser measurements, the laser power incident on the device was measured using a commercial InGaAs surface-mounted photodiode. The photocurrent of the samples as a function of bias was obtained by performing an I-V sweep in the dark and with the laser

illuminating the device, then subtracting the dark current from the current under illumination. This is a reasonable method since the photocurrent generated by the laser is much greater than the dark current.

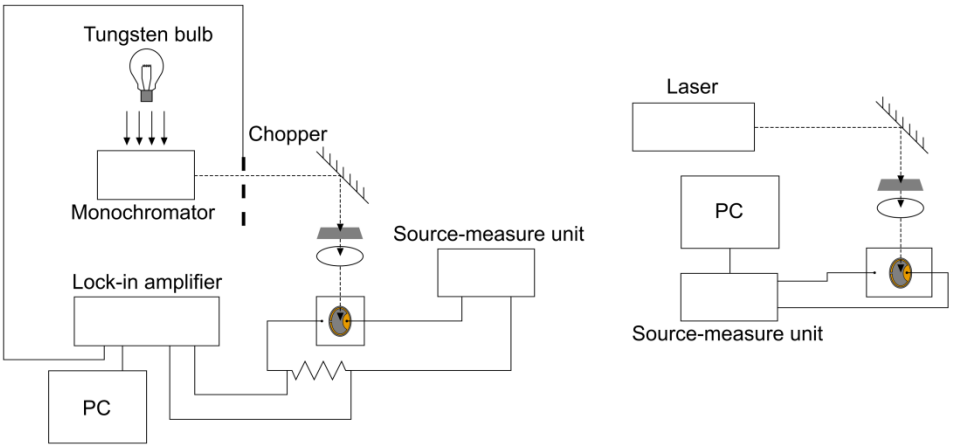

Figure 3.6: Diagrams showing two photocurrent setups with a white light source (left) and a laser light source (right).

For the photoresponse measurements, white light from a tungsten bulb was dispersed using a monochromator. The monochromator contains a diffraction grating with a groove density of 600 grooves/mm and a blaze wavelength of 1000 nm. The light was focussed on to the device using an objective lens. The device was biased using a Keithley 236 source-measure unit. In this case, the photocurrent is lower than the dark current, and so the photocurrent signal needs to be extracted from the overall current. This is achieved by monitoring the voltage across a resistor in series with the device using a lock-in amplifier synchronised with a mechanical chopper. The voltage signal obtained was sent to the PC via a Spectracq control unit.

A commercial germanium photodiode with a known photoresponse was used to obtain the response of the system (white light source emission and diffraction grating response) using equation (3.4). This response was used to correct the obtained data.

$$System\ response = \frac{Measured\ photoresponse}{Actual\ photoresponse} \tag{3.4}$$

3.4 Electrical characterisation

3.4.1 Current-voltage (I-V)

Room-temperature I-V measurements were performed on unpackaged devices. The devices were observed using a microscope while probing to ensure that a good contact was obtained. The devices were connected to a picoammeter, which was used to source voltage and measure current. A computer was used to record the current values and control the picoammeter. A curve tracer was also used to make rough I-V measurements.

Low temperature I-V measurements were performed using a Janis probe station. The sample was placed in a vacuum chamber which was cooled by liquid nitrogen, thus the lowest achievable temperature is ~77 K. To vary the temperature, a heating stage connected to a temperature controller was used. The liquid nitrogen flow rate was adjusted to suit each temperature.

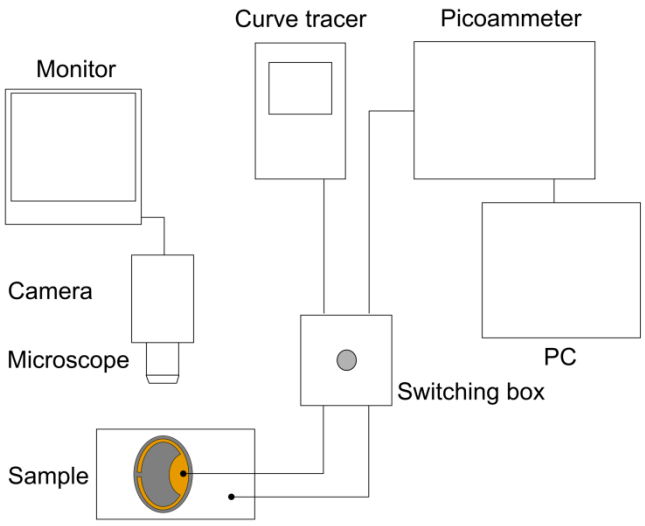

Figure 3.7: Diagram showing setup for I-V measurements.

3.4.2 Capacitance-voltage (C-V)

Capacitance-voltage is a technique that is commonly used to obtain information about the doping in a device structure. Such doping could be intentional (e.g. the doping in a p-n junction) or unintentional (e.g. where background impurities are present, such as carbon or oxygen). Capacitance is defined as:

$$C = \frac{dQ}{dV} \tag{3.5}$$

In the C-V technique, a DC voltage (usually negative) is applied to the device, which will deplete a certain amount of material. On top of this, a small AC voltage signal is applied. As this voltage varies (*dV*), the number of ionized charge carriers will also vary (*dQ*), allowing the capacitance to be calculated. Assuming the dopants are fully ionized, this is equivalent to the doping concentration.

Room temperature C-V characteristics of the unpackaged devices were measured using a similar setup to the I-V measurements, except with the sample connected to a LCR meter instead of a picoammeter. To ensure that only the capacitance of the device is measured, the sample was connected directly to the LCR meter without using the switching box. The stray capacitance of the leads was taken into account by zeroing the LCR meter before each measurement.

3.5 References

[1] D.K. Bowen and B.K. Tanner, *High Resolution X-Ray Diffractometry And Topography*: Taylor & Francis, 1998.

[2] K. A. Jones, *Introduction to Optical Electronics*: John Wiley & Sons, 1987.

[3] A. Janotti, S. Wei, and S. B. Zhang, "Theoretical study of the effects of isovalent coalloying of Bi and N in GaAs," *Phys. Rev. B*, vol. 65, p. 115203, 2002.

[4] P. C. Zalm, "Ultra shallow doping profiling with SIMS," *Reports on Progress in Physics*, vol. 58, p. 1321, 1995.

Chapter 4: Growth and Structural Characterisation

4.1 Introduction

There are two issues to be considered when growing GaAsBi. First, there is a miscibility gap between GaAs and GaBi, which necessitates the use of low growth temperatures in order to incorporate Bi into the lattice. In addition to this problem, Bi atoms tend to migrate to the surface of a growing film due to their large size [1]. This effect has led to bismuth being used as a surfactant during epitaxial growth [2-4], as mentioned in chapter 2.

4.1.1 Early growth of III-V-Bi compounds

Though this work focusses purely on the incorporation of Bi into GaAs, Bi has been used a constituent of other III-V materials for over 40 years. In 1971, Joukoff proposed incorporating Bi into InSb in order to reduce the band gap [5]. In this work InSbBi was prepared by the Czochralski method. Growth of InSbBi by MBE has also been reported [6], however the Bi incorporation is limited by the fact that InBi has a tetragonal crystal structure as opposed to the zinc-blende structure of InSb [7].

4.1.2 MBE growth of GaAsBi

Although most reports of GaAsBi growth in the literature use MBE, GaAsBi was first grown by MOVPE in 1998 [8]. In this work, a Bi composition of around 2% was achieved. This work was motivated by the need for a semiconductor whose band gap is less sensitive to temperature than conventional semiconductors such as InP.

Growth of GaAsBi by MBE was first reported by Tixier et al. in 2003 [1]. They found that low arsenic to gallium flux ratios, close to the stoichiometric value, were required in order for the bismuth atoms to be incorporated, as well as a growth temperature of 380 °C. Bi contents of up to 3.1% were achieved.

In this work and other early papers [9, 10], the bismuth contents of the GaAsBi samples were measured by Rutherford backscattering spectroscopy (RBS). XRD was not used since the lattice constant of GaBi is unknown. An estimate of this value was calculated in [1] by extrapolating from the measured lattice parameters of the GaAsBi layers. In most reports of

MBE growth, As_2 rather than As_4 is used as an arsenic source, and low growth temperatures in the range 270 - 400 °C are commonly used. It has been shown that using As_4 instead of As_2 negates the requirement for a near-stoichiometric flux ratio [11], however when the desorption of excess As during use of As_4 is taken into account, the maximum achievable [Bi] was found to be independent of the As species used [12].

4.1.3 Effect of growth conditions on material quality

The flux ratios typically used for GaAsBi growth can lead to the formation of metallic droplets on the epilayer surface [13]. Using low As:Ga flux ratios can allow Ga droplets to form, while accumulation of excess Bi may lead to the formation of Bi droplets. Ga-Bi composite droplets have also been observed [14]. It is desirable to avoid droplet formation as this will adversely affect the material quality.

Use of low growth temperatures is also detrimental to material quality, as this reduces the diffusion length of the surface adatoms, which in turn reduces the likelihood of an atom reaching a correct lattice site. Because of this, GaAs grown at low temperatures typically exhibits large concentrations of As antisite defects, As_{Ga}, and gallium vacancies, V_{Ga} [15-17]. These defects will introduce trap states within the band gap and reduce the optical and electrical quality of the material. However since there is a maximum temperature that can be used to incorporate a given fraction of Bi, there is a compromise between achieving the best material quality and the desired Bi content.

4.1.4 Surface reconstructions

Masnadi-Shirazi et al. [18] observed the different surface reconstructions present during GaAs and GaAsBi growth using RHEED. The two main surface reconstructions observed during GaAsBi growth are the (1×3) and (2×1) reconstructions. While a (1×3) reconstruction is also observed for low temperature growth of GaAs, the (2×1) is specific to GaAsBi growth. Growth with a (2×1) reconstruction was found to give higher Bi incorporation and better optical quality, as determined by photoluminescence measurements [18]. The (2×1) consists of Bi dimers oriented along the [-110] direction [19]. Since a perfect (2×1) consists of a full atomic layer of Bi on top of a full atomic layer of Ga, it can be considered as a metallic monolayer of GaBi [20]. In contrast to the standard growth modes (step-flow and islanding), growth with this reconstruction is anisotropic.

4.1.5 Growth regimes

Since GaAsBi growth is dependent on many factors (i.e. growth temperature, flux ratios, growth rate), there are many different growth regimes that can be used.

In 2008 Lu et al. [13] reported that using a low growth rate of 0.07 μm/h gave GaAsBi layers with Bi contents up to 10%, with low densities of Bi droplets on the surface. In contrast, Ptak et al. [21] proposed using high growth rates, and achieved Bi contents up to 9%. Using high growth rates kinetically inhibits the Bi from segregating to the surface and allows the growth of high Bi content layers with low amounts of surface Bi. In this case, Bi behaves as a dopant and the Bi content is proportional to the Bi flux. However, using such a regime does not allow growth at the maximum possible temperature for a given [Bi].

Lewis et al. [22] introduced a growth model which predicted that $[Bi]_{max}(T)$ can be achieved only when the As_2:Ga flux ratio is close to the stoichiometric value and the Bi flux is high. In this case access to $[Bi]_{max}(T)$ resulted in the formation of Bi droplets. In this work they were able to achieve a Bi content of 22% using a growth temperature of 200 °C, which is the highest Bi content reported to date.

In order to grow at the maximum possible temperature for a given [Bi], high Bi fluxes are required, and this leads to a population of Bi atoms on the epilayer surface. While this is not necessarily a problem for growing quantum wells/thin layers, when growing thick layers the accumulation of surface Bi needs to be considered.

4.1.6 Overview of chapter

In the growth of GaAsBi layers previously reported by this group [11], a 30 nm thick GaAsBi layer with 6% Bi showed good structural characteristics (as assessed by XRD), while a 160 nm thick layer grown under the same conditions showed degraded characteristics. The intensity of the RHEED pattern was also observed to degrade after approximately 80 nm of growth. In this chapter the growth of p-i-n diode structures containing GaAsBi layers with ~6% Bi is described. To combat the degradation of GaAsBi layer quality with increasing thickness, a growth interrupt technique is used in order remove excess Bi from the surface. The samples were characterized structurally using XRD, TEM and SIMS.

All samples in this work were grown by F. Bastiman. Where characterisation was carried out by other collaborators this has been noted in the text.

4.2 Doping calibration samples

Before growing the diode structures containing GaAsBi layers, the Be and Si doping concentrations were calibrated. This was done by growing a series of doped GaAs test structures and measuring the doping concentrations using SIMS. The samples were grown using a sample temperature of ~600 °C and a growth rate of 160 nm/hour.

For each test structure, a range of dopant cell temperatures was used and 100 nm of doped GaAs was grown for each temperature. The doping profiles obtained for these samples thus exhibit a 'step-like' form. Typical SIMS profiles are shown in Figure 4.1.

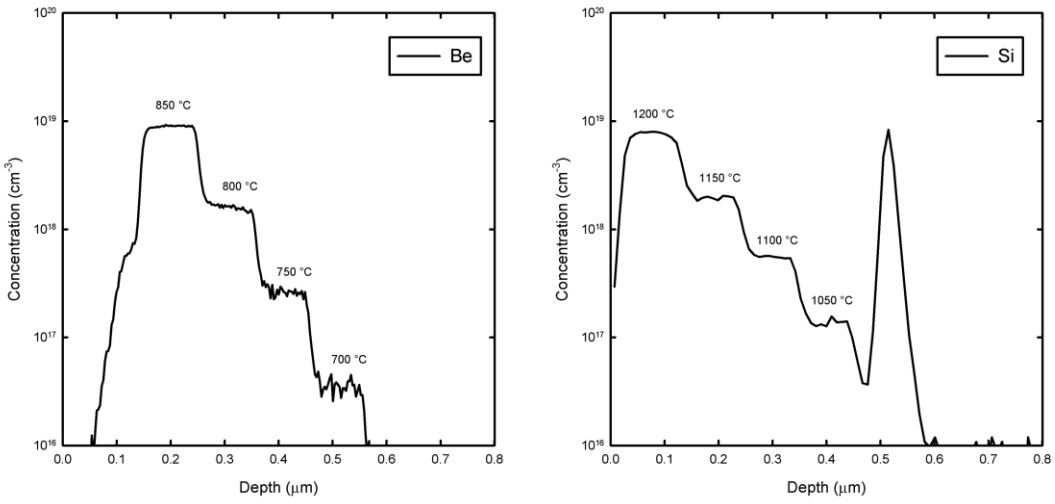

Figure 4.1: SIMS profiles for samples doped with Be (STB036) and Si (STB037).
The cell temperatures used for the growth of each region are shown.

4.3 STB03 samples

Once the doping profiles were obtained, the cell temperature required for a given doping concentration could be calculated. p-i-n diode structures containing undoped GaAs and GaAsBi layers were then grown on Si-doped (001) GaAs substrates. A growth rate of 160 nm/hour was used for all samples.

100 nm p-type GaAs (8×10^{18} cm^{-3})	100 nm p-type GaAs (8×10^{18} cm^{-3})
220 nm undoped GaAs	Undoped GaAs spacer
	Undoped GaAsBi
	Undoped GaAs spacer
160 nm n-type GaAs	160 nm n-type GaAs
n+ GaAs substrate (4×10^{18} cm^{-3})	n+ GaAs substrate (4×10^{18} cm^{-3})

Table 4.1: Sample structures for GaAs control sample (left) and samples containing GaAsBi layers (right).

The structures of the p-i-n diodes are shown above. The doping concentration of the n-type GaAs was 2×10^{18} cm^{-3} for samples STB038 and STB039; this was reduced to 7.5×10^{17} cm^{-3} for the rest of the samples. Undoped GaAs spacers were used to try to reduce dopant diffusion into the GaAsBi layers.

The GaAsBi thickness used for sample STB039 was 200 nm. As with the samples in [11], the RHEED quality deteriorated towards the end of the growth of the GaAsBi layer, therefore the layer thickness was reduced to 53 nm for the following samples. Samples STB03A, B and C also showed poor RHEED; therefore the Bi cell temperature was reduced for sample D. This gave good RHEED quality to the end of the GaAsBi layer, though slight 'spottiness' was observed indicating surface roughening. For sample E, the sample temperature was reduced slightly for the growth of the GaAsBi layer and the RHEED quality improved further. No structural characterisation was performed on these samples before or after device processing.

4.4 STB06 samples

4.4.1 Growth details

For the next set of diode samples (STB06), four samples with GaAsBi layers of different thicknesses were grown, along with a GaAs control sample. In order to grow GaAsBi layers > 50 nm thick, a growth interrupt method was used. A growth rate of 160 nm/hour was again used for all samples. The Bi content of the GaAsBi layers was nominally 6%.

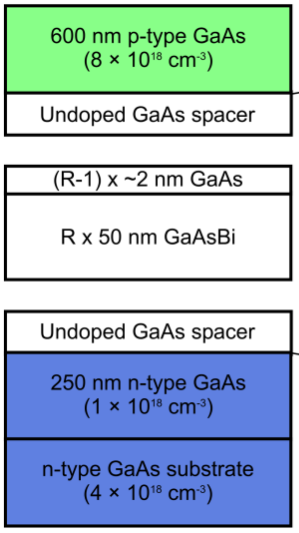

Sample	GaAs spacer thickness (nm)	Number of repeats, R
STB062	25	1
STB063	16	2
STB064	10	4
STB065	10	7

Table 4.2: Sample structures for GaAs control sample (left) and samples containing GaAsBi layers (right).

The GaAs control sample (STB061) comprised a 250 nm n-doped GaAs buffer followed by a 400 nm undoped GaAs active region and a 600 nm p-doped GaAs capping layer. The sample temperature was 580 °C throughout.

For the samples with GaAsBi layers, growth comprised a 250 nm n-doped GaAs buffer grown at 580 °C, followed by a thin undoped GaAs spacer. After the spacer growth, the sample was annealed at the buffer growth temperature for 5 minutes to obtain a flat surface and the substrate temperature was then lowered to 380 °C. A Bi flux was then incident on the surface for 30 seconds and the substrate temperature was left to stabilize for 20 minutes before beginning GaAsBi growth. During the GaAsBi growth, the Bi shutter was closed after every 50 nm for approximately 1 minute and ~2 nm of GaAs was grown with no Bi flux present, this was repeated until the desired GaAsBi layer thickness was achieved. After growing the final GaAsBi layer, a further thin undoped GaAs spacer was grown at the same temperature. Finally, the sample temperature was increased to 575 °C and 600 nm of p-doped GaAs was grown.

4.4.2 RHEED observations

During growth of the samples containing GaAsBi layers, the evolution of the RHEED pattern was monitored. A (2×4) pattern was observed during growth of the n-type GaAs buffer and the undoped GaAs spacer. As the substrate temperature was reduced to 380 °C prior to GaAsBi growth, a c(4×4) pattern emerged, indicating the adsorption of an 1.25 monolayers of As [23]. For the last 30 seconds when a Bi flux was incident on the surface, the pattern changed to (n×3), where n = 1, 2 or 4. However it was not possible to determine which of these is present, as the sample cannot be rotated to observe the other azimuth due to the limitation of the MBE system. The (n×3) has been proposed to consist of Bi dimers back bonded on As dimers [20].

After the first 5-10 seconds of GaAsBi growth, a (2×1) reconstruction was observed. The onset of the (2×1) coincides with the deposition of a total of approximately one monolayer of Ga. As mentioned in section 4.1.4, the (2×1) is believed to consist of one monolayer of GaBi. However in the same duration, the total Bi flux is only ~0.15 monolayers, and therefore the only way a single monolayer of GaBi can form in this time is if the 0.75 monolayers of Bi inside the (n×3) reconstruction contributes to the Bi surface population during the onset of growth and all the Bi surface segregates to the exposed surface. Hence it might be assumed that Bi incorporation is delayed until after a single ML is present in the surfactant layer.

When the GaAs spacers were grown with no Bi flux present, the surface reconstruction evolved from the (2×1) to an (n×3). During growth of the final undoped GaAs spacer layer an (n×3) reconstruction was also observed. It is unclear whether Bi persists on this spacer prior to ramping the temperature to grow the p-type cap, since both GaAsBi and GaAs exhibit a dynamic (n×3) reconstruction at this growth temperature [18]. Upon increasing the sample temperature to grow the p-type GaAs cap, a (2×4) reconstruction was observed and hence all excess Bi was definitely removed prior to the cap.

4.4.3 TEM characterisation

TEM imaging was performed on samples STB062, STB064 and STB065 by Dr. R. Beanland at the University of Warwick.

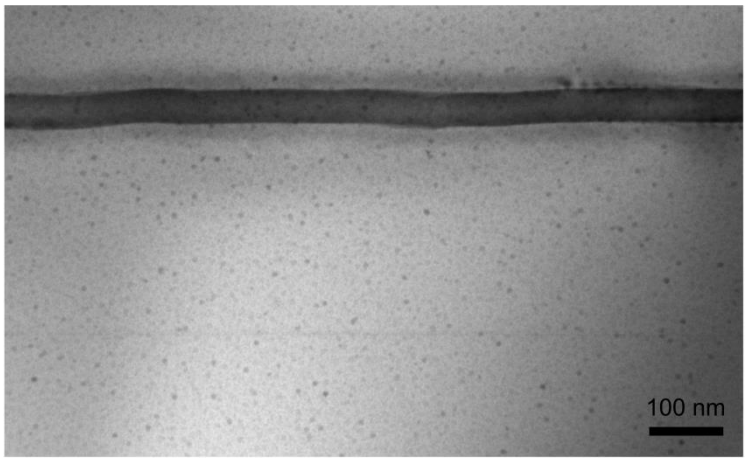

Figure 4.2: Bright-field (002) TEM image of STB062.

Figure 4.2 shows a TEM image of STB062. The spottiness observed in the image is a product of the sample preparation and is not related to the sample structure. The GaAsBi layer is visible as a dark band across the image. It can be seen that the interfaces are not perfectly flat and the structure of the whole layer appears uneven. The effect of this on the electronic properties of the sample is addressed in later chapters.

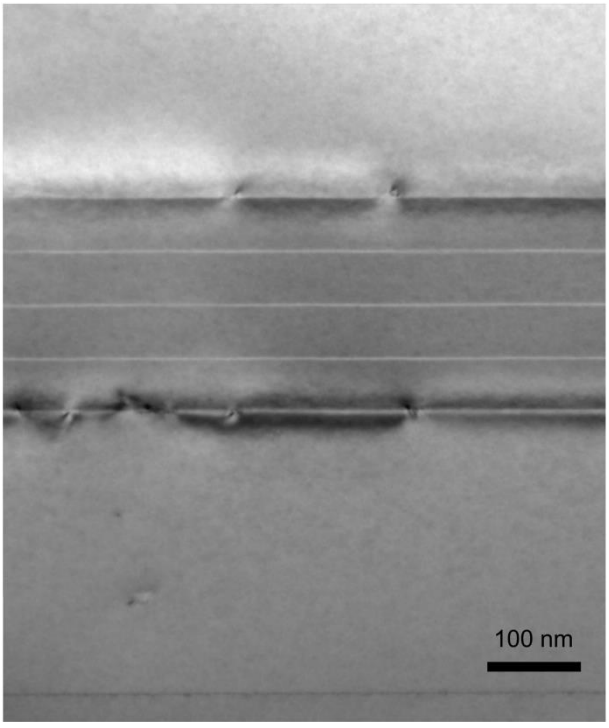

Figure 4.3: Bright field (002) TEM image of STB064.

Figure 4.3 shows a TEM image of sample STB064. Unlike STB062 the interfaces are flat. The ~200 nm GaAsBi layer is made up of 50 nm units, each separated by ~2 nm of GaAsBi with lower [Bi]. This is a result of the growth interrupt method used.

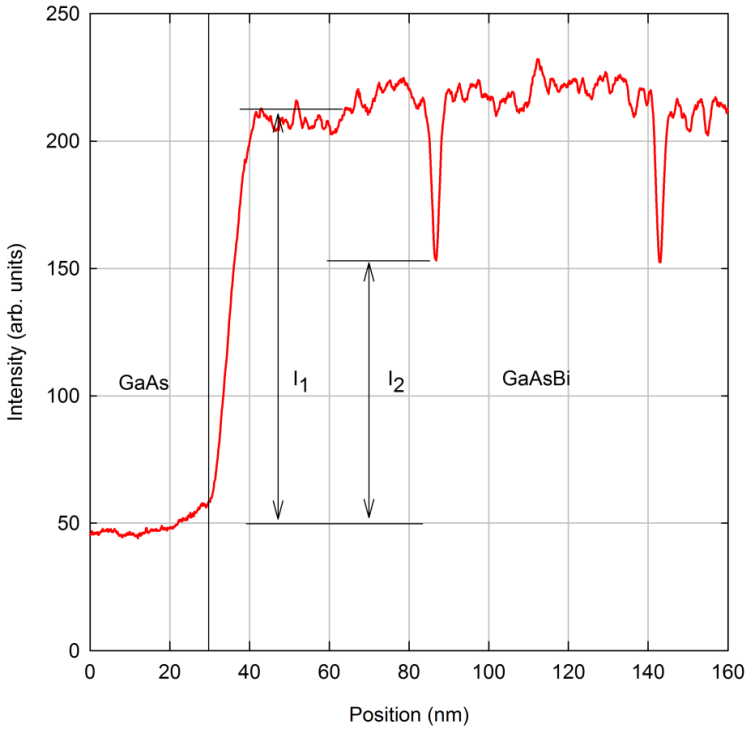

Figure 4.4: Line profile showing Bi concentration as a function of thickness obtained from figure 4.3.

The Bi content of the thin spacer layers can be estimated from analysis of the intensity, *I*, in a dark field (002) image of the thinnest part of the TEM specimen. Comparing the intensity of the spacer layer to that of GaAs and the 50 nm thick GaAsBi layers, and using the predicted linear dependence of the diffracted amplitude of the (002) beam on composition, the minimum value for $x_{spacer} \approx x(I_1/I_2)^{0.5} \approx 0.045$. Therefore, at this temperature Bi incorporation can obviously proceed from the Bi rich surface layer without being replenished from an external flux.

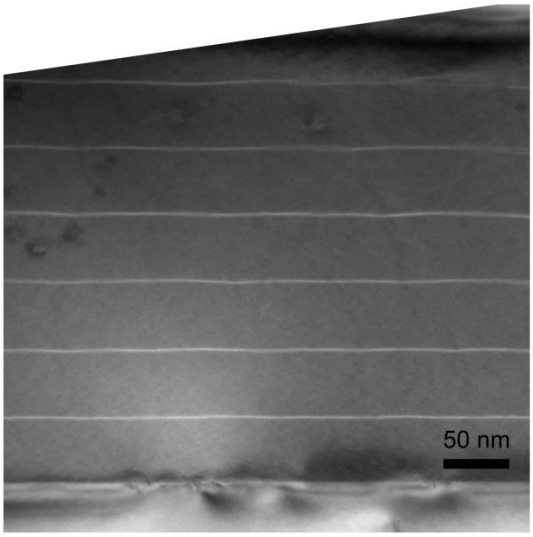

Figure 4.5: Bright field (002) TEM image of STB065.

The TEM image for STB065 in Figure 4.5 also shows this ‘multi-layer’ structure, which suggests Bi incorporation in the spacers is also occurring in this sample.

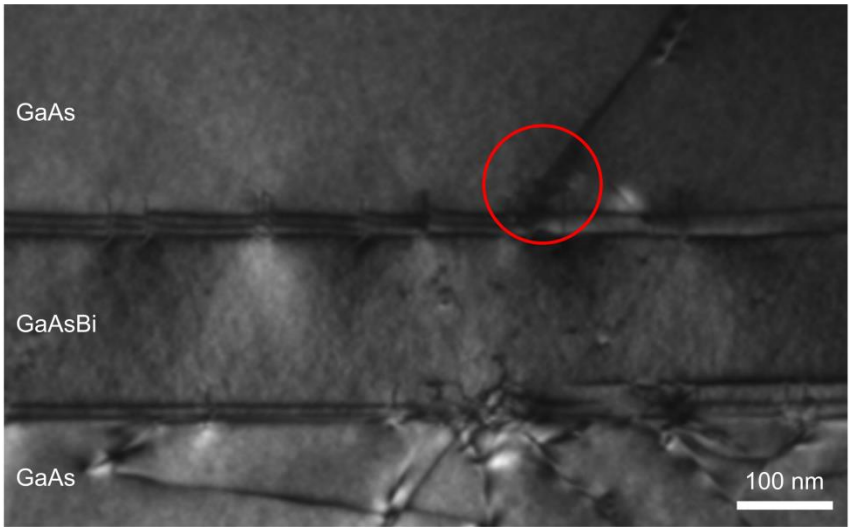

Figure 4.6: Bright field (002) TEM image of STB065.
The start of a dislocation at the upper GaAsBi/GaAs interface is circled in red.

The TEM image of a larger area in STB065 (Figure 4.6) shows 60° dislocations in both the GaAsBi layers and the surrounding GaAs layers, which are observed in other lattice-mismatched III-V systems such as InGaAs/GaAs [24].

4.4.4 Growth model

Growing with no Bi flux creates spacers with a lower Bi content than the surrounding layers and allows the surface to recover, as evidenced by the sustained intensity of the RHEED pattern. It is not clear whether this is due to depleting Bi from the near surface layers or planarising the anisotropic GaAsBi surface layers.

During growth, the Bi adatom population is increased by the adsorption of Bi atoms both from the incident flux and from near surface Bi segregating to the surface. The population is decreased by Bi adatoms incorporating into the bulk or desorbing from the surface, possibly aided by an As flux. According to the Ga:Bi flux ratio used for GaAsBi growth, the maximum possible [Bi] is 10.8% (if all the Bi atoms were incorporated). Since the achieved [Bi] is ~6%, this implies that approximately half of the irradiating Bi atoms are being incorporated. Once a (2×1) reconstruction is observed, the Bi adatom population of the upper layer is considered to be 100%. It is possible that a Bi-enriched sub-surface layer is formed, in a similar way to that predicted from the InAs-InBi phase diagram [25] and observed in thin epitaxial InAsBi layers [26]. The sub-surface layers would therefore contain a high [Bi] and would readily participate in surface segregation. The entire surface region is therefore metastable and super-saturated compared to the underlying layers. Interrupting the GaAsBi growth and growing with no Bi flux may consume the surface Bi and/or near-surface Bi. This allows the near-surface region to return to a stable sub-saturation state and produces thin GaAsBi layers with a lower Bi content.

Whilst droplets can readily occur from oversupply of atomic flux, it is also possible that the process of phase separation provides an additional route to droplet formation. Since GaBi is immiscible the result of GaAsBi phase separation under an excess of external As would be Bi droplets and GaAs. Due to the large size of the Bi atoms, there is the potential for growth to move away from the layer-by-layer Frank-van der Merwe (F-M) mode. Layer-by-layer growth is encouraged by the Bi surfactant effect, which enhances adatom mobility [3, 4]. However, the growth of GaAsBi with a (2×1) reconstruction promotes a purely anisotropic "reconstruction orientated" growth regime in the [-110] direction [20], and in addition, increasing the GaAsBi layer thickness increases the total compound strain energy (γ_{AB}^{ϵ}), which forces growth away from the layer-by-layer mode. Growth eventually becomes divided between multiple monolayers, and the surfactant nature of Bi cannot recover the surface, it merely ensures all available sites are filled upon the multi-monolayer surface. Eventually the surface begins to undulate as the anisotropic, densely packed islands occupy an increasing number of monolayers [20]. Interrupting the growth and growing with no Bi flux allows recovery from this undulated surface. The excess Bi on the surface continues to act as a surfactant and the GaAs can planarise the surface with no increase in strain energy γ_{AB}^{ϵ}, preventing the onset of phase separation, which was observed for $GaAs_{0.87}Bi_{0.13}$ layers in [27] and $GaAs_{0.94}Bi_{0.06}$ layers in [11].

4.4.5 SIMS results

SIMS profiles were obtained for samples STB064 and STB065 by Dr. D. Sykes at Loughborough Surface Analysis Ltd. The data were quantified using reference samples of silicon and beryllium in GaAs, and the depth scales were determined by measuring the sputtered crater depths using a Dektak surface profiler. The Bi concentration could not be obtained directly from the profiles as no calibration sample was present in order to convert the measured counts/second to a concentration value. However since the Bi content (from X-ray diffraction measurements, section 4.4.6) is around 6%, the average of the high Bi content region has been set to this value (assuming all the Bi is incorporated by substitution on As sites [28]).

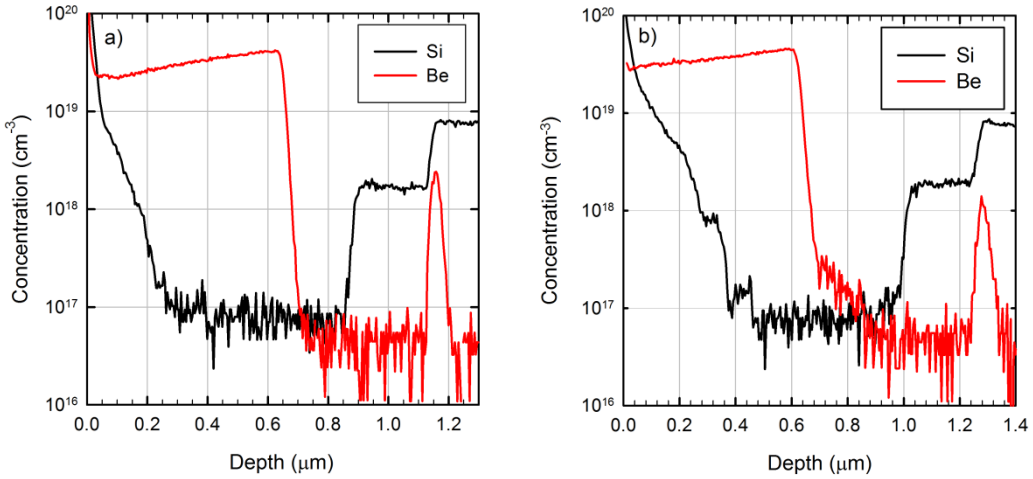

Figure 4.7: Doping profiles for STB064 (a) and STB065 (b).

SIMS profiles for the dopants are shown in Figure 4.7. The Be concentration in the p-type GaAs regions is higher than intended, owing to a small miscalibration of the Be cell flux. The Si concentrations in the substrate and the n-type buffer correspond to the expected values.

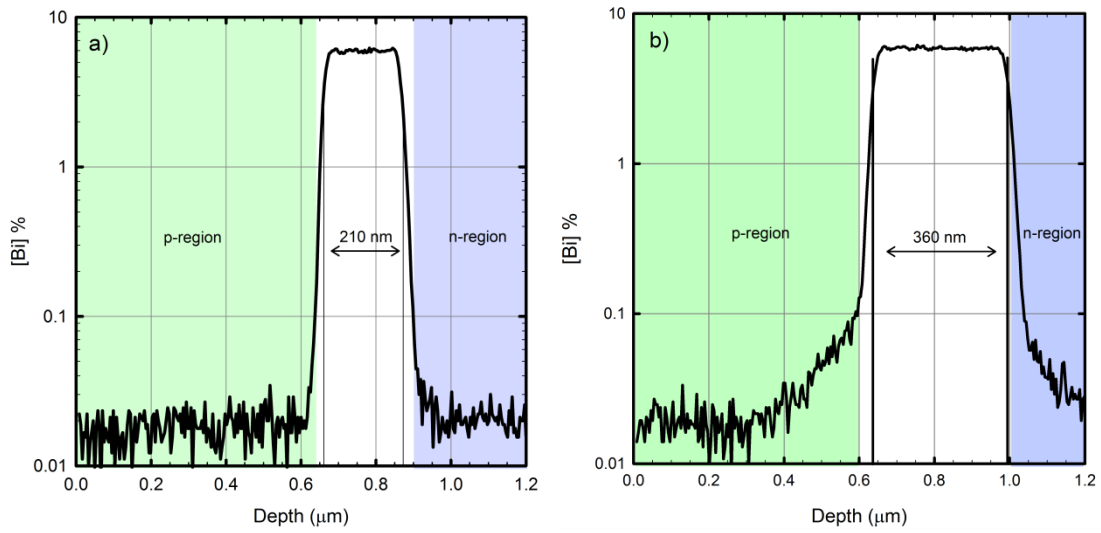

Figure 4.8: Bi depth profiles for STB064 (a) and STB065 (b).

SIMS profiles for Bi are shown in Figure 4.8. The counts/second values in the high [Bi] regions did not vary significantly between the two samples, suggesting that they have similar [Bi]. The GaAsBi thicknesses are within 5% of the intended values. The variation in the average Bi concentration is no more than 0.25%, and there is no sign of a drop in Bi concentration towards the p-cap, as might be expected if the quality of the epitaxy was deteriorating.

The SIMS profiles also show that there is only a negligible amount of Bi outside the GaAsBi layer, meaning that there has been no Bi out diffusion despite the fact that the p-GaAs region is grown over several hours at a higher temperature. While an earlier rapid thermal annealing study [29] showed no evidence of Bi out-diffusion at 600 °C for a GaAsBi sample with 6.5% Bi, this result shows that there is little out-diffusion even for longer annealing times.

4.4.6 XRD results

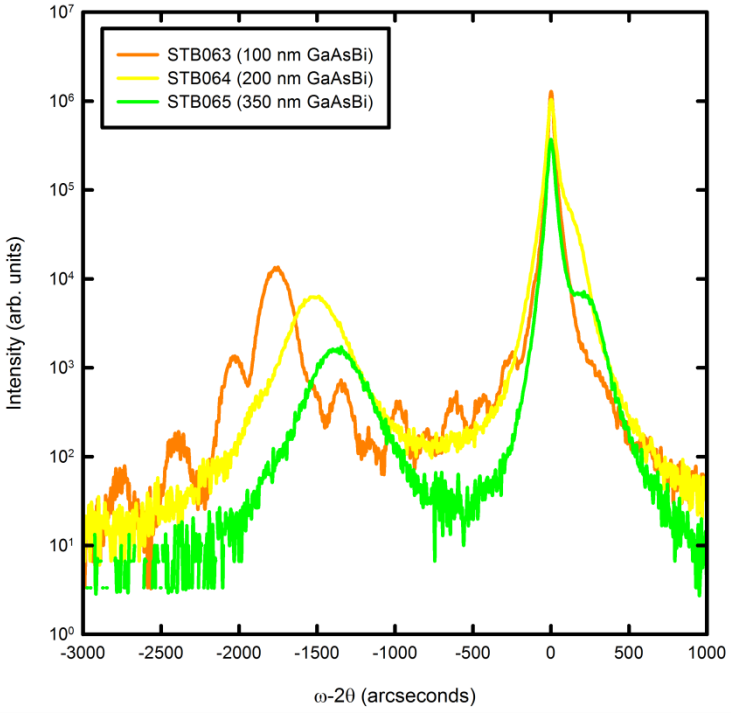

Figure 4.9: (004) XRD scans for STB063, STB064 and STB065.

Before sample processing, (004) high resolution X-ray diffraction (HR XRD) ω-2θ scans were performed on samples STB063, STB064 and STB065. The spectra are shown in Figure 4.9. The spectrum for sample STB063 exhibits Pendellösung fringes, indicating good quality GaAsBi/GaAs interfaces. In contrast, the spectra for samples STB064 and STB065 show broader epi-layer peaks without fringes. Reasons for this will be addressed in section 4.4.7.

The bismuth content for STB063 was determined by fitting the XRD spectrum using RADS Mercury software. A good fit to the data was obtained assuming no relaxation in the GaAsBi layer; therefore it is assumed that the layer is fully strained to the substrate. The fit is shown in Figure 4.10. The (004) plane spacing was calculated from the GaAsBi peak position using Bragg's law. This was found to be 1.432 Å, corresponding to a lattice parameter of 5.728 Å. The unstrained lattice parameter can then be calculated, assuming Poisson's ratio is the same as that of GaAs (0.311). Using Vegard's law and a GaBi lattice constant of 6.324 Å [30] then gives a bismuth content of 5.9%. As mentioned in section 4.1.2, another value for the GaBi lattice constant that is sometimes used in the literature is that calculated by Tixier et al. [1], who extrapolated a value from lattice constants determined for pseudomorphic GaAsBi samples from

XRD measurements. This value was found to be 6.33 ± 0.06 Å. Using this range of values instead of the theoretical value gives an absolute variation in Bi content of no more than 0.5 %.

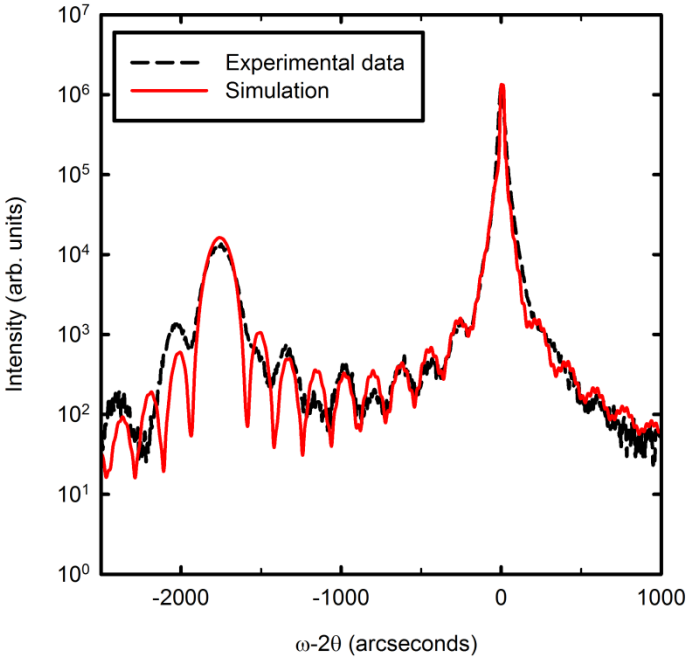

Figure 4.10: XRD data and simulation for sample STB063.

The epi-layer thickness, *t*, can be obtained from the period of the Pendellösung fringes using the equation [31]

$$t = \frac{\lambda}{\delta\theta \; 2cos\theta_B} \tag{4.1}$$

where λ is the X-ray wavelength, $\delta\theta$ is the fringe separation and θ_B is the Bragg angle of the epi-layer peak. This assumes that the angle between the (004) plane and the sample surface is zero. The GaAsBi layer thickness was determined to be 108 nm, which is close to the expected thickness of two 50 nm layers separated by a spacer which is ~5 nm thick.

The XRD measurements were performed before the TEM measurements and thus the spacer with different Bi content was not originally included in the simulation, i.e. a uniform GaAsBi layer was assumed. Although TEM measurements were not performed on STB063, it is likely that a spacer with lower Bi content exists in the same way as for STB064 and STB065. To verify this, another simulation was performed. The results are shown in Figure 4.11.

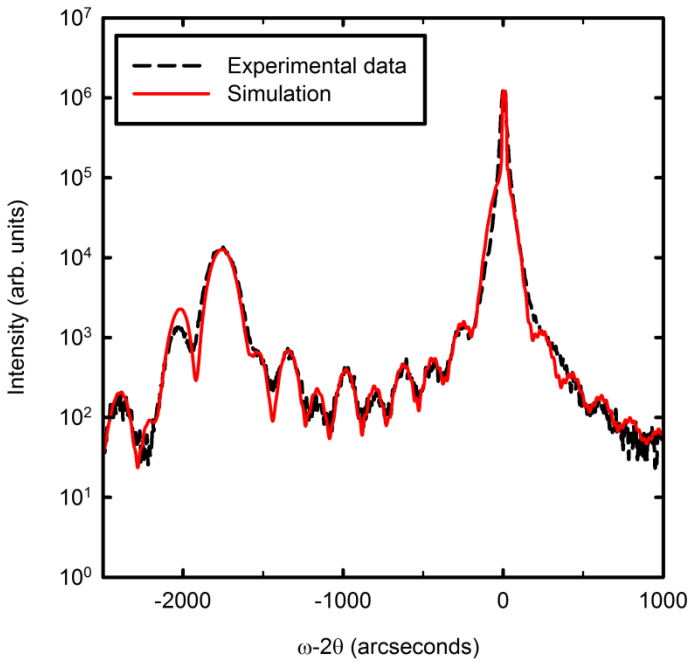

Figure 4.11: XRD data and simulation for sample STB063, including a spacer in the GaAsBi layer.

The fit is much better when the spacer is included, suggesting that such a spacer does exist within the layer. The structure from the simulation is 50 nm GaAsBi with 6.3% Bi, 6 nm with 3.9% Bi and 50 nm with 6% Bi. The ratio of [Bi] in the spacer to the [Bi] in the bulk-like regions is thus similar to that observed in STB064 from the TEM measurements. Since the GaAsBi regions are grown under the same conditions there is no reason to expect a variation in [Bi] between the two layers and the Bi contents are likely the same within experimental error. The full structures used for the simulations in Figures 4.10 and 4.11 are given in Appendix A.

4.4.7 Relaxation

As similar growth conditions were used for all samples, the bismuth content is not expected to vary significantly between the layers. This is supported by optical measurements presented in chapter 5. Since the TEM measurements showed dislocations in the thicker layers, it is likely that the shift in epi-layer peak for samples STB064 and STB065 is due to relaxation in the GaAsBi layers, which reduces the (004) lattice spacing. The presence of dislocations leads to broadening of the peaks [32]. The full width at half maximum (FWHM) values of the epi-layer peaks are shown in Table 4.3. In comparison, the FWHM of the GaAs substrate peak for STB063 is 35 arcsec.

Sample	Epi-layer peak FWHM (arcsec)
STB063	120
STB064	280
STB065	320

Table 4.3: FWHM values for GaAsBi epi-layer peaks.

There are also additional peaks in the XRD spectra for STB064 and STB065 which are positively offset from the substrate peaks. Since there is no material in the structures with a lattice constant less than that of GaAs, there is not an obvious reason for this. However, if relaxation is present in the GaAsBi layers, the GaAs grown on the GaAsBi will be in tensile strain, with an out of plane lattice parameter less than that of unstrained GaAs. As the GaAs cap layer is 600 nm thick it may also relax, which will shift the peak back towards the substrate peak. This is illustrated in Figure 4.12.

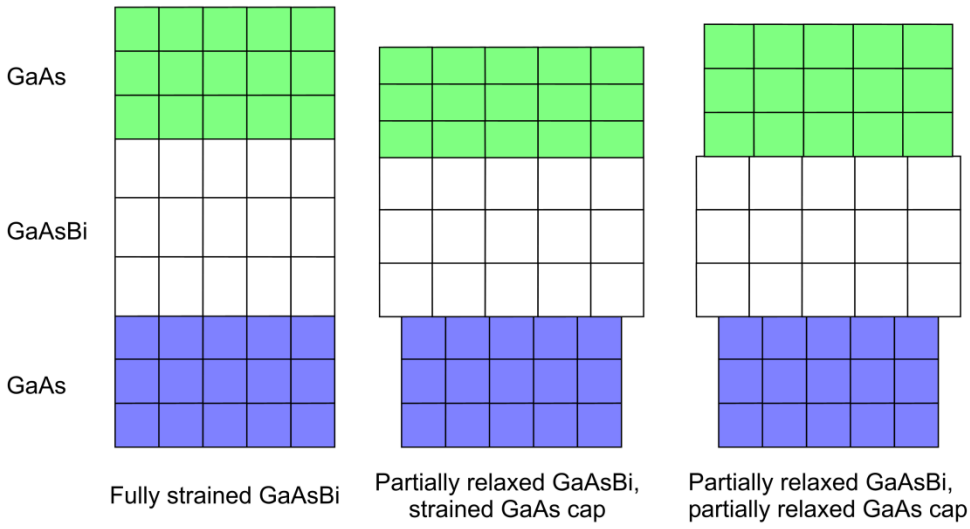

Figure 4.12: Diagrams showing variation in lattice parameters for different relaxation states within the sample.

To investigate the effect of relaxation on the XRD spectra, simulations were performed for the structure of sample STB064, with the bismuth content of the bulk-like regions assumed to be 6% and the content of the spacers to be 4.5%. These are shown in Figure 4.13. The simulation shows spectra with and without relaxation, with all other parameters kept constant. Introducing 30% relaxation in the GaAsBi layer shifts the GaAsBi peak by 250 arcsec to coincide with the measured GaAsBi peak and also creates a peak which is positively offset from the substrate peak. When the relaxation in the GaAs cap layer is set to 30%, this is shifted back towards the

substrate peak to coincide with the measured peak. The final position of the positively offset peak is therefore a convolution of the relaxation in both the GaAsBi and the GaAs cap layers. Along with the TEM measurements, this gives further evidence that the GaAsBi layers in STB064 and STB065 are partially relaxed. A similar feature has been observed for InGaAs multiple quantum wells grown on GaAs [33].

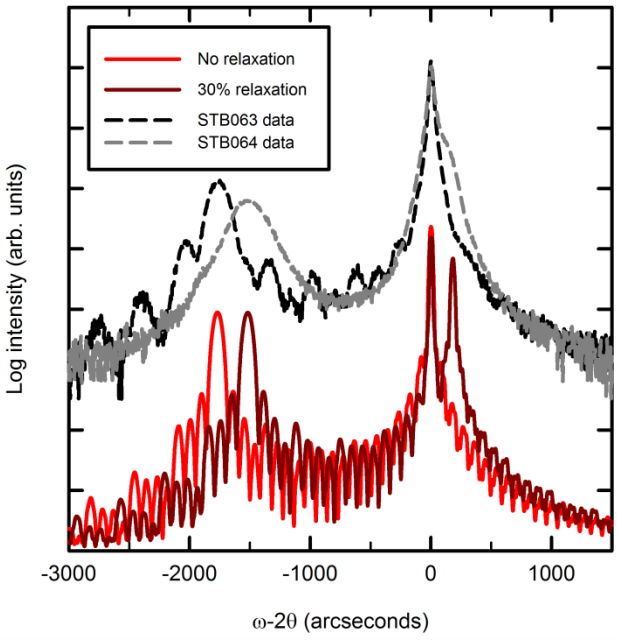

Figure 4.13: XRD data for samples STB063 and STB064, and simulations for the nominal structure of sample STB064 (with and without relaxation).

The epi-layer peak position for a symmetric scan such as a (004) scan depends on both the Bi composition and relaxation in the GaAsBi epi-layer. Thus for STB064 and STB065 there is a range of composition and relaxation values which will give the same lattice parameter, and the Bi composition cannot be obtained from the XRD data. This can be represented using a contour plot (Figure 4.14). The lattice parameter for STB064 is 5.72 Å and the parameter for STB065 is 5.71 Å. Details of the method used to create the plot are given in Appendix B.

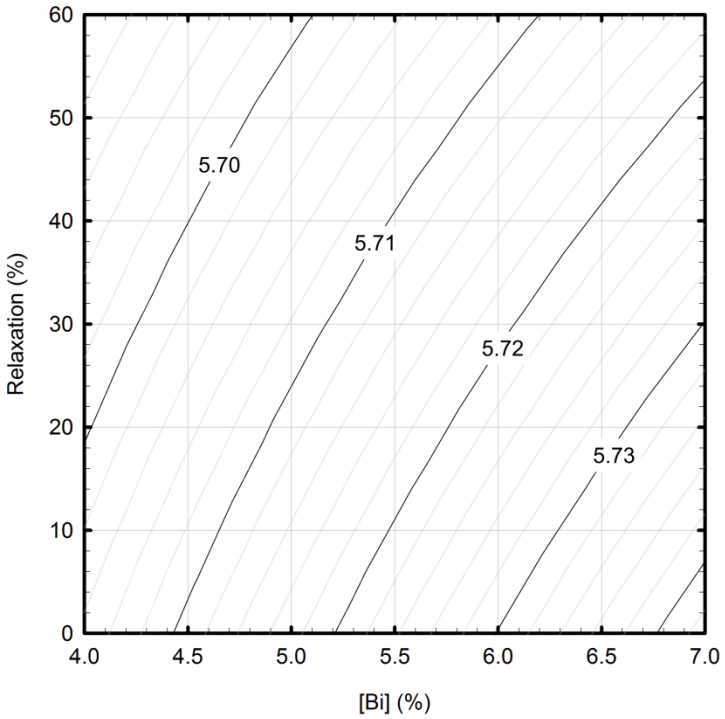

Figure 4.14: Contour plot showing variation of lattice parameter with Bi content and relaxation. Lattice parameters are in angstroms.

4.4.8 Critical thickness

These results suggest that the critical thickness for GaAsBi with ~6% Bi (grown at 380 °C) is between 100 and 200 nm. Many theories for calculating the critical thickness of a mismatched system have been proposed, e.g. by Matthews and Blakeslee [34], People and Bean [35], and Fischer [36]. The equations involved usually need to be solved numerically, however an analytical solution of the theory proposed by Fischer has been suggested [37].

In the Matthews-Blakeslee model, the force due to the strain and the force acting on a dislocation are considered, both of which depend on the epi-layer thickness. Balancing these forces gives an expression for the critical thickness, h_c. Many different formulations of the final equation have been given. Fitzgerald [38] gives a summary of some of these. The particular form given in Equation 22 from [38] is shown below.

$$h_c = \frac{b(1 - \nu cos^2\theta)[ln(h_c/b) + 1]}{8\pi\varepsilon(1+\nu)cos\varphi} \tag{4.2}$$

b is the magnitude of the Burgers vector, ν is the Poisson ratio, θ is the angle between the dislocation line and Burgers vector, ε is the lattice mismatch and φ is the angle between the slip plane and the interface normal.

Experimental data for both strained and relaxed GaAsBi layers are shown in Figure 4.15, along with the critical layer thickness predicted by the Matthews and Blakeslee model. The line separating the strained and relaxed data points is shown as a guide to the eye. The diagram shows that in all cases, the thicknesses of the strained GaAsBi layers greatly exceed the M-B critical thickness. This could be due to the low growth temperatures used for GaAsBi. The growth temperature has been shown to affect the critical thickness for the InGaAs/GaAs system [39, 40]. In the particular case of our layers, it is possible that the growth interrupts may inhibit relaxation by preventing the operation of dislocation multiplication mechanisms. Such mechanisms have been shown to be the main factor affecting relaxation in III-V epitaxy [41]. In addition, growing at low temperatures will also inhibit relaxation, as the energy available for formation of dislocations will be reduced [39, 42].

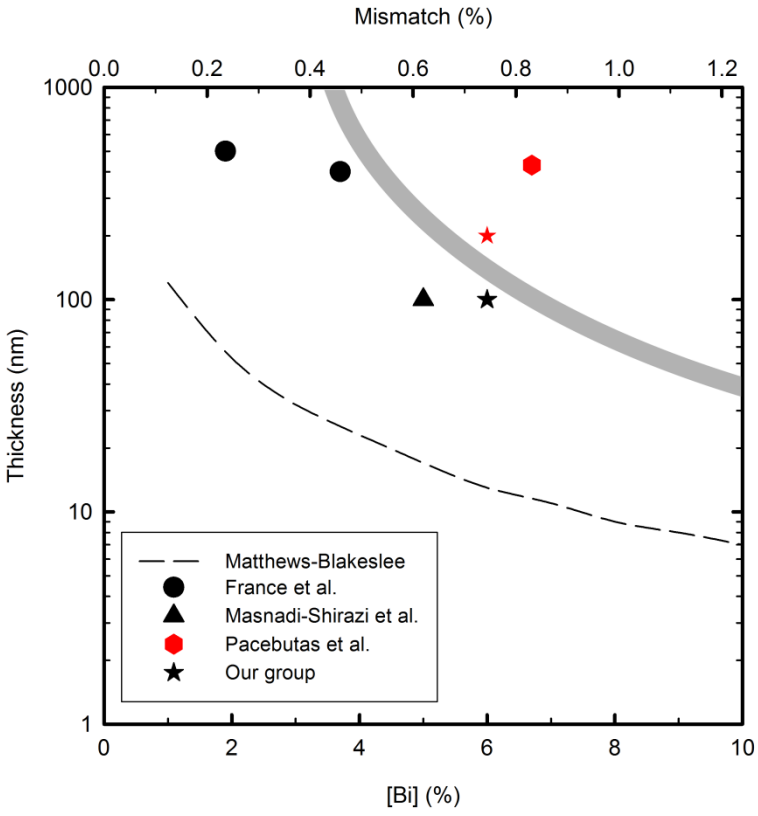

Figure 4.15: Graph showing data points for strained (black) and relaxed (red) GaAsBi layers. Data are taken from references [18, 43, 44].

4.4.9 Transmission electron diffraction and CuPt ordering

Transmission electron diffraction (TED) measurements were also carried out on sample STB064. The [110] TED pattern is shown in Figure 4.16. The 004 spot shows splitting along the [001] direction, due to the different lattice parameters of the GaAs and GaAsBi layers. From the peak position, the lattice parameter was determined to be 0.5714 nm.

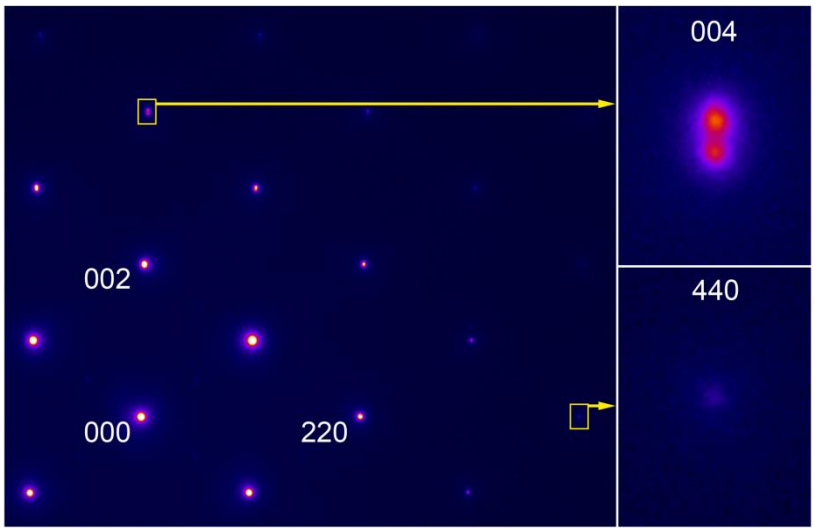

Figure 4.16: TED pattern for STB064 showing (004) peak splitting.

This value is in good agreement with the value determined from XRD. However, since the TEM sample is very thin (< 500 nm), it may relax in the direction perpendicular to the growth direction, which will affect the measured lattice parameter. In order to compare the XRD and TED values, the mismatch values of the (004) lattice parameters were calculated. The value obtained from the XRD is 0.0112 and the value from TED is 0.01022, which is consistent with a small amount (~10%) of surface relaxation in the thin TEM specimen. The 440 spot does not appear to show splitting, though any splitting will be much less than that for the 004 spot and thus difficult to detect.

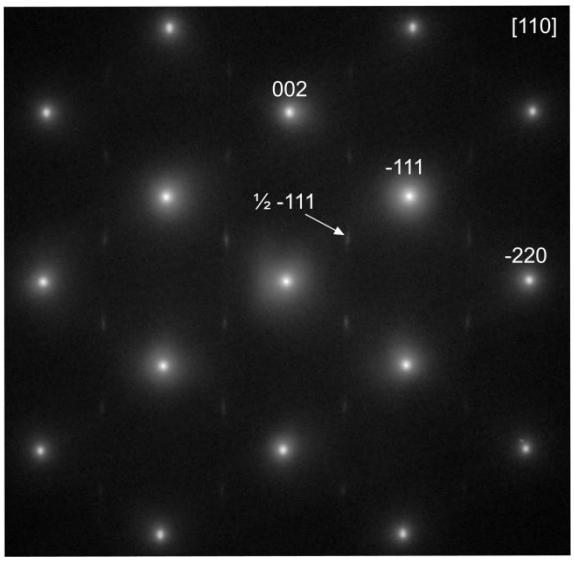

Figure 4.17: TED pattern for STB064 showing extra ½ 111 spots.

Weak ½ 111-type spots were observed in the TED pattern (Figure 4.17), which indicates the presence of extra ordering in the structure. In an ideal binary III-V semiconductor, there is only one type of atom at each lattice site, whereas for ternary or quaternary semiconductors, a lattice site may be occupied by one of two types of atom. e.g. for InGaAsP, a group III lattice site can be occupied by either an In or a Ga atom and a group V lattice site can be occupied by either an As or a P atom. In such compounds it is possible for extra ordering to exist, where the crystal structure repeats periodically along a given crystallographic direction in addition to the directions expected from the unit cell. Several types of ordering have been observed in III-V materials, the most common of which is CuPt-type ordering [45], which is named due to the ordering present in the CuPt alloy [46].

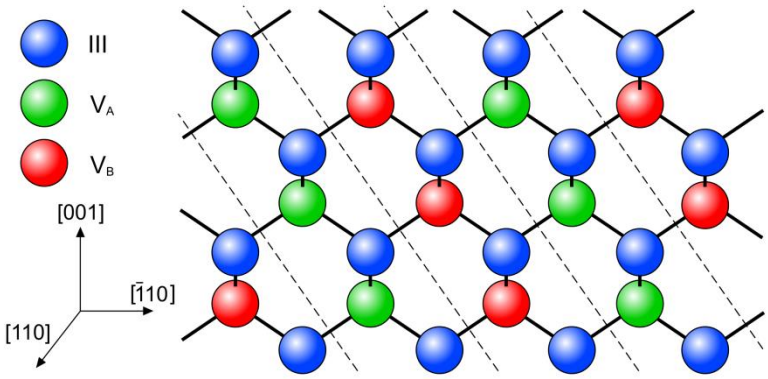

Figure 4.18: Diagram showing perfect CuPt-type ordering for a ternary compound containing two different group V species.

A diagram illustrating CuPt ordering is shown in Figure 4.18. In this type of ordering, the structure is ordered on the {111} planes. There are four equivalent {111} planes, however CuPt ordering is typically only observed on the (1-11) and (-111) planes. This form of CuPt ordering is referred to as $CuPt_B$ ordering, since the line of intersection of these planes with the (001) surface is parallel to that of the $\{111\}_B$ planes in which the group V atoms are uppermost [47]. This extra order causes spots to appear at ½,½,½-type points in reciprocal space, due to the periodicity of the lattice being doubled. For a dilute alloy such as GaAsBi, perfect ordering will consist of group V planes which alternate between As atoms only and a mix of Bi and As atoms.

Ordering has been shown to reduce the band gap compared to a disordered alloy [48-50]. This occurs because the presence of ordering reduces the symmetry of the crystal [49], leading to splitting of the valence band states. Since these effects will have an impact on devices, it is important to consider why ordering occurs and how it can be controlled.

From a thermodynamic perspective, the feasibility of formation of a disordered phase depends on the Gibbs free energy change, ΔG, which is given by

$$\Delta G = \Delta H - T\Delta S \tag{4.3}$$

where H is the enthalpy, S is the entropy and T the temperature in Kelvin. Both the enthalpy change and the entropy change on formation of a ternary compound are positive [45]. At high temperatures the entropy term dominates and disordered compounds can form. At low temperatures this term is negligible, so that the formation of the ternary is not feasible. In this case, phase separation can occur.

The enthalpy change for the formation of CuPt-ordered material is greater than for disordered material [51], and the entropy change will also be smaller. Thus from bulk thermodynamics there is no reason for ordered phases to form. However, this situation is only valid for an ideal crystal which is infinite in three dimensions. As mentioned in chapter 2, a surface exists in epitaxial growth and this gives rise to surface reconstructions, which are ordered along certain directions. In [51], it was suggested that surface order can be 'frozen in' to the bulk, since bulk diffusion in semiconductors is slow. The structure on the epitaxial surface therefore has an effect on the structure achieved in the bulk.

The orientation of the substrate is also an important parameter, as this affects the number of bonds available on the surface and thus the adatom mobility. While CuPt ordering has been observed for growth on (001) substrates, it is not observed for growth on (110), (111) or (113) substrates [47]. Phillips et al. [47] proposed a model which requires the existence of group V

surface atom dimers oriented along the [-110] direction during growth, which are not present for these substrate orientations. Thus while bulk thermodynamics predicts III-V materials to either phase separate or disorder, consideration of surface effects shows that ordering can occur and is affected by growth conditions and the type of substrate used.

Little information on CuPt ordering in the GaAsBi system exists in the literature. Norman et al. observed extra ½ {111} spots in TED patterns obtained from GaAsBi samples with 3%, 6% and 10% Bi [27], though no such spots were observed for a sample with 13% Bi. In agreement with Philips et al., it was suggested in this paper that CuPt ordering could be related to the surface reconstruction present during growth, specifically one containing tightly packed [-110] oriented dimers such as (2×1). This has also been supported by theoretical work [52]. The (2×1) reconstruction was observed for the growth of all GaAsBi layers in this work, in agreement with this hypothesis.

It is important to note that if there is a link between the presence of a (2×1) reconstruction and ordering, ordering will not be observed for growth regimes with low or negligible Bi surface coverage. In this case, ordering will require high Bi flux conditions.

The extent of the ordering in the GaAsBi layer is difficult to ascertain from the TED pattern. The ordering could be anything between perfect (alternating $\{111\}_B$ planes with and without Bi) to fully disordered (Bi on all $\{111\}_B$ planes). It is also not clear whether the ordering exists throughout the entire layer. Since ordered GaAsBi has higher strain than disordered GaAsBi, it is possible that ordering may occur at the beginning of the layer, close to the GaAs/GaAsBi interface and then undergo a transition to disorder after a certain thickness. This has been observed for other GaAsBi samples grown by this group [53].

For mixed group III compounds, the alloy composition is fixed by the group III flux ratios and therefore any variation in the band gap (as determined from PL) can be ascribed to ordering. However for GaAsBi the presence of ordering cannot be obtained from the value of the band gap alone since the incorporation process is more complex. It is thus difficult to decouple the effects of ordering and Bi content, and more work is needed to ascertain the role of ordering in this material system.

4.5 Summary

In this chapter the growth of thick undoped GaAsBi layers has been described. A growth interrupt method has been outlined which prevents degradation of the thicker GaAsBi layers and creates thin spacer layers with lower [Bi] than the surrounding bulk. SIMS measurements show that there is no large change in [Bi] throughout the GaAsBi layers and there is little outdiffusion into the surrounding GaAs barriers.

TEM images show the presence of dislocations in the thicker GaAsBi layers due to the mismatch between GaAsBi and GaAs, and this is supported by XRD measurements. The critical thickness is much greater than that predicted by the Matthews-Blakeslee theory, which could be due to the low growth temperature, as well as the use of growth interrupts. TED measurements show the presence of CuPt ordering in the GaAsBi layers, which could be linked to the (2×1) reconstruction present during growth and thus the specific growth conditions used.

4.6 References

[1] S. Tixier, M. Adamcyk, T. Tiedje, S. Francoeur, A. Mascarenhas, P. Wei, and F. Schiettekatte, "Molecular beam epitaxy growth of $GaAs_{1-x}Bi_x$," *Appl. Phys. Lett.*, vol. 82, pp. 2245-2247, 2003.

[2] R. R. Wixom, L. W. Rieth, and G. B. Stringfellow, "Sb and Bi surfactant effects on homo-epitaxy of GaAs on (0 0 1) patterned substrates," *J. Cryst. Growth*, vol. 265, pp. 367-374, 2004.

[3] S. Tixier, M. Adamcyk, E. C. Young, J. H. Schmid, and T. Tiedje, "Surfactant enhanced growth of GaNAs and InGaNAs using bismuth," *J. Cryst. Growth*, vol. 251, pp. 449-454, 2003.

[4] M. R. Pillai, S. Kim, S. T. Ho, and S. A. Barnett, "Growth of $In_xGa_{1-x}As$/GaAs heterostructures using Bi as a surfactant," *J. Vac. Sci. Technol., B*, vol. 18, pp. 1232-1236, 2000.

[5] B. Joukoff and A. M. Jean-Louis, "Growth of $InSb_{1-x}Bi_x$ single crystals by Czochralski method," *J. Cryst. Growth*, vol. 12, pp. 169-172, 1972.

[6] A. J. Noreika, W. J. Takei, M. H. Francombe, and C. E. C. Wood, "Indium antimonide-bismuth compositions grown by molecular beam epitaxy," *J. Appl. Phys.*, vol. 53, pp. 4932-4937, 1982.

[7] R. F. C. Farrow, "The stabilization of metastable phases by epitaxy," *J. Vac. Sci. Technol., B,* vol. 1, pp. 222-228, 1983.

[8] K. Oe and H. Okamoto, "New Semiconductor Alloy $GaAs_{1-x}Bi_x$ Grown by Metal Organic Vapor Phase Epitaxy," *Jpn. J. Appl. Phys.,* vol. 37, p. L1283, 1998.

[9] S. Francoeur, M. J. Seong, A. Mascarenhas, S. Tixier, M. Adamcyk, and T. Tiedje, "Band gap of $GaAs_{1-x}Bi_x$, $0 < x < 3.6\%$," *Appl. Phys. Lett.,* vol. 82, pp. 3874-3876, 2003.

[10] M. Yoshimoto, S. Murata, A. Chayahara, Y. Horino, J. Saraie, and K. Oe, "Metastable GaAsBi Alloy Grown by Molecular Beam Epitaxy," *Jpn. J. Appl. Phys.,* vol. 42, p. L1235, 2003.

[11] F. Bastiman, A. R. B. Mohmad, J. S. Ng, J. P. R. David, and S. J. Sweeney, "Non-stoichiometric GaAsBi/GaAs (100) molecular beam epitaxy growth," *J. Cryst. Growth,* vol. 338, pp. 57-61, 2012.

[12] R. D. Richards, F. Bastiman, C. J. Hunter, D. F. Mendes, A. R. Mohmad, J. S. Roberts, and J. P. R. David, "Molecular beam epitaxy growth of GaAsBi using As_2 and As_4," *J. Cryst. Growth,* vol. 390, pp. 120-124, 2014.

[13] X. Lu, D. A. Beaton, R. B. Lewis, T. Tiedje, and M. B. Whitwick, "Effect of molecular beam epitaxy growth conditions on the Bi content of $GaAs_{1-x}Bi_x$," *Appl. Phys. Lett.,* vol. 92, pp. 192110-3, 2008.

[14] G. Vardar, S. W. Paleg, M. V. Warren, M. Kang, S. Jeon, and R. S. Goldman, "Mechanisms of droplet formation and Bi incorporation during molecular beam epitaxy of GaAsBi," *Appl. Phys. Lett.,* vol. 102, pp. 042106-4, 2013.

[15] M. Kaminska, E. R. Weber, Z. Liliental-Weber, R. Leon, and Z. U. Rek, "Stoichiometry-related defects in GaAs grown by molecular-beam epitaxy at low temperatures," *J. Vac. Sci. Technol., B,* vol. 7, pp. 710-713, 1989.

[16] M. Kaminska, Z. Liliental-Weber, E. R. Weber, T. George, J. B. Kortright, F. W. Smith, B. Y. Tsaur, and A. R. Calawa, "Structural properties of As-rich GaAs grown by molecular beam epitaxy at low temperatures," *Appl. Phys. Lett.,* vol. 54, pp. 1881-1883, 1989.

[17] M. Luysberg, H. Sohn, A. Prasad, P. Specht, Z. Liliental-Weber, E. R. Weber, J. Gebauer, and R. Krause-Rehberg, "Effects of the growth temperature and As/Ga flux ratio on the incorporation of excess As into low temperature grown GaAs," *J. Appl. Phys.,* vol. 83, pp. 561-566, 1998.

[18] M. Masnadi-Shirazi, D. A. Beaton, R. B. Lewis, X. Lu, and T. Tiedje, "Surface reconstructions during growth of $GaAs_{1-x}Bi_x$ alloys by molecular beam epitaxy," *J. Cryst. Growth,* vol. 338, pp. 80-84, 2012.

[19] P. Laukkanen, M. P. J. Punkkinen, H. P. Komsa, M. Ahola-Tuomi, K. Kokko, M. Kuzmin, J. Adell, J. Sadowski, R. E. Perälä, M. Ropo, T. T. Rantala, I. J. Väyrynen,

M. Pessa, L. Vitos, J. Kollár, S. Mirbt, and B. Johansson, "Anomalous Bismuth-Stabilized (2 × 1) Reconstructions on GaAs(100) and InP(100) Surfaces," *Phys. Rev. Lett.,* vol. 100, p. 086101, 2008.

[20] F. Bastiman, A. G. Cullis, J. P. R. David, and S. J. Sweeney, "Bi incorporation in GaAs(100)-2×1 and 4×3 reconstructions investigated by RHEED and STM," *J. Cryst. Growth,* vol. 341, pp. 19-23, 2012.

[21] A. J. Ptak, R. France, D. A. Beaton, K. Alberi, J. Simon, A. Mascarenhas, and C. S. Jiang, "Kinetically limited growth of GaAsBi by molecular-beam epitaxy," *J. Cryst. Growth,* vol. 338, pp. 107-110, 2011.

[22] R. B. Lewis, M. Masnadi-Shirazi, and T. Tiedje, "Growth of high Bi concentration $GaAs_{1-x}Bi_x$ by molecular beam epitaxy," *Appl. Phys. Lett.,* vol. 101, pp. 082112-4, 2012.

[23] F. Bastiman, A. G. Cullis, and M. Hopkinson, "GaAs(0 0 1) (2 × 4) to c(4 × 4) transformation observed in situ by STM during As flux irradiation," *Surface Science,* vol. 603, pp. 2398-2402, 2009.

[24] N. J. Quitoriano and E. A. Fitzgerald, "Alternative slip system activation in lattice-mismatched InP/InGaAs interfaces," *J. Appl. Phys.,* vol. 101, pp. 073509-10, 2007.

[25] K. Y. Ma, Z. M. Fang, R. M. Cohen, and G. B. Stringfellow, "OMVPE growth and characterization of Bi-containing III–V alloys," *J. Cryst. Growth,* vol. 107, pp. 416-421, 1991.

[26] L. Dominguez, D. F. Reyes, F. Bastiman, D. L. Sales, R. D. Richards, D. Mendes, J. P. R. David, and D. Gonzalez, "Formation of Tetragonal InBi Clusters in InAsBi/InAs(100) Heterostructures Grown by Molecular Beam Epitaxy," *Appl. Phys. Express,* vol. 6, p. 112601, 2013.

[27] A. G. Norman, R. France, and A. J. Ptak, "Atomic ordering and phase separation in MBE $GaAs_{1-x}Bi_x$," *J. Vac. Sci. Technol., B,* vol. 29, p. 03C121, 2011.

[28] P. Wei, S. Tixier, M. Chicoine, S. Francoeur, A. Mascarenhas, T. Tiedje, and F. Schiettekatte, "Ion beam characterization of $GaAs_{1-x-y}N_xBi_y$ epitaxial layers," *Nuclear Instruments and Methods in Physics Research Section B: Beam Interactions with Materials and Atoms,* vol. 219-220, pp. 671-675, 2004.

[29] A. R. Mohmad, F. Bastiman, C. J. Hunter, R. Richards, S. J. Sweeney, J. S. Ng, and J. P. R. David, "Effects of rapid thermal annealing on $GaAs_{1-x}Bi_x$ alloys," *Appl. Phys. Lett.,* vol. 101, pp. 012106-3, 2012.

[30] A. Janotti, S. Wei, and S. B. Zhang, "Theoretical study of the effects of isovalent coalloying of Bi and N in GaAs," *Phys. Rev. B,* vol. 65, p. 115203, 2002.

[31] C. R. Wie, "High resolution x-ray diffraction characterization of semiconductor structures," *Materials Science and Engineering: R: Reports,* vol. 13, pp. 1-56, 1994.

[32] D.K. Bowen and B.K. Tanner, *High Resolution X-Ray Diffractometry And Topography*: Taylor & Francis, 1998.

[33] I. Kim, B. Choe, S. K. Park, and W. Jeong, "Analysis of abnormal x-ray diffraction peak broadening from InGaAs/GaAs multiple quantum wells," *J. Appl. Phys.*, vol. 82, pp. 4865-4869, 1997.

[34] J. W. Matthews and A. E. Blakeslee, "Defects in epitaxial multilayers: I. Misfit dislocations," *J. Cryst. Growth*, vol. 27, pp. 118-125, 1974.

[35] R. People and J. C. Bean, "Calculation of critical layer thickness versus lattice mismatch for Ge_xSi_{1-x}/Si strained-layer heterostructures," *Appl. Phys. Lett.*, vol. 47, pp. 322-324, 1985.

[36] A. Fischer, H. Kühne, and H. Richter, "New Approach in Equilibrium Theory for Strained Layer Relaxation," *Phys. Rev. Lett.*, vol. 73, pp. 2712-2715, 1994.

[37] C. Hadj Belgacem and M. Fnaiech, "Exact Analytical Solution for the Critical Layer Thickness of a Lattice-Mismatched Heteroepitaxial Layer," *J. Electron. Mater.*, vol. 39, pp. 2248-2250, 2010.

[38] E. A. Fitzgerald, "Dislocations in strained-layer epitaxy: theory, experiment, and applications," *Materials Science Reports*, vol. 7, pp. 87-142, 1991.

[39] M. J. Ekenstedt, S. M. Wang, and T. G. Andersson, "Temperature-dependent critical layer thickness for $In_{0.36}Ga_{0.64}As$/GaAs single quantum wells," *Appl. Phys. Lett.*, vol. 58, pp. 854-855, 1991.

[40] G. J. Whaley and P. I. Cohen, "Relaxation of strained InGaAs during molecular beam epitaxy," *Appl. Phys. Lett.*, vol. 57, pp. 144-146, 1990.

[41] D. J. Dunstan, P. Kidd, R. Beanland, A. Sacedón, E. Calleja, L. González, Y. González, and F. J. Pacheco, "Predictability of plastic relaxation in metamorphic epitaxy," *Mater. Sci. Technol.*, vol. 12, pp. 181-186, 1996.

[42] G. L. Price, "Critical-thickness and growth-mode transitions in highly strained $In_xGa_{1-x}As$ films," *Phys. Rev. Lett.*, vol. 66, pp. 469-472, 1991.

[43] R. France, C. S. Jiang, and A. J. Ptak, "In situ strain relaxation comparison between GaAsBi and GaInAs grown by molecular-beam epitaxy," *Appl. Phys. Lett.*, vol. 98, pp. 101908-3, 2011.

[44] V. Pačebutas, K. Bertulis, L. Dapkus, G. Aleksejenko, A. Krotkus, K. M. Yu, and W. Walukiewicz, "Characterization of low-temperature molecular-beam-epitaxy grown GaBiAs layers," *Semicond. Sci. Technol.*, vol. 22, p. 819, 2007.

[45] G. B. Stringfellow and G. S. Chen, "Atomic ordering in III/V semiconductor alloys," *J. Vac. Sci. Technol., B*, vol. 9, pp. 2182-2188, 1991.

[46] R. S. Irani and R. W. Cahn, "The mechanism of crystallographic ordering in CuPt," *Journal of Materials Science*, vol. 8, pp. 1453-1472, 1973/10/01 1973.

[47] B. A. Philips, A. G. Norman, T. Y. Seong, S. Mahajan, G. R. Booker, M. Skowronski, J. P. Harbison, and V. G. Keramidas, "Mechanism for CuPt-type ordering in mixed III–V epitaxial layers," *J. Cryst. Growth*, vol. 140, pp. 249-263, 1994.

[48] S. H. Wei and A. Zunger, "Band-gap narrowing in ordered and disordered semiconductor alloys," *Appl. Phys. Lett.*, vol. 56, pp. 662-664, 1990.

[49] S. Wei and A. Zunger, "Optical properties of zinc-blende semiconductor alloys: Effects of epitaxial strain and atomic ordering," *Phys. Rev. B*, vol. 49, pp. 14337-14351, 1994.

[50] S. Wei and A. Zunger, "Fingerprints of CuPt ordering in III-V semiconductor alloys: Valence-band splittings, band-gap reduction, and x-ray structure factors," *Phys. Rev. B*, vol. 57, pp. 8983-8988, 1998.

[51] J. E. Bernard, S. Froyen, and A. Zunger, "Spontaneous surface-induced long-range order in $Ga_{0.5}In_{0.5}P$ alloys," *Phys. Rev. B*, vol. 44, pp. 11178-11195, 1991.

[52] A. Duzik, J. C. Thomas, A. van der Ven, and J. M. Millunchick, "Surface reconstruction stability and configurational disorder on Bi-terminated GaAs(001)," *Phys. Rev. B*, vol. 87, p. 035313, 2013.

[53] D. F. Reyes, F. Bastiman, C. J. Hunter, D. L. Sales, A. Sanchez, J. P. R. David, and D. Gonzalez, "Bismuth incorporation and the role of ordering in GaAsBi/GaAs structures," *Nanoscale Research Letters*, vol. 9, p. 23, 2014.

Chapter 5: Electrical and Absorption Characterisation

5.1 Introduction

In this chapter, the electrical characteristics of the diode samples are explored using current-voltage (I-V) and capacitance voltage (C-V) measurements, and the I-V characteristics are compared with those of GaAsBi/GaAs LEDs reported in the literature. I-V measurements were also performed with the sample under illumination from a laser, which gives information about the absorption properties of the samples at a single wavelength. The optical absorption characteristics were also investigated as a function of wavelength and bias. Most of the focus on GaAsBi has been aimed at light-emitting devices such as LEDs and lasers; therefore there is limited information in the literature on its absorption properties, apart from absorption coefficients reported for GaAsBi layers in [1-3].

5.2 Electrical characterisation measurements

5.2.1 Room temperature C-V measurements

Room temperature C-V measurements were performed on all samples. C-V results for STB065 are shown in Figure 5.1. The measurements were taken using a frequency of 1 MHz.

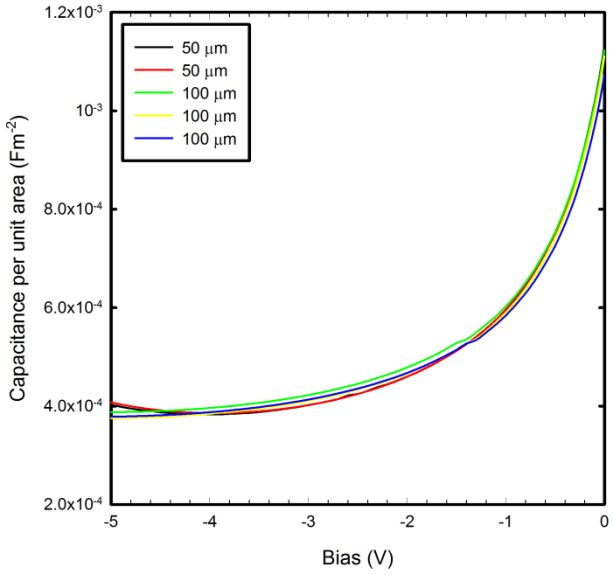

Figure 5.1: Graph of capacitance per unit area versus voltage for STB065.

The C-V characteristics scale with area when a small reduction to the device radii of 1-2 μm is taken into account. For an ideal diode under reverse bias, the dark currents are very low until breakdown is reached, so the diode is assumed to act as a perfect capacitor with a phase angle of 90°. In these samples, the dark currents are high and increase rapidly with reverse bias so that the phase angle deviates from this value. This may affect the validity of the C-V measurements.

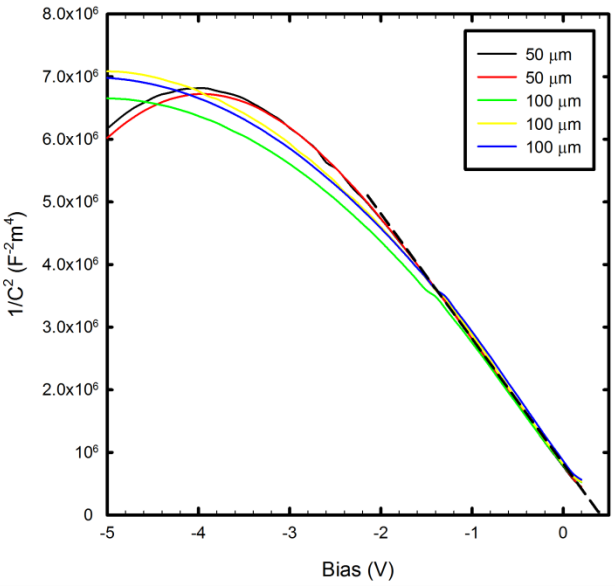

Figure 5.2: Graph of $1/C^2$ versus voltage for STB065.

Plotting $1/C^2$ versus voltage and extrapolating to the x-axis gives a value for the built-in voltage for the diode, which is ~0.4 V.

Assuming the background doping density in the GaAsBi layers is much lower than the doping density in the intentionally doped regions, applying a reverse bias to the diode will mainly deplete the GaAsBi layer. The depletion width is obtained simply from the equation

$$W = \frac{\varepsilon_0 \varepsilon_r}{C_D} \tag{5.1}$$

where ε_r is the relative permittivity of the semiconductor and ε_0 is the permittivity of free space in units of Fm^{-1}. C_D is the capacitance per unit area in units of Fm^{-2}.

The background doping density, *N*, was calculated using the following equations:

$$N = -\frac{2}{q\varepsilon_r\varepsilon_0 A} \tag{5.2}$$

$$A = \frac{d(1/C_D^2)}{dV} \tag{5.3}$$

The relative permittivity of GaAsBi was taken to be the same as that of GaAs (12.9) as no values have been reported in the literature. The relative permittivity increases with atomic number [4] (e.g. along the series GaP, GaAs, GaSb), so it would be expected that the addition of bismuth would cause an increase in the relative permittivity.

Doping profiles obtained from the C-V measurements using equations (5.2) and (5.3) are shown in Figure 5.3. Since the calculations of the depletion width and the background doping both involve the relative permittivity of GaAsBi, there is some uncertainty in the calculated values.

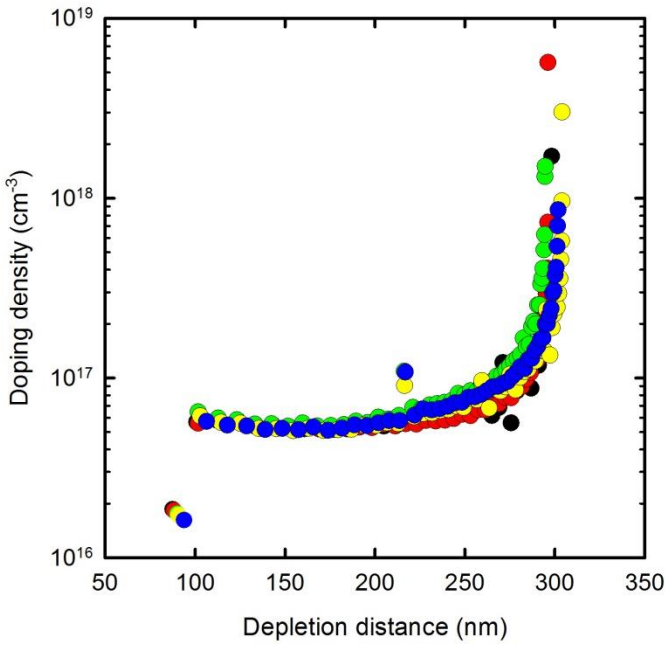

Figure 5.3: Doping profiles for STB065.

The initial depletion width at zero bias is approximately 100 nm, therefore the GaAsBi layer is not fully depleted at zero bias. Full depletion is desirable in order to aid carrier collection. The depletion width achieved can be increased by decreasing the background doping, however this

may be fundamentally limited by the low sample temperatures required for GaAsBi growth. Background doping in the range 10^{14} - 10^{15} cm^{-3} is desirable and such levels have been achieved for InGaAsN with a band gap around 1 eV [5, 6].

As the reverse bias increases, there is a sharp increase in the doping concentration at around 300 nm, which is probably the n/p-doped region. Although the nominal i-region thickness is 370 nm, this is likely reduced by dopant diffusion, as observed in the SIMS doping profiles.

It has not been determined whether the background doping in the GaAsBi layers is n-type or p-type, however nominally undoped GaAsBi layers with p-type conductivity have been reported [7]. In this work, the hole concentration was found to increase with Bi content. Interpolating between doping concentrations for 5.6% and 8.5% gives an expected value of 5×10^{15} cm^{-3} for a Bi content of 6%. Since the background doping is higher in our samples it is likely that factors other than the presence of Bi, such as the outgassing of the As cell during growth and/or background impurities in the growth chamber, are influencing the background doping.

5.2.2 Room temperature forward I-V measurements

Room temperature I-V measurements were initially performed on the STB03 samples. The I-V characteristics did not scale with area and there was variation even between devices with the same radius.

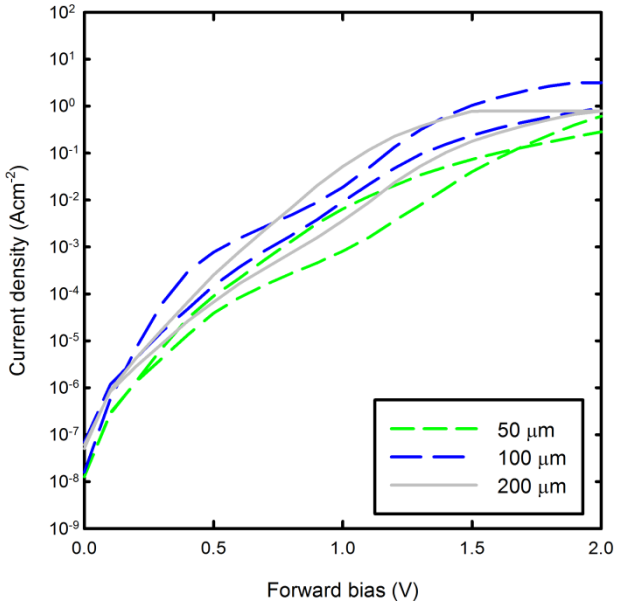

Figure 5.4: Forward J-V characteristics for STB03D.
Device radii are indicated in the legend.

The I-V characteristics for the STB06 samples are more uniform, and since the main difference in the structures is the increased thickness of the p-region, it seems likely that this is the cause of the improvement. The rest of this chapter focuses solely on the STB06 samples.

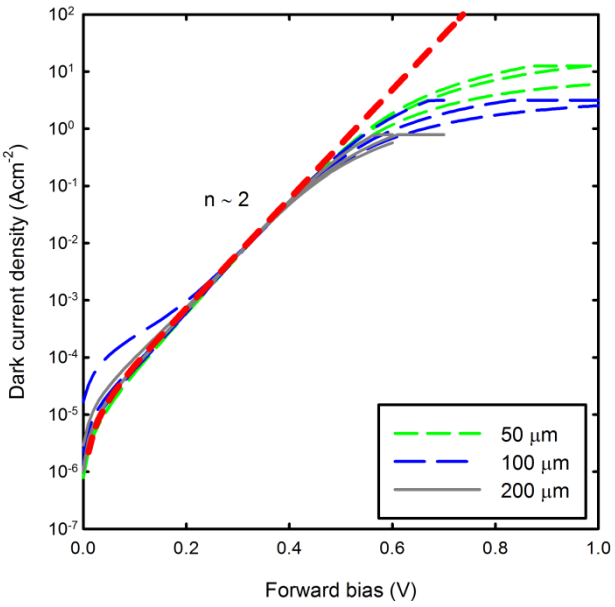

Figure 5.5: Forward J-V characteristics for STB063.
Device radii are indicated in the legend.

Figure 5.5 shows forward bias current density-voltage (J-V) plots for STB063. The overlap of the data shows that the forward currents scale with device area, indicating that bulk current is the dominant current mechanism. This was the same for all bismuth-containing samples.

The slope of the forward J-V curves provides information about the recombination mechanism in the diodes. The ideal diode equation is given by

$$J = J_0 \left[exp\left(\frac{qV}{nkT}\right) - 1 \right] \tag{5.4}$$

where J_0 is the saturation current density, q is the charge on an electron, n is the ideality factor, k is Boltzmann's constant and T is the temperature in Kelvin. Assuming the temperature is constant, the slope of the J-V curve depends on the ideality factor, which takes values between 1 and 2. All the samples in this work have ideality factors close to 2, which indicates that recombination via trap states in the i-region is the dominant current mechanism. The presence of trap states can be expected due to the low growth temperature used for the GaAsBi layers.

The J-V curves deviate from ideal behaviour as the voltage increases. This can be attributed to series resistance within the structure. When a series resistance is present, the diode equation can be rewritten as

$$I = I_0 \left[exp\left(\frac{q(V - IR_s)}{nkT} \right) \right] \tag{5.5}$$

The series resistance term IR_s becomes increasingly dominant as the current increases. This equation can be solved numerically to give a value for the series resistance. For devices from STB063 this varied between 200 and 400 Ohms.

A useful way of comparing electrical properties of the samples is to look at the saturation current density, J_0. The lowest values of the saturation current density for all samples are shown in Figure 5.6.

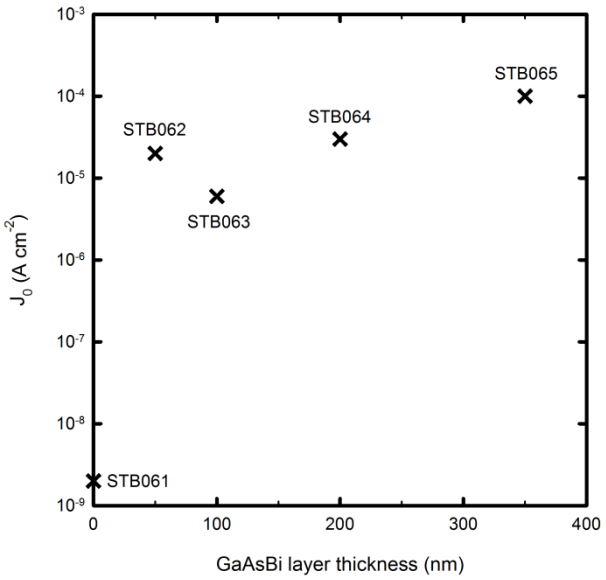

Figure 5.6: Graph showing saturation current density for the STB06 series as a function of GaAsBi layer thickness.

J_0 for the GaAs control sample was 2×10^{-9} A cm^{-2}, whereas the lowest value for a sample containing GaAsBi was 6×10^{-6} A cm^{-2} for sample STB063.

This majority of this increase can be explained by the lower band gap of STB063 (~1.04 eV from absorption measurements presented in section 5.3.2), since J_0 increases with decreasing band gap:

$$J_0 = \frac{qn_i^2 D}{NL} \tag{5.6}$$

$$n_i^2 \propto exp\left(-\frac{E_g}{kT}\right) \tag{5.7}$$

where n_i is the intrinsic carrier concentration, D is the diffusion coefficient and L is the minority carrier diffusion length.

Looking at the expected increase in J_0 from the decrease in band gap (assuming the other terms are constant) gives a predicted J_0 value of 4.4×10^{-7} A cm^{-2} for STB063. The further increase in J_0 could possibly be due to a decrease in the minority carrier diffusion length in GaAsBi compared to GaAs. This could be due to the existence of trap states in the GaAsBi layers, in agreement with the observed ideality factors.

It has been shown that the forward dark current density can be used as a measure of the dislocation density [8]. J_0 increases for the series STB063, STB064, STB065, which is probably due to the increasing number of dislocations present in the GaAsBi layers. The fact that J_0 for STB062 is anomalously high could be linked to the uneven structure of the layer, as observed in the TEM images.

5.2.3 Room temperature reverse I-V measurements

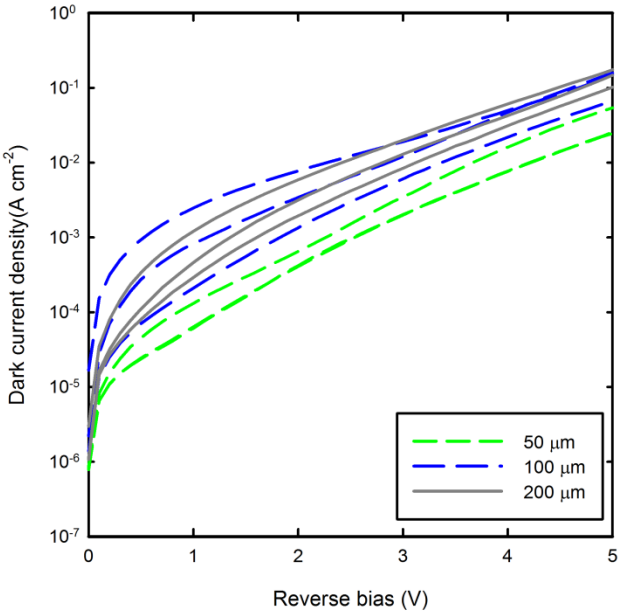

Figure 5.7: Reverse J-V characteristics for STB063.
Device radii are indicated in the legend.

Reverse bias current-voltage characteristics for STB063 are shown in Figure 5.7. The dark currents increase exponentially with voltage, and unlike the forward bias characteristics, do not scale exactly with device area. The exponential dependence can be modelled by a Poole-Frenkel emission process. In this model electrons are emitted from trap centres, and this emission is aided by the presence of an electric field.

The 3D Poole-Frenkel process has the form [9]

$$J \approx \frac{\sigma_0 kT}{2qb}\left[exp\left(\frac{qEb}{kT}\right) - 1\right] \tag{5.8}$$

where σ_0 is the low-field conductivity, b is the radius of the potential well and E is the electric field. It is assumed that all the applied potential is dropped across the i-region, i.e. $E = V/w$ where w is the nominal i-region width. The parameters σ_0 and b are adjusted to fit the data. A fit to the J-V curve of a 50 µm radius device from sample STB063 is shown in Figure 5.8.

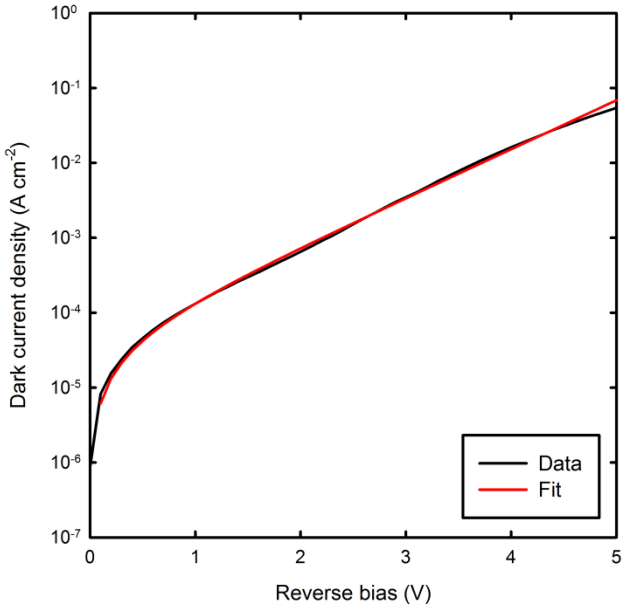

Figure 5.8: Fit to reverse bias J-V data for STB063 using Poole-Frenkel equation.

The fitting parameters used were $\sigma_0 = 1.5 \times 10^{-7}$ S m^{-1} and $b = 5 \times 10^{-9}$ m. The Poole-Frenkel effect has also been suggested as a current mechanism for p-i-n diodes containing InGaAsN layers [10].

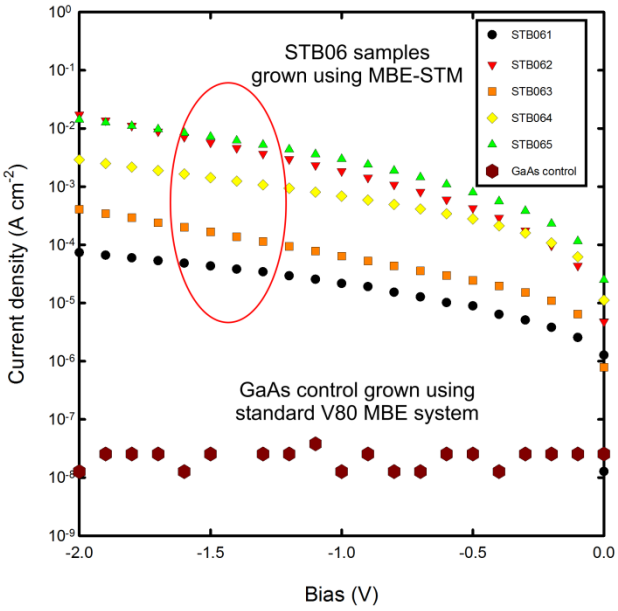

Figure 5.9: Reverse bias current density characteristics for STB06 samples and a GaAs control sample.

The lowest reverse dark current density data for each sample are shown in Figure 5.9. The increase in the reverse dark currents for STB063-5 corresponds to the trend observed for the

forward bias J_0 values. The reverse dark current for STB062 is noticeably high. In addition to the fact that the quality of this layer is likely to be poor, the nominally undoped region in this sample is likely much thinner than the intended 100 nm (50 nm of GaAs + 50 nm GaAsBi), due to dopant diffusion, which results in a much higher electric field for a given bias and hence leads to a higher current.

Also shown is the reverse J-V curve for a GaAs control sample grown on a V80 MBE reactor. The reverse current for this sample is below the noise floor for the picoammeter and is significantly lower than for STB061. Thus it seems likely that some overriding factor in the growth and/or processing has contributed to the high dark currents in the other samples, rather than the presence of the GaAsBi layers.

Although the dark currents for STB062 are higher than expected, they still compare favourably to I-V data for GaAsBi/GaAs LEDs reported by Lewis et al. [11]. The LEDs have the same nominal i-region structure as STB062 (25 nm GaAs, 50 nm GaAsBi, 25 nm GaAs). The I-V data reported in [11] have been converted to J-V data and are shown in Figure 5.10. Sample STB062 has slightly lower reverse dark currents and also a better ideality factor ($n \approx 2$ compared to 2.26 for the LED). It should be noted that this is despite the fact that the bismuth fraction is higher in our samples than the LED (1.8% Bi). The improvement could be due to the higher GaAsBi growth temperature used for our samples (380 °C rather than 300 °C).

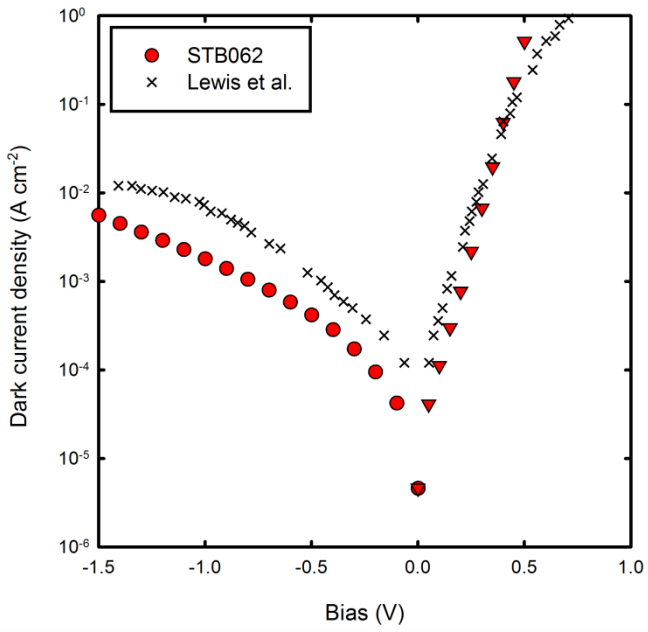

Figure 5.10: Comparison of J-V data for sample STB062 and Lewis et al.

5.2.4 Temperature-dependent I-V data

I-V measurements were also taken at temperatures of 77 K and 200 K. Reverse and forward bias J-V curves for STB063 are shown below.

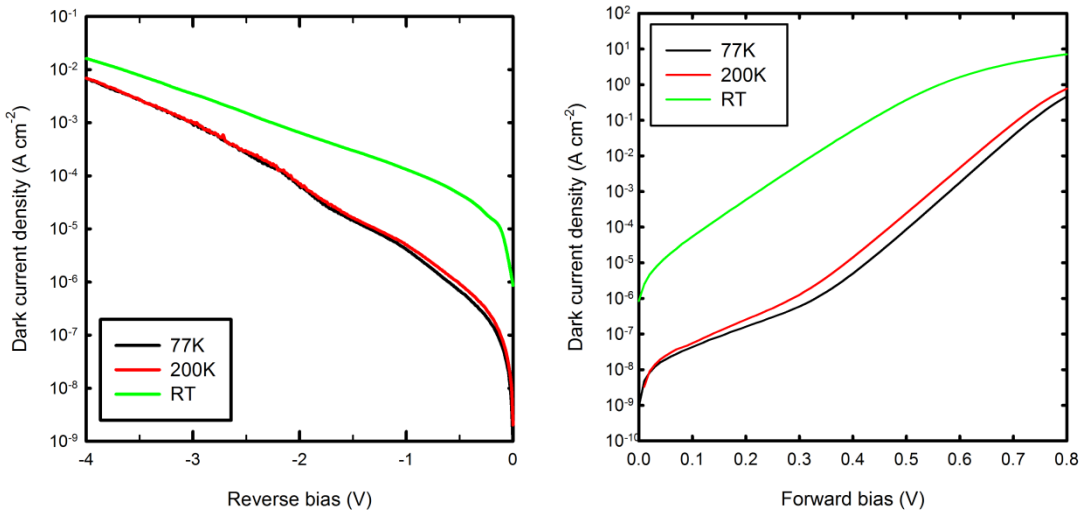

Figure 5.11: Forward and reverse J-V characteristics for STB063 taken at different temperatures.

The forward J-V curves show a decrease in current between room temperature and low temperature which is most likely due to the increase in band gap with decreasing temperature, although there is a small increase between 77 K and 200 K. The reverse J-V curves also show a corresponding decrease from room temperature to low temperature.

5.3 Optical characterisation measurements

5.3.1 Laser illumination measurements

To gain information about the potential of GaAsBi for absorption related applications, forward and reverse I-V curves were taken under illumination from a laser operating at 1064 nm. This wavelength corresponds to photon energy of 1.17 eV, which is less than the band gap of GaAs and therefore leads to photoexcitation in the GaAsBi layers only.

Taking I-V curves under illumination from a light source gives operation in the fourth I-V quadrant (positive bias, negative current). This can give information about the material's potential for use in solar cells. Two important parameters for solar cells are the short-circuit current, I_{sc}, and the open-circuit voltage, V_{oc}.

The short-circuit current is defined as the photocurrent at zero bias. Since the dark current at this bias is zero, this is equal to the total current at zero bias. Under low illumination conditions the short-circuit current is proportional to the light intensity.

The open-circuit voltage is the voltage at which the total current is zero. This obviously depends on both the dark current and the illuminated current. The relationship between them can be derived using the expression for the diode dark current [12]:

$$I = I_{sc} - I_{dark}(V) = I_{sc} - I_0\left(e^{qV/nkT} - 1\right) \tag{5.9}$$

which equals zero at the open-circuit voltage, V_{oc}.

Rearranging for V_{oc} gives

$$V_{oc} = \frac{nkT}{q} ln\left(\frac{I_{sc}}{I_0} + 1\right) \approx \frac{nkT}{q} ln\left(\frac{I_{sc}}{I_0}\right) \tag{5.10}$$

(The "+1" can be ignored when $I_{sc} \gg I_0$).

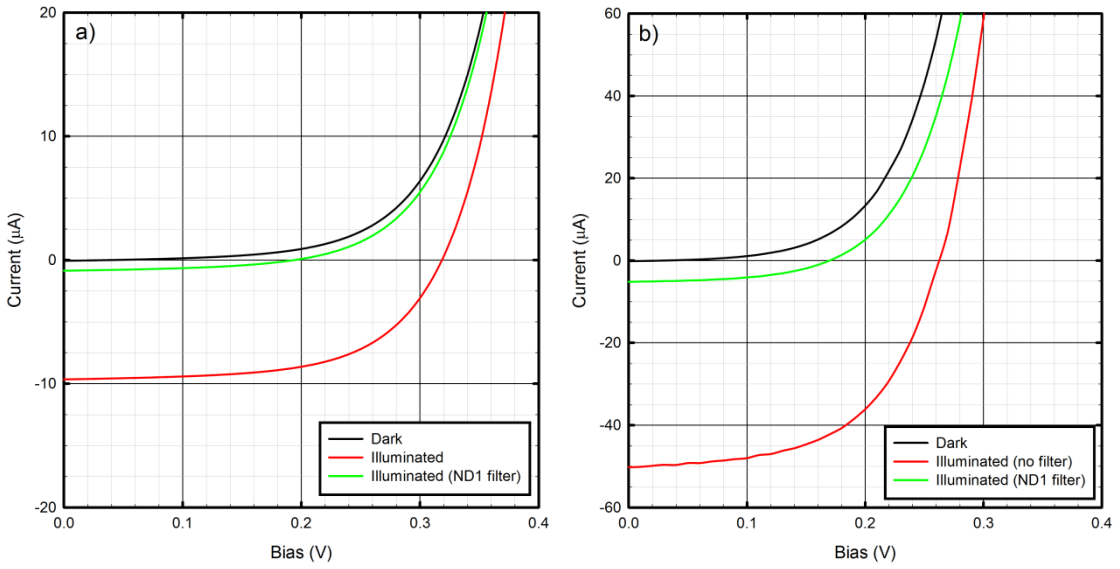

Figure 5.12: Dark and illuminated I-V curves for samples STB062 and STB065.

I-V curves taken in the dark and under laser illumination are shown in Figure 5.12. For some measurements, a neutral density filter was placed in the laser beam path, which reduces the power incident on the device by a factor of approximately 10. Since the short-circuit current also scales by a similar factor, this shows that the photocurrent is proportional to the light intensity.

From Figure 5.12 it can be seen that the short-circuit current increases between STB062 and STB065, which is due to the increased absorption in the thicker GaAsBi layer. However, the open-circuit voltage decreases. Equation (5.10) shows that the open-circuit voltage depends on the ratio of the short-circuit current and the saturation current, and while the short-circuit current increases, this is outweighed by the increase in saturation current.

In reverse bias, the illuminated I-V curves can be used to determine the responsivity of the samples. The responsivity, *R*, is a measure of the detection efficiency of the devices and is defined as

$$R = \frac{I}{P}\ (A/W) \tag{5.11}$$

where *I* is the photocurrent and *P* is the optical power incident on the device. A certain fraction of the incident light is reflected at the sample surface, though this is not usually taken into account when calculating the responsivity.

Another measure of detection efficiency is the external quantum efficiency (E.Q.E.), which is defined as the number of electrons generated in the absorbing layer divided by the number of incident photons. The external quantum efficiency is related to the responsivity by the equation

$$E.Q.E. = \frac{I/q}{P/(hc/\lambda)} = \frac{I}{P}\frac{hc}{\lambda q} = \frac{Rhc}{\lambda q} \tag{5.12}$$

where q is the charge on an electron, h is Planck's constant, c is the speed of light and λ is the wavelength of the incident light.

Assuming every photon can only generate one electron-hole pair, the external quantum efficiency takes values between 0 and 1, or can alternatively be expressed as a percentage. Generating more than one electron-hole pair can occur in zero-dimensional systems however [13, 14], and this effect is of interest for increasing solar cell efficiency.

In order to measure the responsivity of the samples, the incident power from the laser was measured using a commercial InGaAs photodiode with a known responsivity. Reverse bias I-V curves were then taken in the dark and under laser illumination. The photocurrent was obtained by subtracting the dark current from the illuminated current, giving the photocurrent as a function of reverse bias.

Reverse bias characteristics for STB065 are shown in Figure 5.13. For STB062 and STB063, there was no change in the photocurrent as a function of bias. However for STB064 and STB065, there was an increase in the photocurrent between 0 and -2 V. This could be related to the presence of dislocations in the GaAsBi layers in these samples: at zero bias, the built-in field is not sufficient to sweep all the carriers out of trap states; therefore a reverse bias must be applied to extract all the carriers.

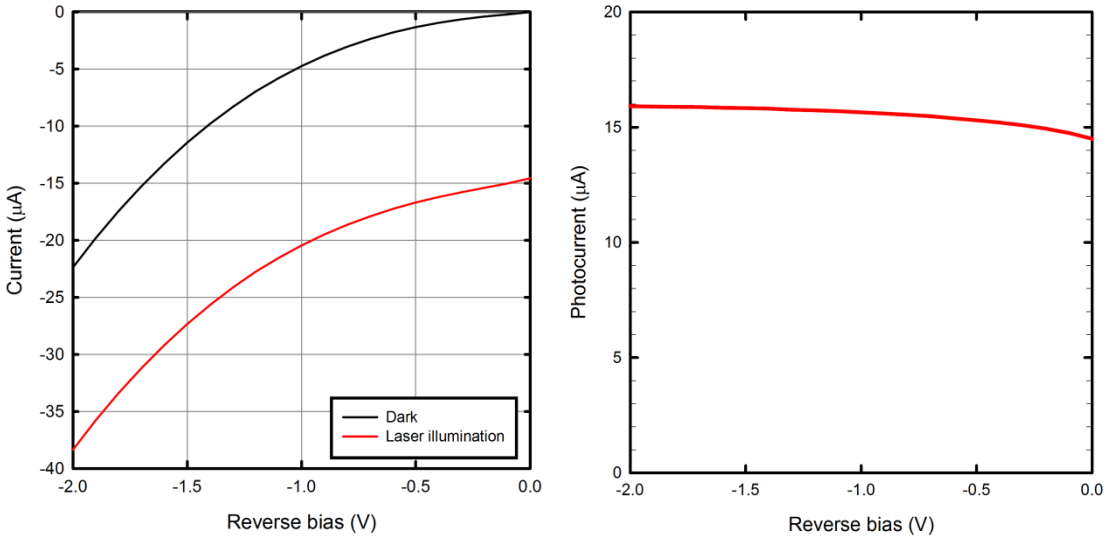

Figure 5.13: Graphs for STB065 showing a) dark and illuminated current and b) photocurrent as a function of reverse bias.

The responsivity values for the samples were calculated using measured values of the incident laser power. The responsivity values at zero bias and a bias of -2 V are plotted as a function of GaAsBi layer thickness in Figure 5.14.

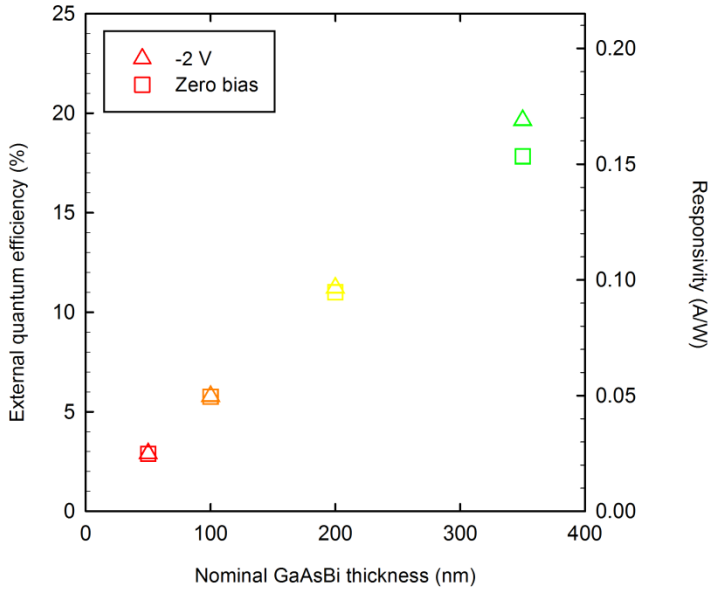

Figure 5.14: External quantum efficiency/responsivity at 1064 nm as a function of GaAsBi layer thickness.

Absorption of light in a uniform medium can be described by the equation

$$I(W) = I_0 exp(-\alpha W) \tag{5.13}$$

where I is the light intensity at a given thickness W, I_0 is the incident intensity and α is the absorption coefficient of the material.

Assuming every absorbed photon creates one electron-hole pair that is extracted from the device, the external quantum efficiency can be related to the absorption by the equation

$$E.Q.E. = (1 - R_p)[1 - \exp(-\alpha W)] \tag{5.14}$$

where R_p is the reflection coefficient of the material. The term (1-R_p) is added to account for the light that is reflected from the sample surface.

For normal incidence ($\theta_i = \theta_t = 90°$) and refraction in air ($n_{air} = 1$), the reflection coefficient is

$$R_p = \left|\frac{n-1}{n+1}\right|^2 \tag{5.15}$$

where n is the refractive index of GaAs. At 1064 nm this is approximately 3.48 [15].

Refractive index values for GaAsBi with Bi fractions up to 2.6% have been reported [16], but the value for [Bi] = 6% is not known. In [16], the refractive index was reported to vary between 3.7 and 3.4. Thus the reflectivity at the GaAs/GaAsBi interface is very small and can be neglected.

Using equation (5.14) a fit to the E.Q.E. data can be obtained, which is shown in Figure 5.15.

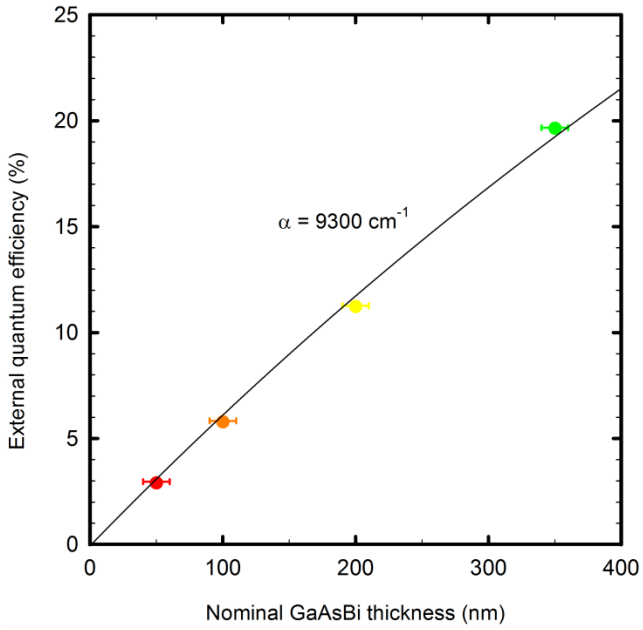

Figure 5.15: External quantum efficiency at 1064 nm as a function of GaAsBi layer thickness.

From SIMS and XRD measurements, the error in the GaAsBi layer thicknesses is no more than 10 nm. Though a good fit to the data points can be obtained using a single value for α, some deviation should be expected as the bismuth contents of the GaAsBi layers are not exactly the same, which leads to variation in α.

In order to compare the absorption coefficient to those of other materials, it is necessary to look at the values at similar energies above the band gap, i.e. ~170 meV above the band gap. GaAs

has an absorption coefficient of ~1.5 × 10^4 cm^{-1} at 1.6 eV [17], and InGaAsN with a 1.2 eV band gap has an absorption coefficient of ~1.3 × 10^4 cm^{-1} at 1.38 eV [18]. It has been suggested that, for alloys described by the BAC model, the absorption coefficient will be reduced compared to that of the host material [19]. In [19] the absorption coefficient of an InGaAsN alloy with 1% N was found to be less than half that of GaAs at the absorption edge.

5.3.2 Photoresponse measurements

The photoresponse of the devices as a function of wavelength was measured using a white light source and a monochromator. The data were normalized for the system response using a germanium photodiode. The data were then normalized to the responsivity value at 1064 nm to obtain the responsivity as a function of wavelength. For STB061, the response was compared to the other samples in order to obtain the responsivity. Measurements were taken at both zero bias and a bias of -2V in order to obtain the maximum photoresponse.

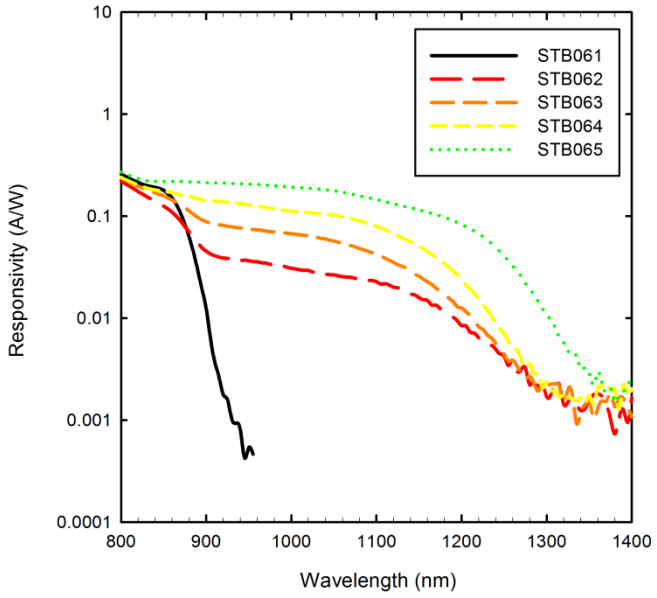

Figure 5.16: Responsivity of all samples at a bias of -2 V.

The responsivity of all the samples is shown in Figure 5.16. As expected, the responsivity of STB061 begins to roll off around 870 nm. For the samples containing GaAsBi layers, the response is extended into the near-infrared, up to ~1.24 μm.

Although we do not possess a solar simulator to perform calibrated measurements, it is possible to obtain an estimate of the short circuit current under the AM 1.5 spectrum from the responsivity data, using the equation

$$J_{sc} = \sum_{\lambda_1}^{\lambda_2} H(\lambda)R(\lambda) \tag{5.16}$$

where H is the spectral irradiance at a particular wavelength λ. In this case the AM 1.5 global spectrum was used, which was shown in Figure 1.3. The sum is carried out between the limits λ_1 and λ_2. Only the absorption in the GaAsBi layers is considered; therefore λ_1 is taken to be 880 nm, so that absorption in the GaAs is discounted. λ_2 is taken to be 1400 nm. The calculated values of J_{sc} are shown in Table 5.1. Also shown are the values of J_0 which were given in Figure 5.6. The values for J_0 and J_{sc} were then used to calculate values for the open-circuit voltage using equation (5.10).

Sample	GaAsBi layer thickness (nm)	J_0 (mA cm^{-2})	J_{sc} (mA cm^{-2})	V_{oc} (V)
STB062	50	0.0200	0.1096	0.0849
STB063	100	0.006	0.2171	0.1643
STB064	200	0.0300	0.3623	0.1168
STB065	350	0.1000	0.5935	0.0880

Table 5.1: Calculated values of short-circuit current and open-circuit voltage under the AM 1.5 global spectrum.

The J_{sc} values display an increasing trend which is expected from the responsivity measurements e.g. in Figure 5.15. However the increase in J_{sc} is cancelled out by the increase in J_0, leading to a decrease in V_{oc} for the samples with thicker GaAsBi layers, which is similar to the behaviour observed for the illuminated I-V curves in Figure 5.12.

Both the J_{sc} and V_{oc} values are low when compared to dilute nitride samples with similar band gaps [20, 21]. An obvious way to increase J_{sc} is to use thicker absorbing layers; however this will increase the number of dislocations. This emphasizes the need for lattice matching using boron or nitrogen, in order to grow thick Bi-containing layers on GaAs/Ge without dislocations. J_{sc} could also be improved by increasing the carrier collection efficiency, which could be achieved by reducing the background doping, as mentioned in section 5.2.1.

Besides increasing J_{sc}, V_{oc} could also be increased by reducing J_0. Since the increase in J_0 values is believed to be related to the increase in the number of dislocations with increasing GaAsBi thickness, this could also be achieved by lattice matching.

5.3.3 Absorption coefficients

The absorption coefficients (α) can be calculated from the responsivity data by equating equations (5.12) and (5.14) and rearranging:

$$\alpha = \left(\frac{-1}{w}\right) ln\left[1 - \frac{Rhc}{(1 - R_p)\lambda q}\right] \tag{5.17}$$

This equation assumes that all of the generated charge carriers are extracted from the samples, which for the thicker GaAsBi layers is only true when an external bias is applied. This equation is only valid for wavelengths > 880 nm (or energies < than 1.4 eV) where carriers are absorbed in the GaAsBi layers only.

The reflection coefficient of GaAs is assumed to be constant. Though it varies over the range of wavelengths used, the difference in the values of absorption coefficients that would be obtained by allowing the reflection coefficient to vary is no more than 5%.

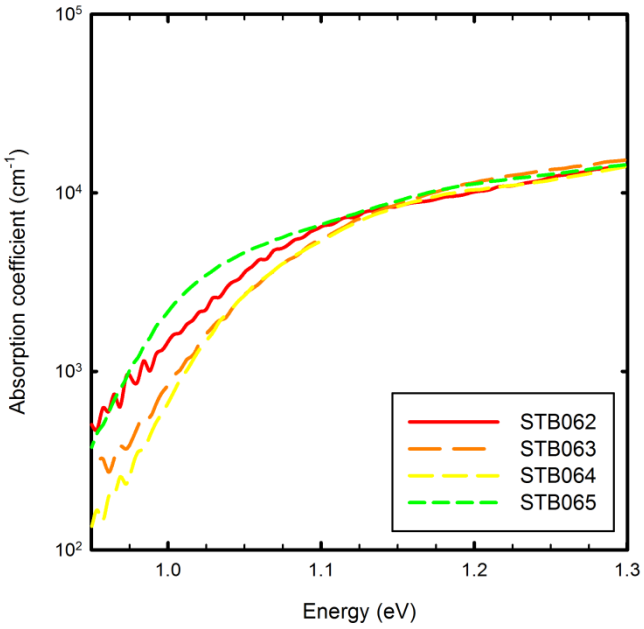

Figure 5.17: Absorption coefficients of the GaAsBi layers as a function of energy.

The absorption coefficients of the GaAsBi layers are shown in Figure 5.17. The absorption coefficient of a direct band gap semiconductor is given by

$$\alpha(h\nu) \propto \left(h\nu - E_g\right)^{1/2} \tag{5.18}$$

where $h\nu$ is the incident photon energy and E_g is the band gap energy. Thus for a direct band gap semiconductor, plotting the square of the absorption coefficient against the photon energy gives a straight line graph. Extrapolating the data to the x-axis gives a value for the band gap of the layer. Graphs of α^2 for all samples are shown in Figure 5.18.

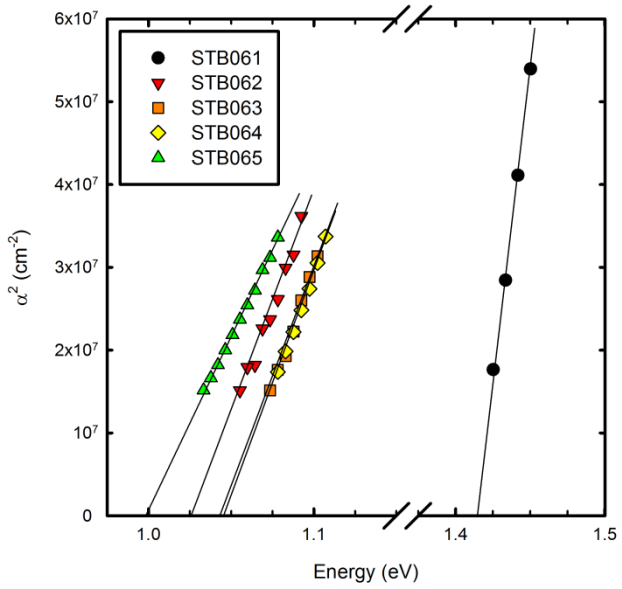

Figure 5.18: Graphs of α^2 versus energy for all samples.

All of the graphs are linear, confirming that for this Bi content GaAsBi is a direct band gap material, which is in agreement with the results in [2]. The range of band gaps observed is probably due to small variations in the bismuth composition and/or strain in the GaAsBi layers.

For sample STB063, the band gap value obtained from the absorption data was 1.04 eV. From XRD, the Bi content for this layer is approximately 6%. Using the BAC model presented in the introduction (Equation (1.6)), the expected band gap for this Bi content is 1.046 eV. There is thus good agreement between these values.

In Figure 5.17, for energies less than the band gap energy, the absorption coefficients decrease exponentially with decreasing photon energy. This feature has been observed for both amorphous and crystalline materials and was first observed by Urbach [22].

The "Urbach tail" can be described by the equation [23]

$$\alpha(h\upsilon) = \alpha_g \exp\left[\frac{(h\upsilon - E_g)}{E_0}\right] \tag{5.19}$$

where $h\upsilon$ is the photon energy, E_g is the band gap energy and E_0 is the characteristic width of the absorption edge. α_g is the value of the absorption coefficient at the band gap. The fit to the data for STB063 is shown in Figure 5.19.

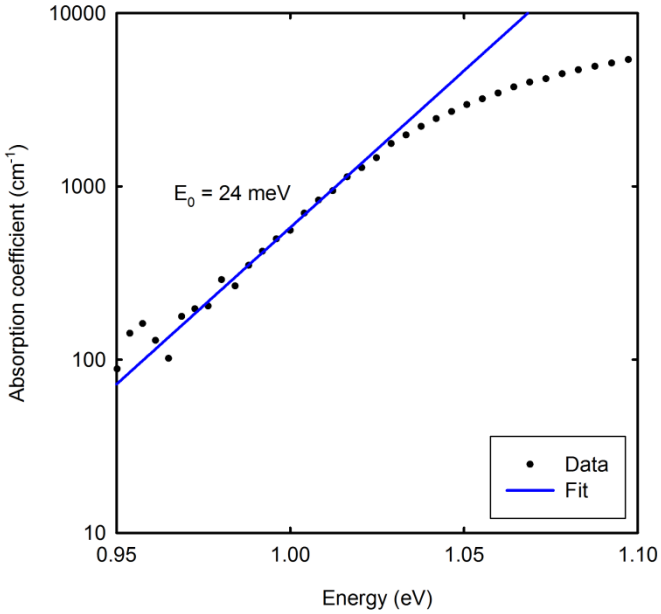

Figure 5.19: Graph showing the Urbach tail for STB063.

The parameter E_0 is composed of temperature-dependent contributions (phonon interaction) and temperature-independent contributions due to structural disorder and impurities. The E_0 values were obtained from the zero bias data, as at -2 V the external electric field will also lead to increased absorption below the band gap. This is known as the Franz-Keldysh effect [24] and will be discussed in more detail in section 5.3.4. This effect will still be present at zero bias due to the built-in field in the diodes, so the E_0 values should considered an upper bound to the true values.

The exponential regions of the absorption coefficient data were fitted using equation (5.19), and the E_0 values for all samples are shown in Table 5.2.

Sample	E_0 (meV)
STB061	14
STB062	24
STB063	24
STB064	21
STB065	22

Table 5.2: E_0 values for all samples.

For STB061, it was assumed that most of the low-energy photons are transmitted through the p and i regions, so that most of the absorption will take place in the n-doped GaAs. E_0 was found to be 14 meV, slightly more than the value of 13 meV found in [23] for Si-doped GaAs. The increase in E_0 in GaAsBi compared to GaAs is likely due to the increased disorder and the presence of Bi clusters which give states within the band gap [25]. Although the presence of ordering was evident from the TED patterns, it is unlikely that the ordering exists throughout the entire layer, and thus there will be some disordered regions present.

This absorption below the band gap is consistent with emission below the band gap observed in electro- and photo-luminescence studies [11, 26, 27]. A study of Urbach tailing in GaAsBi photoluminescence spectra was recently reported and evidence of two different energy scales was found [28]. At room temperature both values were around 29 meV, which is fairly close to our values.

E_0 has been reported to increase with carrier concentration for values above 10^{18} cm^{-3}, however the carrier concentration necessary to give an E_0 value of 24 meV is close to 10^{20} cm^{-3} [29], so it is unlikely that this increase is related to the background doping in the samples.

5.3.4 Franz-Keldysh effect and electro-absorption

As mentioned previously, absorption below the band gap is enhanced by the presence of an electric field, since the field effectively reduces the barrier, *d*, that an electron in the valence band has to tunnel through to reach the conduction band. This is illustrated in Figure 5.20. This is similar to the Poole-Frenkel effect, except the transfer is from the valence band instead of a trap centre. This effect allows the absorption in this region to be controlled by the magnitude of the electric field, and is of interest for electroabsorption modulators [30, 31].

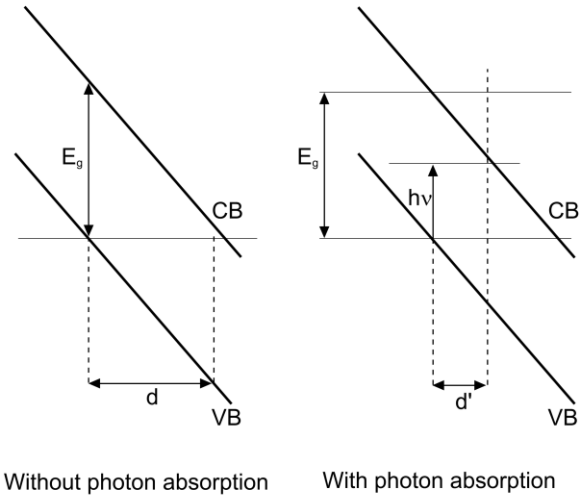

Figure 5.20: Diagrams illustrating electron tunnelling with and without photon absorption.

To investigate this effect, photoresponse measurements were performed as a function of bias and converted to absorption coefficient data using equation (5.17). STB065 has the greatest absorption due to its thick GaAsBi layer; however there is also the change in carrier collection with bias to consider. Instead STB064 was used, where there is only a small change in carrier collection with bias. The absorption coefficients at voltages from zero to -5 V are shown in Figure 5.21.

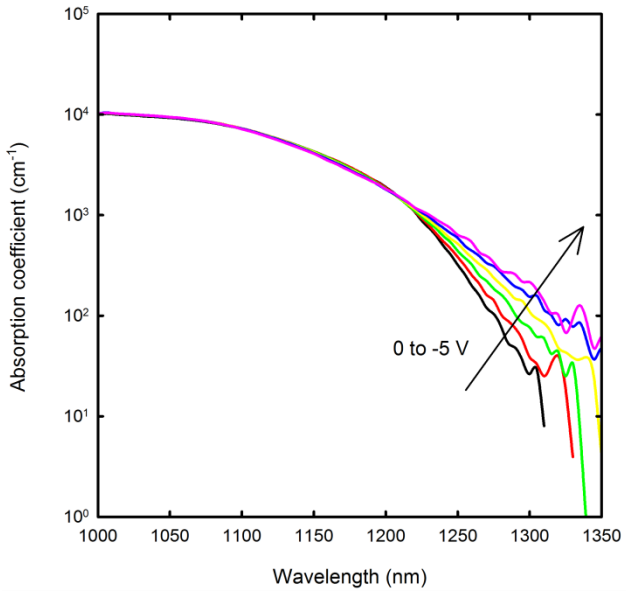

Figure 5.21: Absorption coefficients for STB064 measured at different reverse biases.

The results in Figure 5.21 show that the absorption at 1.31 μm can be varied with applied bias. This wavelength is technologically important for telecommunications, as the dispersion in an optical fibre at this wavelength is zero [32]. The change in absorption coefficient for different biases is plotted as a function of wavelength in Figure 5.22.

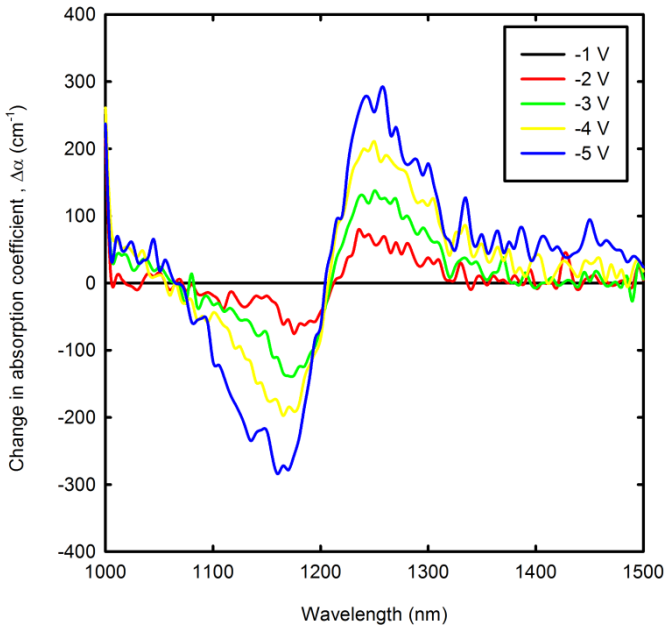

Figure 5.22: Change in absorption coefficient as a function of reverse bias, compared to the value at -1 V.

These results show that GaAsBi has the potential to be used for electroabsorption modulators operating at 1.31 μm.

5.4 Summary

C-V measurements performed on the diode samples showed that the background doping in the GaAsBi layers is on the order of 10^{16} cm^{-3}. This is relatively high and needs to be improved in order to achieve a fully-depleted layer at zero bias, which is desirable for solar cells.

The I-V characteristics of the samples exhibit ideality factors close to 2, which indicate recombination via trap states in the GaAsBi layers. The presence of such states could be related to the low growth temperature used. The increase in saturation current density compared to GaAs is higher than that expected from the reduction of the band gap alone and possibly indicates a degradation of the carrier lifetimes in the GaAsBi layers, which could also be linked to the presence of trap states. The saturation current density increases with the GaAsBi layer thickness and this is likely due to the increase in the number of dislocations. The reverse dark currents are high and increase exponentially with reverse bias, however since this is also the case for the GaAs control sample it is likely that the GaAsBi layers are not causing this behaviour. Though high, the dark currents are still better than those previously reported in the literature for similar samples.

Measurements taken with a laser operating at 1064 nm show that the GaAsBi layers can detect light at this wavelength, and the detection efficiency increases with layer thickness. For the thicker layers, the fact that a reverse bias is needed to extract all the carriers again suggests the presence of trap states in the layers.

Measurements of the photoresponse as a function of wavelength show that the GaAsBi samples are able to detect light out to at least 1.24 μm. The absorption coefficients obtained from these measurements are slightly lower than for GaAs, which could be due to the reduced coupling between the valence and conduction bands in the BAC model. The band gaps obtained from the absorption coefficients are consistent with a bismuth content of ~6% Bi. The increased Urbach tailing observed below the band gap compared to GaAs is indicative of increased disorder/Bi clustering in the GaAsBi layers. The absorption below the band gap also increases with reverse bias which is attributed to the Franz-Keldysh effect. The ability to adjust the absorption coefficient by changing the applied electric field is desirable for electro-adsorption modulators.

5.5 References

[1] K. Bertulis, A. Krotkus, G. Aleksejenko, V. Pacebutas, R. Adomavicius, G. Molis, and S. Marcinkevicius, "GaBiAs: A material for optoelectronic terahertz devices," *Appl. Phys. Lett.*, vol. 88, pp. 201112-3, 2006.

[2] V. Pačebutas, K. Bertulis, G. Aleksejenko, R. Adomavicius, G. Molis, and A. Krotkus, "Growth and characterization of GaBiAs epilayers," *Opt. Mater.*, vol. 30, pp. 756-758, 2008.

[3] M. Henini, J. Ibanez, M. Schmidbauer, M. Shafi, S. V. Novikov, L. Turyanska, S. I. Molina, D. L. Sales, M. F. Chisholm, and J. Misiewicz, "Molecular beam epitaxy of GaBiAs on (311)B GaAs substrates," *Appl. Phys. Lett.*, vol. 91, pp. 251909-3, 2007.

[4] S. Adachi, "Material parameters of $In_{1-x}Ga_xAs_yP_{1-y}$ and related binaries," *J. Appl. Phys.*, vol. 53, pp. 8775-8792, 1982.

[5] I. R. Sellers, W. S. Tan, K. Smith, S. Hooper, S. Day, and M. Kauer, "Wide depletion width of 1 eV GaInNAs solar cells by thermal annealing," *Appl. Phys. Lett.*, vol. 99, pp. 151111-3, 2011.

[6] J. S. Ng, W. M. Soong, M. J. Steer, M. Hopkinson, J. P. R. David, J. Chamings, S. J. Sweeney, and A. R. Adams, "Long wavelength bulk GaInNAs p-i -n photodiodes lattice matched to GaAs," *J. Appl. Phys.*, vol. 101, pp. 064506-6, 2007.

[7] G. Pettinari, A. Patane, A. Polimeni, M. Capizzi, X. Lu, and T. Tiedje, "Bi-induced p-type conductivity in nominally undoped Ga(AsBi)," *Appl. Phys. Lett.*, vol. 100, pp. 092109-4, 2012.

[8] J. P. R. David, Y. H. Chen, R. Grey, G. Hill, P. N. Robson, and P. Kightley, "Effect of misfit dislocations on leakage currents in strained multiquantum well structures," *Appl. Phys. Lett.*, vol. 67, pp. 906-908, 1995.

[9] J. L. Hartke, "The Three-Dimensional Poole-Frenkel Effect," *J. Appl. Phys.*, vol. 39, pp. 4871-4873, 1968.

[10] L. J. J. Tan, W. M. Soong, J. P. R. David, and J. S. Ng, "Dark Current Mechanism in Bulk GaInNAs Lattice Matched to GaAs," *Electron Devices, IEEE Transactions on*, vol. 58, pp. 103-106, 2011.

[11] R. B. Lewis, D. A. Beaton, X. Lu, and T. Tiedje, "$GaAs_{1-x}Bi_x$ light emitting diodes," *J. Cryst. Growth*, vol. 311, pp. 1872-1875, 2009.

[12] J. Nelson, *The Physics of Solar Cells*: Imperial College Press, 2003.

[13] M. C. Beard, K. P. Knutsen, P. Yu, J. M. Luther, Q. Song, W. K. Metzger, R. J. Ellingson, and A. J. Nozik, "Multiple Exciton Generation in Colloidal Silicon Nanocrystals," *Nano Lett.*, vol. 7, pp. 2506-2512, 2007.

[14] A. J. Nozik, "Multiple exciton generation in semiconductor quantum dots," *Chem. Phys. Lett.*, vol. 457, pp. 3-11, 2008.

[15] D. T. F. Marple, "Refractive Index of GaAs," *J. Appl. Phys.*, vol. 35, pp. 1241-1242, 1964.

[16] K. Yamashita, M. Yoshimoto, and K. Oe, "Temperature-insensitive refractive index of GaAsBi alloy for laser diode in WDM optical communication," *phys. stat. sol. (c)*, vol. 3, pp. 693-696, 2006.

[17] H. C. Casey, D. D. Sell, and K. W. Wecht, "Concentration dependence of the absorption coefficient for n-type and p-type GaAs between 1.3 and 1.6 eV," *J. Appl. Phys.*, vol. 46, pp. 250-257, 1975.

[18] P. Perlin, P. Wisniewski, C. Skierbiszewski, T. Suski, E. Kaminska, S. G. Subramanya, E. R. Weber, D. E. Mars, and W. Walukiewicz, "Interband optical absorption in free standing layer of $Ga_{0.96}In_{0.04}As_{0.99}N_{0.01}$," *Appl. Phys. Lett.*, vol. 76, pp. 1279-1281, 2000.

[19] C. Skierbiszewski, P. Perlin, P. Wisniewski, T. Suski, J. F. Geisz, K. Hingerl, W. Jantsch, D. E. Mars, and W. Walukiewicz, "Band structure and optical properties of $In_yGa_{1-y}As_{1-x}N_x$ alloys," *Phys. Rev. B*, vol. 65, p. 035207, 2001.

[20] D. B. Jackrel, S. R. Bank, H. B. Yuen, M. A. Wistey, J. S. Harris, A. J. Ptak, S. W. Johnston, D. J. Friedman, and S. R. Kurtz, "Dilute nitride GaInNAs and GaInNAsSb solar cells by molecular beam epitaxy," *J. Appl. Phys.*, vol. 101, pp. 114916-8, 2007.

[21] S. L. Tan, W. M. Soong, M. J. Steer, S. Zhang, J. S. Ng, and J. P. R. David, "Dilute nitride GaInNAs and GaInNAsSb for solar cell applications," in *Proc. SPIE 8256, Physics, Simulation, and Photonic Engineering of Photovoltaic Devices*, 2012, p. 82561E.

[22] F. Urbach, "The Long-Wavelength Edge of Photographic Sensitivity and of the Electronic Absorption of Solids," *Phys. Rev.*, vol. 92, p. 1324, 1953.

[23] S. R. Johnson and T. Tiedje, "Temperature dependence of the Urbach edge in GaAs," *J. Appl. Phys.*, vol. 78, pp. 5609-5613, 1995.

[24] J. I. Pankove, *Optical processes in semiconductors*. Englewood Cliffs: Prentice-Hall, Inc., 1971.

[25] S. Imhof, A. Thranhardt, A. Chernikov, M. Koch, N. S. Koster, K. Kolata, S. Chatterjee, S. W. Koch, X. Lu, S. R. Johnson, D. A. Beaton, T. Tiedje, and O. Rubel, "Clustering effects in Ga(AsBi)," *Appl. Phys. Lett.*, vol. 96, pp. 131115-3, 2010.

[26] S. Francoeur, S. Tixier, E. Young, T. Tiedje, and A. Mascarenhas, "Bi isoelectronic impurities in GaAs," *Phys. Rev. B*, vol. 77, p. 085209, 2008.

[27] A. R. Mohmad, F. Bastiman, J. S. Ng, S. J. Sweeney, and J. P. R. David, "Photoluminescence investigation of high quality $GaAs_{1-x}Bi_x$ on GaAs," *Appl. Phys. Lett.*, vol. 98, p. 122107, 2011.

[28] C. Gogineni, N. A. Riordan, S. R. Johnson, X. Lu, and T. Tiedje, "Disorder and the Urbach edge in dilute bismide GaAsBi," *Appl. Phys. Lett.*, vol. 103, pp. 041110-4, 2013.

[29] J. I. Pankove, "Absorption Edge of Impure Gallium Arsenide," *Phys. Rev.*, vol. 140, p. A2059, 1965.

[30] G. E. Stillman, C. M. Wolfe, C. O. Bozler, and J. A. Rossi, "Electroabsorption in GaAs and its application to waveguide detectors and modulators," *Appl. Phys. Lett.*, vol. 28, pp. 544-546, 1976.

[31] G. B. Morrison, J. W. Raring, C. S. Wang, E. J. Skogen, Y. Chang, M. Sysak, and L. A. Coldren, "Electroabsorption modulator performance predicted from band-edge absorption spectra of bulk, quantum-well, and quantum-well-intermixed InGaAsP structures," *Solid-State Electronics*, vol. 51, pp. 38-47, 2007.

[32] K. A. Jones, *Introduction to Optical Electronics*: John Wiley & Sons, 1987.

Chapter 6: Electroluminescence Characterisation

6.1 Introduction

Photoluminescence is a commonly used technique to determine the Bi content and optical quality of GaAsBi. Previous work by this group has looked at photoluminescence from GaAsBi samples as a function of temperature and laser power. A brief review of the work is given here.

PL intensity is an indication of material quality, since brighter PL indicates less non-radiative recombination and thus fewer defects in the material. The dependence of the PL intensity on the bismuth content has been investigated in [1]. In this work it was found that the room-temperature PL intensity increases with bismuth concentration, up to [Bi] = 6%. In explaining this result it must be first be noted that as the band gap decreases, the confinement of charge carriers in the GaAsBi layer will increase, leading to increased emission from the GaAsBi. When measurements are performed at low temperature it can be assumed that the carriers are confined for all bismuth concentrations, and thus the effect of material quality can be determined. In [1] it was found that the low-temperature PL intensity increased for low bismuth concentrations up to [Bi] = 2%. This was explained by low amounts of bismuth improving the material quality, but leading to defects at higher concentrations.

The temperature dependence of the PL peak has also been investigated. For many III-V semiconductors, the temperature dependence of the band gap is given by the Varshni equation [2]:

$$E_g(T) = E_0 - \frac{\alpha T^2}{(T + \beta)} \tag{6.1}$$

where E_0 is the band gap at 0 K and α and β are fitting parameters. The band gap dependence of GaAsBi however deviates from this equation at low temperatures and displays 'S-shape' behaviour [3].

In this case, the peak dependence can be described by a modified form of the Varshni equation [4]:

$$E_g(T) = E_0 - \frac{\alpha T^2}{(T+\beta)} - \frac{\sigma^2}{kT} \tag{6.2}$$

where σ is an additional fitting parameter. This behaviour has been attributed to localized states in the GaAsBi alloy which trap excitons at low temperatures, leading to emission at energies below the band gap energy.

The effect of rapid thermal annealing (RTA) on GaAsBi samples has been explored in [5]. Annealing was found to improve the optical quality of the samples, without affecting the peak wavelength. This was attributed to the removal of Ga- and As-related defects.

Though most reports of luminescence from GaAsBi in the literature deal with photoluminescence, electroluminescence from GaAsBi/GaAs LEDs has been reported [6]. In this work, electroluminescence from the GaAsBi layer was observed at a wavelength of 987 nm.

6.2 Room temperature electroluminescence

Electroluminescence measurements were initially performed at room temperature and emission was obtained from all samples. Spectra are shown in Figure 6.1. All measurements in this chapter were performed on 200 μm radius devices.

The luminescence from STB065 was noticeably weaker than the other samples, which is probably due to the defects within the GaAsBi layer as observed in the TEM images. It might be expected that STB062 would give the most intense luminescence since it has the thinnest GaAsBi layer; however it is not as bright as STB063, again suggesting increased non-radiative recombination. This is in agreement with the J_0 values reported in the previous chapter, where J_0 is greater for STB062 than STB063.

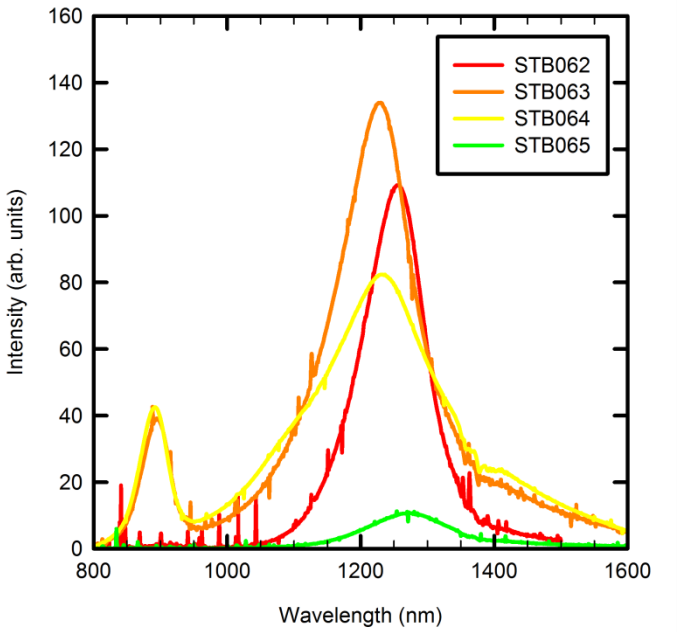

Figure 6.1: Comparison of electroluminescence spectra taken using an injection current of 100 mA.

The FWHM values for the electroluminescence peaks are shown in Table 6.1.

Sample	FWHM (meV)
STB062	88
STB063	118
STB064	187
STB065	116

Table 6.1: FWHM values for all samples (at 100 mA injection current).

These values are much larger than the value expected from the thermal energy alone (around 21 meV). A comparison of FWHM values reported in the literature in [3] shows a range between 50 meV and 220 meV. These large values are attributed to alloy fluctuations in the material.

The FWHM has been observed to increase with decreasing growth temperatures; however in this work, all the samples were grown at the same temperature. Therefore the increased values for the other samples could be due to increased alloy fluctuations with increasing GaAsBi layer

thickness. Also, the presence of relaxation in STB064 and STB065 can be expected to lead to broadening, in common with the broadening observed in the XRD spectra.

The band gaps of the GaAsBi layers were obtained from the EL peaks and are compared with the band gaps determined from photocurrent measurements (presented in chapter 5). The results are shown in Figure 6.2. Using band gap values from the lowest injection current measurements negates the redshift effect of sample heating and gives a better agreement between the band gap values. The biggest discrepancy (for STB062) is still less than 5%. Due to the weak emission from sample STB065, 100 mA was the lowest injection current used.

The rest of this chapter focuses on STB063 and STB064, since STB062 is an anomalous sample due to the poor growth, and the emission from STB065 is very weak.

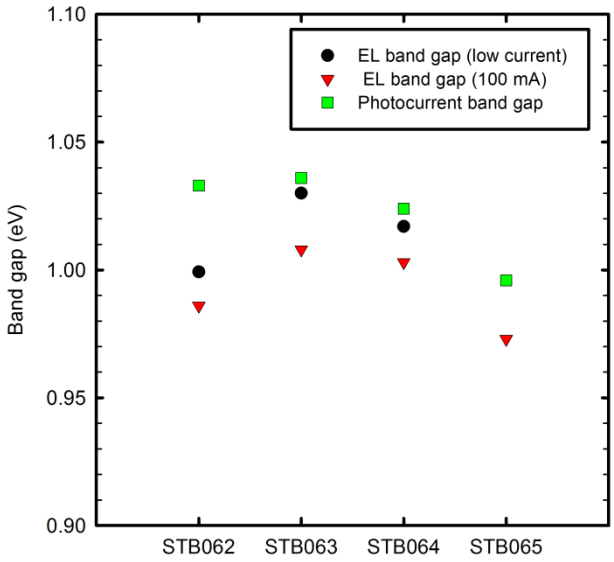

Figure 6.2: Comparison of band gap values obtained from photocurrent and electroluminescence measurements.

Spectra for samples STB063 and STB064 measured at a range of injection currents are shown in Figure 6.3. For both samples, a slight redshift of the GaAsBi peak is observed at high injection currents, which is likely due to sample heating. This can be expected from the series resistance observed in the I-V characteristics.

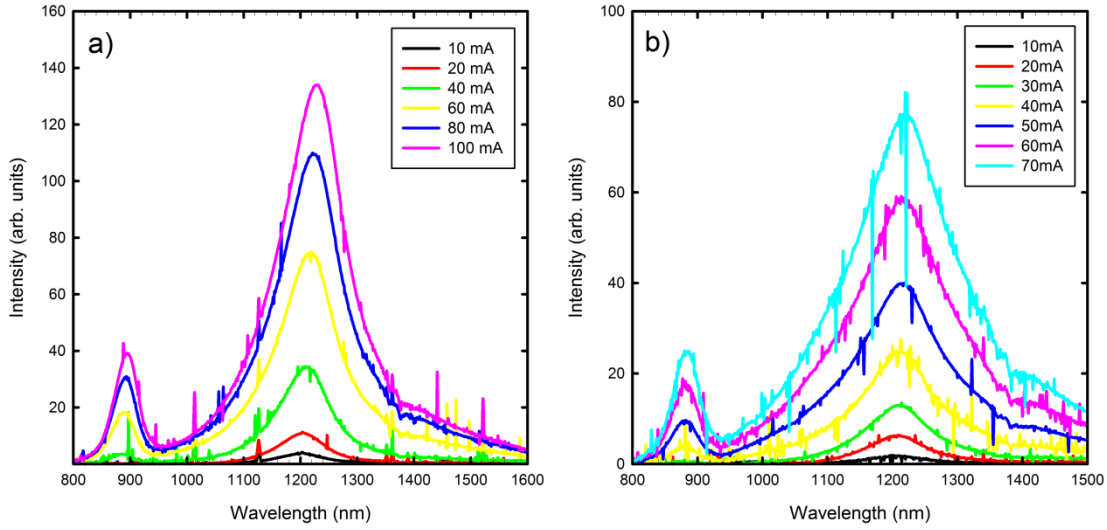

Figure 6.3: RT EL spectra of STB063 (a) and STB064 (b) taken using different injection currents.

Also noticeable in some of the EL spectra is a peak at approximately 880 nm which is probably emission from the GaAs barriers. The redshift compared to the expected room-temperature wavelength of GaAs (~873 nm) could be due to a doping-induced band gap reduction, particularly in the p-type cap where the doping concentration was observed to be very high. Emission around this wavelength was also observed in the electroluminescence spectra of the LEDs in [6], and pressure dependent measurements performed on similar samples [7] also showed the presence of carrier leakage into the GaAs barriers. Since the conduction band offset for GaAsBi/GaAs at 300 K has been predicted to be ~50 meV [8], it is possible that at room temperature electrons can thermally escape from the GaAsBi layer into the barriers.

6.3 Low temperature electroluminescence

EL measurements were also carried out at a low temperature of 20 K, again using a range of injection currents. Low-temperature spectra for samples STB063 and STB064 measured at a range of injection currents are shown in Figure 6.4. The spectra have an asymmetric shape, and the peaks blue-shift with increasing injection current. This behaviour can be explained by the presence of disorder and Bi clustering, which give localized states within the band gap [9]. At low temperatures, holes fall into these states and do not have sufficient thermal energy to escape, leading to the formation of localized excitons. The energy of the luminescence peak is thus less than the band gap energy. As the carrier density (in this case the injection current)

increases, the localized states become filled and the luminescence peak shifts to higher energies [3, 9, 10]. This is illustrated diagrammatically in Figure 6.5.

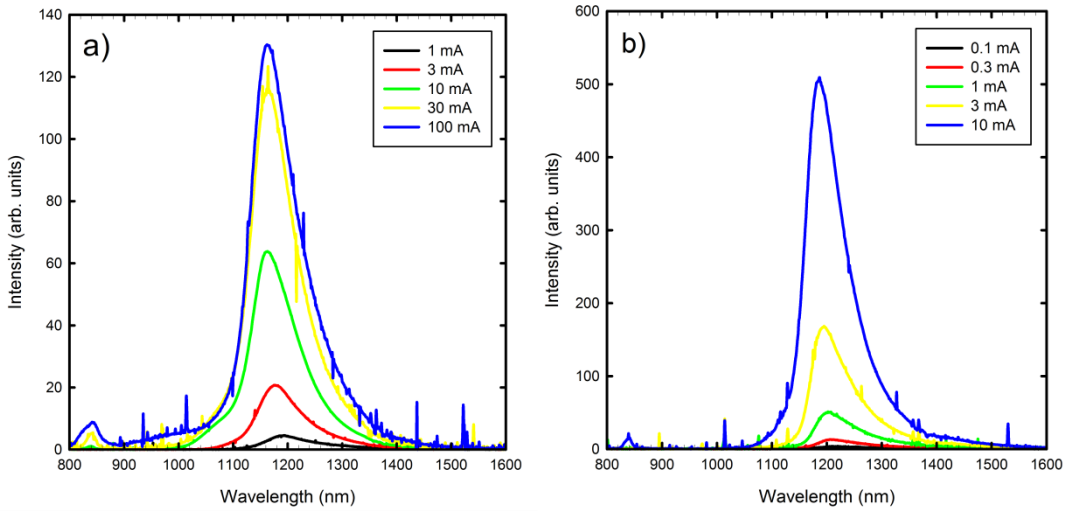

Figure 6.4: Low temperature spectra for STB063 (a) and STB064 (b).

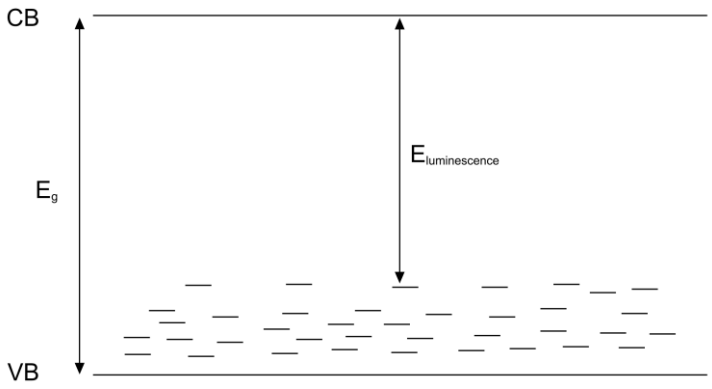

Figure 6.5: Diagram showing localized states in GaAsBi.

Integrating the electroluminescence over the wavelength range used and plotting the resulting values as a function of current gives information about the carrier recombination mechanisms in the GaAsBi layers. Following the analysis used in [11], when the integrated electroluminescence (IEL) is plotted against i_{inject} on a log-log plot, the gradient is expected to take values between 1 and 2, where a value of 1 shows radiative recombination is dominant and a value of 2 shows non-radiative recombination is dominant. An intermediate value shows that both processes are contributing.

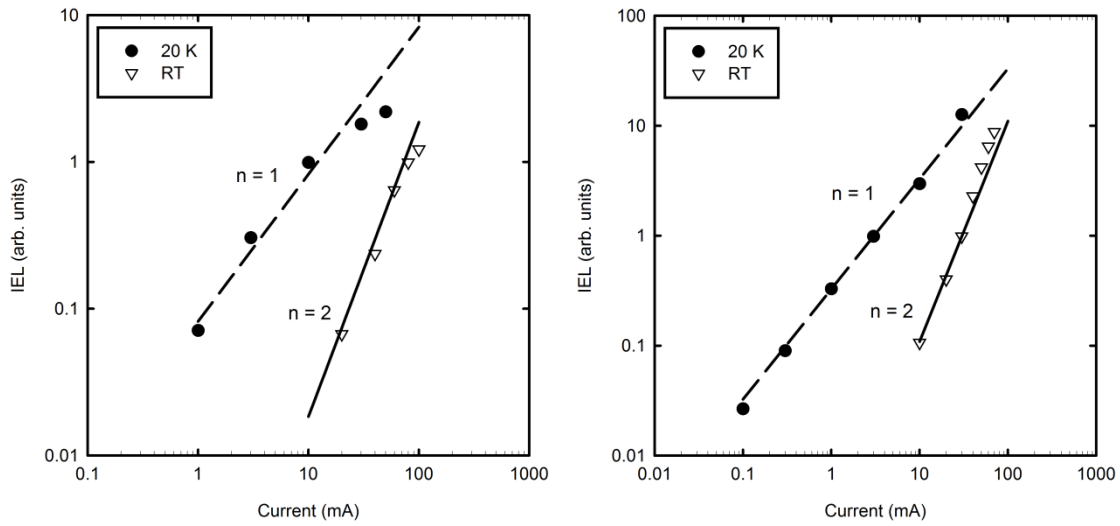

Figure 6.6: IEL plots for STB063 (left) and STB064 (right).

The results are shown in Figure 6.6. The gradients are approximately 1 at 20 K and 2 at room temperature, although for STB063, the IEL values fall below the expected values at high currents. This could be due to the sample heating at high currents causing a temperature-activated quenching mechanism.

These results show that radiative recombination is dominant at low temperature, but non-radiative recombination is dominant at room temperature. Similar behaviour was observed for photoluminescence from GaAsBi layers with [Bi] = 3% [3]. This is due to the change in carrier mobility with temperature: as the temperature increases, carriers become more mobile and are increasingly able to recombine non-radiatively via defect states.

The origin of these defect states is not fully understood, but is likely to be due to two types of defects. First, there will be defects related to the presence of Bi. A common example is the Bi antisite defect, Bi_{Ga}. These were shown to be present in Bi-doped GaAs grown by liquid phase epitaxy [12], although no evidence of these was found in GaAsBi layers grown by MBE [13]. In addition to these defects, there will be native GaAs defects such as As-interstitials, As-antisites and Ga vacancies which are commonly observed in GaAs grown at low temperatures [14], as mentioned in chapter 4. Experiments on n-type GaAs and GaAsBi layers grown at by MBE at temperatures < 400 °C found that these native GaAs defects were dominant in both types of layers [15]. If this is generally the case, reducing the concentration of such defects may prove difficult since GaAsBi growth always requires low growth temperatures. This has implications for using Bi-containing alloys in solar cells, as non-radiative recombination will act as a loss mechanism and reduce the efficiency.

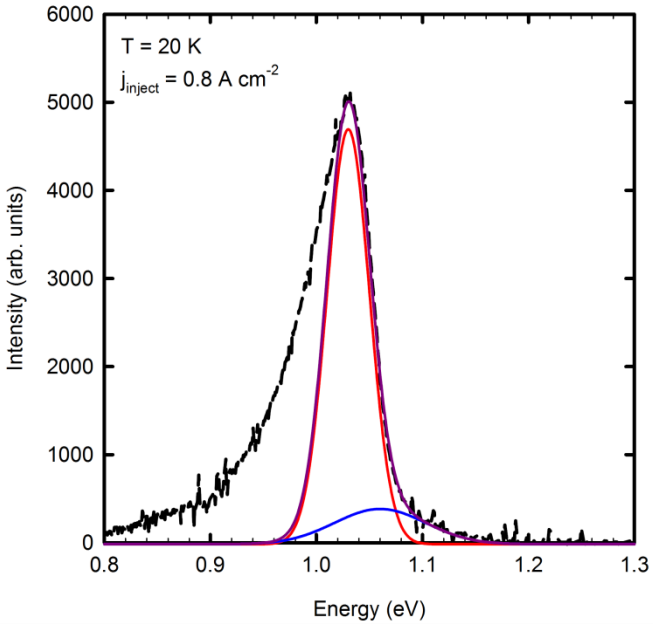

Figure 6.7: Low temperature electroluminescence spectrum of STB064.
Also shown is a fit to the spectrum using a combination of two Gaussian peaks.

The shape of the low temperature spectrum for STB064 will now be discussed in detail. The spectrum taken at an injection current of 1 mA is shown in Figure 6.7. The overall shape of the low temperature spectrum is a convolution of three main features: a low-energy exponential tail for energies lower than 1.03 eV and two Gaussian peaks - a main peak at 1.03 eV and a secondary peak at 1.06 eV. The dip in intensity around 0.9 eV is due to atmospheric water absorption. The overall peak position is 1.031 eV, very close to the main Gaussian peak. Low energy tails in luminescence spectra have been observed for GaAsBi [16, 17], and also for other disordered materials such as (In)GaAsN [18]. They are attributed to recombination of excitons trapped in localized states within the band gap, which is in agreement with the blue-shift in peak with increasing injection current.

Multiple photoluminescence peaks for GaAsBi have also been observed, in bulk [19], single quantum well [17] and double quantum well [20] structures. One possible reason for multiple luminescence peaks is the presence of more than one bismuth composition within the GaAsBi layer. In [20] it was found that the quantum wells grown after the first wells contained more bismuth than the first wells, giving a second PL peak which was redshifted compared to that from the first well. It is possible that a similar effect could occur for growth of bulk layers. In [16], the two peaks seen in the low-temperature photoluminescence spectra were attributed to excitons bound to localized states and free excitons, with the free exciton peak becoming increasingly dominant at higher excitation powers as the localized states become saturated.

From the SIMS and TEM results shown in chapter 4, the Bi content is reasonably uniform throughout the bulk-like parts of the GaAsBi layer. However since the Bi content in the spacers is lower than that in the bulk-like sections this may give rise to an additional peak. The TED measurements also suggested the presence of CuPt-type ordering in the GaAsBi layers. Aside from a structural analysis paper [21], there is very little information in the literature on this effect in the GaAsBi system, and its effect on the optical properties of GaAsBi has not been discussed. It is known that ordering reduces the band gap, therefore if emission from an ordered phase is present, it will be the lower energy peak [22, 23]. Ordering also reduces the peak linewidth [24], and since the lower energy peak has a smaller FWHM this is consistent with our results. As mentioned in chapter 4, it is possible that CuPt ordering occurs at the beginning of growth with a later transition to a disordered phase. This would give two regions with similar Bi content but different band gaps.

At high injection currents, a peak is observed at around 1.48 eV, which suggests that emission from the GaAs barriers is still present even at low temperatures. Though the GaAs peaks observed in the room-temperature EL spectra could be attributed to thermal escape of electrons into the GaAs barriers, at 20 K the conduction band offset will increase (it has been predicted to be at least 90 meV at 0 K [25]) and is thus much greater than the thermal energy. A possible reason for the persistence of the GaAs emission can be understood by looking at the Bi concentration profile from the TEM data, shown in Figure 6.8.

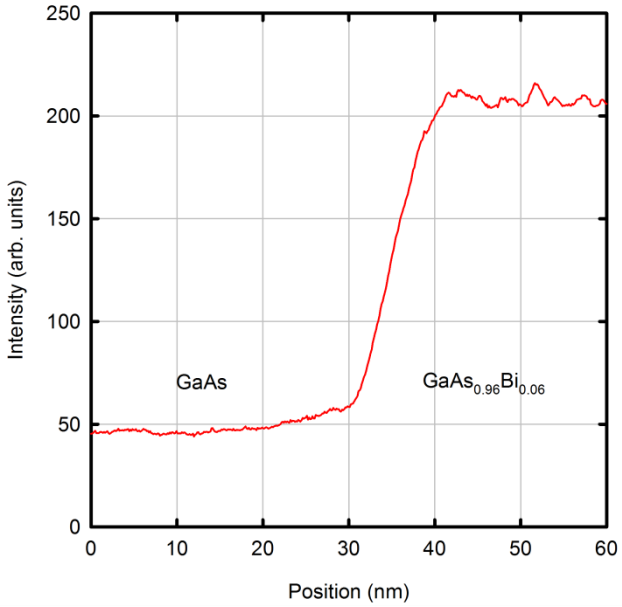

Figure 6.8: Bi concentration profile for STB064 at the GaAs/GaAsBi interface.

As shown in chapter 4, the Bi incorporation in process does not start immediately when growth begins. Thus instead of a ‘step-like’ profile, the bismuth content increases from zero to ~6%

over the first 10-15 nm of growth. In this case the conduction band energy will decrease gradually between the GaAs and GaAsBi instead of being a step-like function, which could allow electrons to escape into the GaAs barriers more easily.

6.4 Temperature dependence

Temperature dependent EL measurements were performed and the results are shown in Figure 6.9. As mentioned in the introduction, photoluminescence of GaAsBi samples been observed to follow an 'S-shaped' dependence [3, 10], due to the presence of localized states in the band gap. This 'S-shape' can be explained with reference to the localized states [26]. At low temperatures, all the excitons are localized and are unable to move between states. As the temperature increases, the excitons gain enough energy to move to lower energy localized states, giving a redshift in the peak energy. As the temperature increases further, the excitons are able to move to increasingly higher energy states, leading to a blueshift in the peak energy. Eventually the thermal energy becomes sufficient for the excitons to become fully delocalized and recombine at the band edges. Beyond this point, the luminescence is mainly from the band edges and the further redshift in peak energy is due to the classical change in band gap as expected from the lattice expansion with temperature.

For both STB063 and STB064 the main peak appears to follow an S-shaped dependence. This is in contrast to the EL results in [6] where the GaAsBi peak was observed to follow the conventional Varshni equation. Due to the presence of the additional peaks (which are also shifting with temperature) it is difficult to be sure of the true peak position in order to determine the Varshni shift. To take into account the existence of multiple peaks in the spectra, the main peak position was obtained from fitting the spectra with Gaussian peaks as in Figure 6.7. This analysis was performed for STB063.

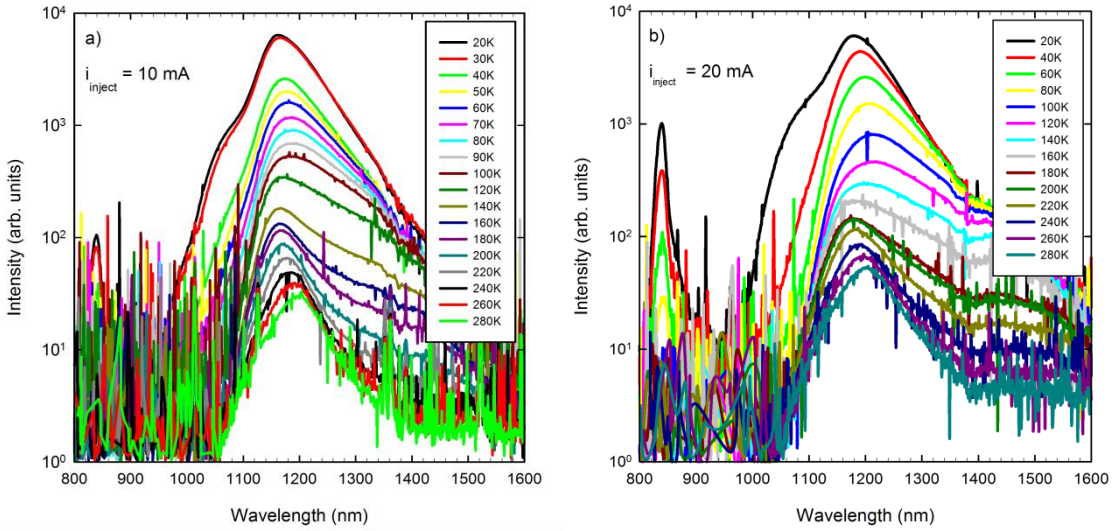

Figure 6.9: Temperature dependent EL spectra for STB063 (a) and STB064 (b).

The peak shift for STB063 as a function of temperature is shown in Figure 6.10. Fits to the data obtained using the forms of the Varshni equation with and without the localization term (equations (6.2) and (6.1)) are also shown.

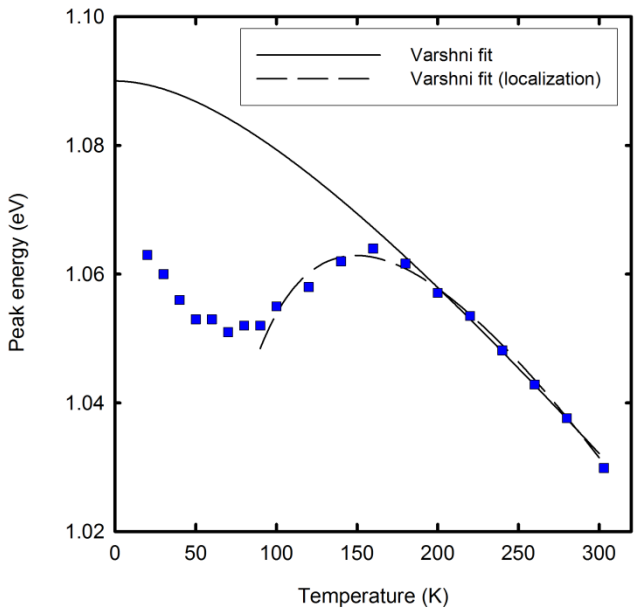

Figure 6.10: Varshni shift data for STB063.

The fitting parameters used for Equation (6.2) are shown in Table 6.2, and are compared to values found in [3] for a GaAsBi sample with ~3% Bi.

Parameter	STB063	Ref. [3]
E_0 (eV)	1.141	1.325
α (meV/K)	0.48	0.49
β (K)	204	120
σ (meV)	24.8	22.5

Table 6.2: Fitting parameters used for STB063, and a comparison with the values used in [3].

The lower E_0 value for STB063 is expected due to its higher Bi content. The α values are similar and are both less than the value reported for a GaAs control sample in [3] (0.56 meV/K). This confirms that incorporating Bi reduces the temperature dependence of the band gap. The localization values are also similar. The clusters that cause the localization are believed to adversely affect the hole mobility [27] and this may cause problems for hole transport in Bi-containing alloys.

As well as the temperature dependence of the EL peak, it is possible to analyse the temperature dependence of the IEL. IEL data often takes an 'Arrhenius' type dependence of the form

$$IEL(T) = Aexp\left(\frac{\Delta E}{kT}\right) \tag{6.3}$$

where A is a constant, ΔE is an activation energy, k is Boltzmann's constant and T is the temperature in Kelvin. Taking the natural log of both sides of the equation gives

$$ln\big(IEL(T)\big) = lnA + \left(\frac{\Delta E}{k}\right)\left(\frac{1}{T}\right) \tag{6.4}$$

Thus, plotting the natural log of the IEL data as a function of $1/T$ gives a straight-line region with gradient $\Delta E/k$ when equation (6.3) is obeyed. Plots of IEL versus inverse temperature are shown in Figure 6.11.

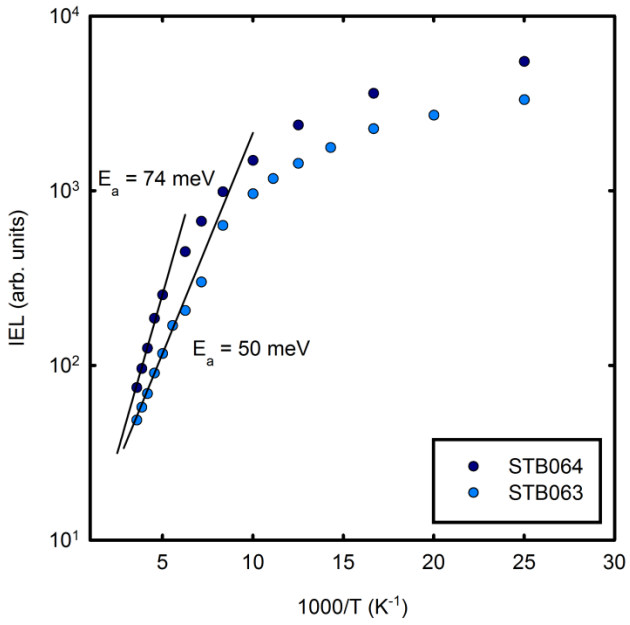

Figure 6.11: Arrhenius plots for STB063 and STB064.

The activation energies obtained from these plots are 50 meV for STB063 and 74 meV for STB064. In [9], temperature dependent PL measurements on GaAsBi layers were modelled using Monte-Carlo simulations and two different energy scales were used to take into account alloy fluctuations and Bi clustering. These were found to be 45 meV and 11 meV respectively. In [10] temperature dependent PL measurements were performed on GaAsBi layers with different Bi contents and doping concentrations, and for an undoped GaAsBi sample with 2.6% Bi, the activation energy was found to be 52 meV. This energy was attributed to localized states lying up to 52 meV in energy from the valence band edge. In our results, the temperature range where the Arhhenius-type behaviour begins (120-160 K) is the same as the range where the peaks blueshift before redshifting, i.e. when the excitons are becoming delocalized. This suggests that the localization could be causing this behaviour, though it is unclear why the activation energy value for STB064 is much greater than for STB063.

6.5 Summary

Room temperature electroluminescence was obtained for all samples at wavelengths around 1.25 µm, despite the presence of dislocations in the thicker GaAsBi layers. The band gaps obtained from the room-temperature EL peaks showed good agreement with the values obtained from photocurrent measurements. Analysis of the IEL as a function of injection current showed that recombination is mainly non-radiative at room temperature and radiative at low temperature.

Emission from the GaAs barriers was observed at both room temperature and low temperature. This suggests that carriers are able to escape from the GaAsBi layer, which could be due to a gradation in Bi content close to the interface, as well as thermal escape at room temperature.

Localized states are present in the GaAsBi layers, as evidenced by the blue-shift of the EL peaks at low temperatures, the exponential tails observed in the low temperature EL spectra and the 'S-shaped' temperature dependence of the EL peaks.

IEL plots were fitted with the Arrhenius equation at temperatures > 120 K, and the activation energies thus obtained are similar to values in the literature which were attributed to excitons escaping from localized states.

6.6 References

[1] A. R. Mohmad, F. Bastiman, C. J. Hunter, J. S. Ng, S. J. Sweeney, and J. P. R. David, "The effect of Bi composition to the optical quality of $GaAs_{1-x}Bi_x$," *Appl. Phys. Lett.*, vol. 99, p. 042107, 2011.

[2] Y. P. Varshni, "Temperature dependence of the energy gap in semiconductors," *Physica*, vol. 34, pp. 149-154, 1967.

[3] A. R. Mohmad, F. Bastiman, J. S. Ng, S. J. Sweeney, and J. P. R. David, "Photoluminescence investigation of high quality $GaAs_{1-x}Bi_x$ on GaAs," *Appl. Phys. Lett.*, vol. 98, p. 122107, 2011.

[4] P. G. Eliseev, P. Perlin, J. Lee, and M. Osinski, "``Blue" temperature-induced shift and band-tail emission in InGaN-based light sources," *Appl. Phys. Lett.*, vol. 71, pp. 569-571, 1997.

[5] A. R. Mohmad, F. Bastiman, C. J. Hunter, R. Richards, S. J. Sweeney, J. S. Ng, and J. P. R. David, "Effects of rapid thermal annealing on $GaAs_{1-x}Bi_x$ alloys," *Appl. Phys. Lett.*, vol. 101, pp. 012106-3, 2012.

[6] R. B. Lewis, D. A. Beaton, X. Lu, and T. Tiedje, "$GaAs_{1-x}Bi_x$ light emitting diodes," *J. Cryst. Growth*, vol. 311, pp. 1872-1875, 2009.

[7] N. Hossain, I. P. Marko, S. R. Jin, K. Hild, S. J. Sweeney, R. B. Lewis, D. A. Beaton, and T. Tiedje, "Recombination mechanisms and band alignment of $GaAs_{1-x}Bi_x$/GaAs light emitting diodes," *Appl. Phys. Lett.*, vol. 100, pp. 051105-3, 2012.

[8] S. J. Sweeney and S. R. Jin, "Bismide-nitride alloys: Promising for efficient light emitting devices in the near- and mid-infrared," *J. Appl. Phys.*, vol. 113, pp. 043110-6, 2013.

[9] S. Imhof, A. Thranhardt, A. Chernikov, M. Koch, N. S. Koster, K. Kolata, S. Chatterjee, S. W. Koch, X. Lu, S. R. Johnson, D. A. Beaton, T. Tiedje, and O. Rubel, "Clustering effects in Ga(AsBi)," *Appl. Phys. Lett.*, vol. 96, pp. 131115-3, 2010.

[10] M. Yoshimoto, M. Itoh, Y. Tominaga, and K. Oe, "Quantitative estimation of density of Bi-induced localized states in $GaAs_{1-x}Bi_x$ grown by molecular beam epitaxy," *J. Cryst. Growth*, 2013.

[11] N. F. Hasbullah, Ng Jo Shien, Liu Hui-Yun, M. Hopkinson, J. David, T. J. Badcock, and D. J. Mowbray, "Dependence of the Electroluminescence on the Spacer Layer Growth Temperature of Multilayer Quantum-Dot Laser Structures," *IEEE Journal of Quantum Electronics*, vol. 45, pp. 79-85, 2009.

[12] M. Kunzer, W. Jost, U. Kaufmann, H. M. Hobgood, and R. N. Thomas, "Identification of the Bi_{Ga} heteroantisite defect in GaAs:Bi," *Phys. Rev. B*, vol. 48, p. 4437, 1993.

[13] G. Ciatto, P. Alippi, A. A. Bonapasta, and T. Tiedje, "How much room for Bi_{Ga} heteroantisites in $GaAs_{1-x}Bi_x$?," *Appl. Phys. Lett.*, vol. 99, pp. 141912-3, 2011.

[14] M. Kaminska, Z. Liliental-Weber, E. R. Weber, T. George, J. B. Kortright, F. W. Smith, B. Y. Tsaur, and A. R. Calawa, "Structural properties of As-rich GaAs grown by molecular beam epitaxy at low temperatures," *Appl. Phys. Lett.*, vol. 54, pp. 1881-1883, 1989.

[15] P. M. Mooney, K. P. Watkins, Z. Jiang, A. F. Basile, R. B. Lewis, V. Bahrami-Yekta, M. Masnadi-Shirazi, D. A. Beaton, and T. Tiedje, "Deep level defects in n-type GaAsBi and GaAs grown at low temperatures," *J. Appl. Phys.*, vol. 113, pp. 133708-6, 2013.

[16] Y. I. Mazur, V. G. Dorogan, M. Benamara, M. E. Ware, M. Schmidbauer, G. G. Tarasov, S. R. Johnson, X. Lu, S. Yu, T. Tiedje, and G. J. Salamo, "Effects of spatial confinement and layer disorder in photoluminescence of $GaAs_{1-x}Bi_x$/GaAs heterostructures," *Journal of Physics D: Applied Physics*, vol. 46, p. 065306, 2013.

[17] Y. I. Mazur, V. G. Dorogan, M. Schmidbauer, G. G. Tarasov, S. R. Johnson, X. Lu, M. E. Ware, S. Q. Yu, T. Tiedje, and G. J. Salamo, "Strong excitation intensity

dependence of the photoluminescence line shape in $GaAs_{1-x}Bi_x$ single quantum well samples," *J. Appl. Phys.,* vol. 113, pp. 144308-5, 2013.

[18] I. A. Buyanova, W. M. Chen, G. Pozina, P. N. Hai, B. Monemar, H. P. Xin, and C. W. Tu, "Optical properties of GaNAs/GaAs structures," *Materials Science and Engineering: B,* vol. 82, pp. 143-147, 2001.

[19] V. Pačebutas, R. Butkutė, B. Čechavičius, J. Kavaliauskas, and A. Krotkus, "Photoluminescence investigation of $GaAs_{1-x}Bi_x$/GaAs heterostructures," *Thin Solid Films,* 2012.

[20] D. Fan, P. C. Grant, S. Yu, V. G. Dorogan, X. Hu, Z. Zeng, C. Li, M. E. Hawkridge, M. Benamara, Y. I. Mazur, G. J. Salamo, S. R. Johnson, and Z. M. Wang, "MBE grown GaAsBi/GaAs double quantum well separate confinement heterostructures," *J. Vac. Sci. Technol., B,* vol. 31, pp. 03C105-5, 2013.

[21] A. G. Norman, R. France, and A. J. Ptak, "Atomic ordering and phase separation in MBE $GaAs_{1-x}Bi_x$," *J. Vac. Sci. Technol., B,* vol. 29, p. 03C121, 2011.

[22] S. Wei and A. Zunger, "Optical properties of zinc-blende semiconductor alloys: Effects of epitaxial strain and atomic ordering," *Phys. Rev. B,* vol. 49, pp. 14337-14351, 1994.

[23] S. Wei and A. Zunger, "Fingerprints of CuPt ordering in III-V semiconductor alloys: Valence-band splittings, band-gap reduction, and x-ray structure factors," *Phys. Rev. B,* vol. 57, pp. 8983-8988, 1998.

[24] Y. Zhang, A. Mascarenhas, S. Smith, J. F. Geisz, J. M. Olson, and M. Hanna, "Effects of spontaneous ordering and alloy statistical fluctuations on exciton linewidth in $Ga_xIn_{1-x}P$ alloys," *Phys. Rev. B,* vol. 61, p. 9910, 2000.

[25] M. Usman, C. A. Broderick, Z. Batool, K. Hild, T. J. C. Hosea, S. J. Sweeney, and E. P. O'Reilly, "Impact of alloy disorder on the band structure of compressively strained $GaBi_xAs_{1-x}$," *Phys. Rev. B,* vol. 87, p. 115104, 2013.

[26] R. J. Potter and N. Balkan, "Optical properties of GaNAs and GaInAsN quantum wells," *Journal of Physics: Condensed Matter,* vol. 16, p. S3387, 2004.

[27] D. A. Beaton, R. B. Lewis, M. Masnadi-Shirazi, and T. Tiedje, "Temperature dependence of hole mobility in $GaAs_{1-x}Bi_x$ alloys," *J. Appl. Phys.,* vol. 108, pp. 083708-4, 2010.

Chapter 7: Conclusions and Future Work

7.1 Conclusions

Bulk GaAsBi layers grown within p-i-n diode structures have been studied. The growth of the layers has been described and the layers have been characterized structurally. The samples have been fabricated into devices which have been characterized optically and electrically.

A growth interrupt method has been outlined which allows growth of thick GaAsBi layers at higher growth temperatures than those commonly used in the literature. Dislocations have been observed by TEM imaging, and the presence of relaxation is evidenced in XRD measurements. The critical thickness is much greater than that predicted by the Matthews-Blakeslee theory, which could be due to the low growth temperatures used, as well as the presence of the growth interrupts which may inhibit dislocation multiplication. TED measurements show the presence of CuPt ordering in the GaAsBi layers, which could be linked to the surface reconstruction present during growth.

The diode samples can detect and emit light in the near-infrared, despite the presence of dislocations in the thicker layers. The band gap values obtained from both absorption and emission measurements are in good agreement with each other and are consistent with a Bi content of ~6%.

Evidence for localized states can be observed in both absorption and emission measurements. The absorption spectra show increased absorption below the band gap compared to GaAs, while in emission spectra localization is evidenced by the blue-shift of the EL peaks at low temperatures, the exponential tails observed in the low temperature EL spectra and the 'S-shaped' temperature dependence of the EL peaks.

The background doping in the GaAsBi layers is relatively high and needs to be improved in order to achieve a fully-depleted layer at zero bias, which is desirable for solar cells. The I-V characteristics of the samples exhibit ideality factors close to 2, which indicates recombination via the presence of trap states in the GaAsBi layers. The presence of such states could be related to the low growth temperature used. The saturation current density increases with the thicker layers and this is likely due to the increase in the number of dislocations with increasing thickness. The reverse dark currents are high and increase exponentially with reverse bias,

however since this is also the case for the GaAs control sample it is likely that the GaAsBi layers are not causing this behaviour. Though high, the dark currents are still better than those previously reported in the literature for similar samples.

7.2 Future work

Two main areas can be explored for future work: first, continuing work on the GaAsBi system, and second, looking at quaternary Bi-containing alloys such as GaAsBiN.

It would be interesting to grow p-i-n diode samples containing GaAsBi layers with different Bi contents. The effect of changing Bi content on the optical and electrical characteristics can then be ascertained. It would also be useful to have a GaAs control sample with an i-region grown at low temperatures in order to separate the effects of low-temperature growth and the addition of Bi.

Another potential application of GaAsBi for solar cells is its use as a middle junction of a triple junction cell, where it could replace the currently used InGaAs material system. Since a given band gap can be obtained with less strain using Bi compared to In, this may improve device performance. Only a small fraction of Bi (<1%) would be required for such an application, which would allow growth at a higher temperature than that used for the samples in this work.

For the application of a 1 eV band gap material that can be lattice matched to GaAs/Ge, quaternary Bi-containing alloys such as GaAsBiN will be neccessary. Since it will be difficult to use a nitrogen source on the MBE-STM machine due to space limitations, this will require the use of a different MBE reactor which possesses both Bi and N sources. This material can then be compared directly with InGaAsN.

Appendix A: X-ray diffraction simulation parameters for STB063

For STB063, simulations were performed using RADS Mercury software in order to determine the sample structure. The simulated structures for STB063 shown in figures 4.10 and 4.11 are given in the tables below. In both cases the GaAsBi epi-layer was assumed to be fully strained to the substrate.

Thickness (nm)	Material	[Bi] (%)
621	GaAs	-
108	GaAsBi	5.9
267	GaAs	-
Substrate	GaAs	-

Table A-1: Structure for STB063 assuming uniform GaAsBi layer (Figure 4.10).

Thickness (nm)	Material	[Bi] (%)
640	GaAs	-
50	GaAsBi	6
6	GaAsBi	3.9
50	GaAsBi	6.3
283	GaAs	-
Substrate	GaAs	-

Table A-2: Structure for STB063 including a spacer within the GaAsBi layer (Figure 4.11).

Appendix B: Calculation of lattice parameter as a function of Bi content and relaxation

The method outlined here is similar to that given in [1]. First the unstrained GaAsBi lattice constant was calculated using Vegard's law (Equation 3.2). As mentioned previously, the lattice constant of GaBi was taken to be 6.324 Å and Poisson's ratio, *s*, was assumed to be the same as that of GaAs (0.311). In the following equations *a* and *b* are taken to mean the lattice parameters in the *x*-*y* plane perpendicular to the growth direction, and *c* is the lattice parameter in the direction parallel to the growth direction *z*. Symmetrical relaxation is assumed, i.e. $a = b$. The equations for the strains ε_{ii} are derived from Hooke's law.

$$a_{epi}(R) = a_{GaAs} + R(a_{unstrained} - a_{GaAs}) \tag{B-1}$$

R is the relaxation which takes values between 0 and 1. When $R = 0$ the GaAsBi epi-layer is fully strained and a_{epi} is equal to the lattice constant of GaAs. When $R = 1$ the GaAsBi epi-layer is fully relaxed and a_{epi} is equal to the unstrained lattice parameter for the specified Bi content.

$$\varepsilon_{xx} = \varepsilon_{yy} = \frac{\left(a_{unstrained} - a_{epi}\right)}{a_{epi}} \tag{B-2}$$

$$\varepsilon_{zz} = -(2\varepsilon_{xx})\left(\frac{s}{1-s}\right) \tag{B-3}$$

$$c = a_{unstrained}(1 - \varepsilon_{zz}) \tag{B-4}$$

The calculated data were then plotted as an *xyz* contour plot where *x* = [Bi], *y* = % relaxation and *z* = *c*.

References

[1] D.K. Bowen and B.K. Tanner, *High Resolution X-Ray Diffractometry And Topography*: Taylor & Francis, 1998.